1-1-2013

Second Order And Fluctuating Hydrodynamic Theory Of Two-Particle Transverse Momentum Correlations In Nuclear Collisions

Rajendra Kumar Pokharel
Wayne State University,

SECOND ORDER AND FLUCTUATING HYDRODYNAMIC THEORY OF TWO-PARTICLE TRANSVERSE MOMENTUM CORRELATIONS IN NUCLEAR COLLISIONS

by

RAJENDRA K POKHAREL

DISSERTATION

Submitted to the Graduate School

of Wayne State University,

Detroit, Michigan

in partial fulfillment of the requirements

for the degree of

DOCTOR OF PHILOSOPHY

2013

MAJOR: PHYSICS

Approved by:

_____

Advisor Date

_____

_____

_____

DEDICATION

Dedicated to my parents for keeping up the traditional Brahmin culture of appreciating knowledge and inner search above anything else in the world, despite hardships they sometimes had to go through.

ACKNOWLEDGEMENTS

This work would not have been possible without a lot of help and support I received from many people. At this moment remember my teachers, relatives, friends from whom I received love, encouragement and support. The list is very long to fit here. I am grateful to all of them.

First of all, I would like express my gratitude to my advisor Prof. Sean Gavin for providing me this opportunity, support and academic guidance. Beside the academic support, I always remember him for his very friendly, helpful and personal approach.

I am grateful to my committee member Prof. Claude Pruneau for his help on computations and specifically on ROOT at the beginning and for sharing important information on experimental measurements of p_t correlations. I would like to thank Dr. Joern Putschke and Prof. David Cinabro for agreeing to be in my committee and for the help I received from them. I also like to thank Prof. Rene Bellwied, who was in my committee before he left for University of Huston. I would like to thank Prof. Ratna Naik for her constant encouragement and support. I would also want to thank Prof. Jogendra Wadehra for all the help I got from him.

I highly appreciate my friend Chris Zin for taking the painful task of proofreading and corrections and discussion. I would like to thank Dr. George Moschelli for providing some very important parts of the codes used for this work. I will always remember the the wonderful collaborative work we had here at Wayne State.

Finally, I would like to appreciate my wife Rama from my heart for being very supportive throughout. I appreciate my son Bhargav and daughter Bhumika for being being very patient and understanding.

The soul that sees beauty

may sometimes walk alone.

- Johann Wolfgang von Goethe

TABLE OF CONTENTS

LIST OF FIGURES

CHAPTER 1

INTRODUCTION

This dissertation is a detailed documentation of our studies on specific aspects of nuclear matter in extreme conditions of temperature, pressure and baryon density. Extreme conditions are believed to have prevailed a few microseconds after the Big Bang, the moment the universe was created. With the advancement in scientific knowledge and technology, it has become possible to create the extreme situation under laboratory conditions, in a very small scale of space and time. The experiments to create this kind of situation are the ultra-relativistic collisions of heavy nuclei. Such collisions are carried out at large laboratory facilities like Relativistic Heavy Ion Colliders (RHIC) at Brookhaven National Laboratory (BNL) and the Large Hadron Collider (LHC) at European Center for Nuclear Research (CERN).

RHIC started its operation at the beginning of the last decade and the LHC started its first run on Pb + Pb in 2010. At its optimum capacity, RHIC collides gold-gold nuclei at a center of mass energy of 200 GeV per nucleon pair ($\sqrt{s} = 200$ GeV). This is a tremendous amount of energy. To get some idea of the energy scale, we need to note that 200 GeV is equivalent to temperatures of $\sim 10^{12}$ K, about 100 million times the core temperature of the Sun. The LHC can collide lead-lead nuclei at $\sqrt{s} = 2.76$ TeV. The temperatures that can be reached in these collisions are greater than 300 MeV at the RHIC [8] and 420 MeV at the LHC [9]. Therefore, the matter created in such collisions is indeed under extreme conditions, albeit in an extremely small scale of space and time. This is the space and time scale of the order of a few tens of fermi (10^{-15} m).

The extreme temperatures and pressures are sufficient (i.e., the energy is larger than the QCD scale $\Lambda_{QCD} \sim 200$ MeV) to break the strong force that keeps the

quarks and gluons confined. At extreme energy density the quarks and gluons are deconfined and the matter transits to the phase of quark-gluon plasma (QGP). Lattice QCD calculations at zero baryon density have shown that the transition is a rapid crossover transition around the temperature $T \sim 170$ MeV [4, 18, 12]. In other words, the phase transition from hadrons to quark-gluon plasma is a second order rather than a first order according to the lattice QCD calculations.

The idea of the QCD phase transition and creation of weakly interacting QGP using extremely energetic collisions of heavy nuclei was envisioned [5] right after the discovery of asymptotic freedom [1, 2]. The kind of QGP envisioned before the advent of RHIC was a matter consisting of weakly coupled massless quarks and gluons. RHIC experimental results, however, showed that the heavy ion collision experiments actually produces a strongly interacting color plasma of quarks and gluons. It is not a gas consisting of weakly interacting quarks and gluons as was expected. This might however be the case at even higher temperatures well beyond the transition temperature. The existence of strongly interacting QGP is evidenced by a surprisingly large amount of elliptic flow, much larger (by an order of magnitude) than given by perturbative QCD. RHIC experiments also showed that the strongly interacting QGP behaves like a nearly perfect fluid - much less viscous than the superfluid liquid helium.

In the field of heavy ion physics, methods of relativistic hydrodynamics and relativistic kinetic theory have been extensively applied for the bulk treatment of the evolution of QGP. In relativistic hydrodynamics, the ratio of viscosity to entropy density serves as the kinematic viscosity. This ratio, η/s, is an important transport parameter to characterize the perfectness (or lack thereof) of QGP. Note that, while discussing viscosity of QGP in our work, we most often mean the shear viscosity, η. Bulk viscosity is often ignored in comparison to shear viscosity. This will be discussed in detail in Chapters 3 and 4. Hydrodynamic model calculations, both ideal and viscous, indicate that η for QGP is unlikely to exceed 0.3 (in the units where

$c = k_B = \hbar = 1$) [83]. AdS/CFT calculations have put a lower limit of $1/4\pi$ on its value [?]. This limit is known as the Kovtun-Son-Starinets (KSS) bound, and it is believed to be the lowest possible bound for η/s. Quantum kinetic theory calculations carried out as early as the mid 1980s [75] also put the lowest value close to this bound. In our theory, discussed in detail in subsequent chapters, this ratio plays an important role. The main ingredient of our theory is the causal diffusion of two-particle transverse momentum correlation in the quark-gluon plasma medium. The ratio η/s turns out to be a major factor of the diffusion and the relaxation coefficients of the causal diffusion equation.

The theory presented in this work is about hydrodynamic evolution of two-particle correlations of transverse momentum fluctuations. In general, two-particle correlations and related fluctuation studies and measurements are very useful as they reveal the space-time information on particle production and dynamics not observed by single particle distributions. Long range correlations, for example, indicate that the correlated particles should be produced at the earlier stage of particle production. Correlated pairs with large rapidity separation are like the twins separated at birth, while those with a short gap are like twins that have grown up together. Correlation measurements have played a very important role in most of the discoveries at RHIC and LHC. Measurements of jet tagged two-particle correlations provided us with the evidence of jet quenching and hence evidence of the existence of QGP. Another example is elliptic flow studies, which revealed the "nearly" perfect fluid behavior of the produced particles. These successes inspired further correlation measurements and studies like the "ridge", a long range correlation profile that will be briefly discussed in Chapter 2.

Experimental measurements of two-particle correlations have revealed a complex pattern of bumps and ridges in relative pseudo rapidity $\Delta\eta = \eta_1 - \eta_2$ and azimuthal angles $\Delta\phi = \phi_1 - \phi_2$ [38, 103, 44]. Recently, long range correlations have been observed

even in the case of d-Pb collisions at LHC [**?**]. We will give a general introduction of the correlation patterns and structures in Chapter 2. Especially interesting correlations are the long range correlations in relative rapidity, called the "ridge". PHOBOS (a RHIC collaboration) measurements show that the correlation extends to six units of relative pseudorapidity (Fig.2.14). The phenomenon of the ridge is probably among the most important experimental findings by RHIC experiments, after the discovery of high elliptic flow and jet quenching. We do not expect that the effects of short range phenomena like hydrodynamics, resonance decays and freezeout produce correlations with this big relative rapidity. Long range in relative rapidity means causally disconnected regions for hydrodynamic evolution. The long range correlations like the ridge must originate from the initial conditions and reveal early time dynamics, earlier than the time when the system of collided nuclei equilibrates thermally and hydrodynamic evolution sets in.

The main focus of our search for this work is how the second order viscous hydrodynamic evolution contributes to the two-particle transverse momentum, p_t, correlation structure. The first order case has already been studied by Gavin and Abdel-Aziz [71], the work that provided an alternate method for estimating η/s. The important ratio η/s has traditionally been estimated using elliptic flow data. In addition to our main theory of causal diffusion of p_t correlation, we also use the first order case in our studies. The purpose is to compare the results and to see if there are some distinct features that result from the second order theory alone.

We compute some experimentally measurable observables. These observables were introduced in the work of Gavin and Abdel-Aziz [71] and were measured by the STAR collaboration of RHIC [43]. We discuss these observables in detail in Chapter 6. The main goal of the STAR measurement was to estimate η/s, by the method proposed by Gavin and Abdel-Aziz. The range of values of η/s obtained by the measurements came out to be consistent with the values estimated from the flow

data. In addition, the STAR measurements of the observables have been invaluable for our study, especially to compare and test our second order theory. We will discuss the relevant experimental results in Chapter 6.

The core of our work here consists of two main parts. The first part is the development of the second order or causal deterministic diffusion equation for two-particle transverse momentum correlation using Israel-Stewart second order hydydrodymics. After reviewing basic hydrodynamics in some detail, we first obtain the causal diffusion equation for fluctuations in single particle momentum current in Chapter 3. In Chapter 5, we first discuss the general aspects of two-particle correlations and then move on to obtain the second order diffusion equation for two-particle p_t correlations. We find that the diffusion equation contains the stochastic noise. However the noise cancels out when we subtract the equilibrium part of the equation. This leads to our equation - the deterministic second order diffusion equation for p_t correlations over the background thermal correlations. The detail is in Chapter 5.

The the other part of our contribution consists of solving our equation and computing the observables. In addition to our second order equation, we also solve the first order diffusion equation, first obtained in Ref. [71]. We have already pointed out that the purpose of including the first order equation is to compare the two theory and to see if observables calculated using second order equations show some novel features. The correlations profiles in relative rapidity, $\Delta\eta$ have not been computed before for the first order. We will show that we do obtain novel features in the correlation in relative rapidity. Interestingly, STAR experimental results [43] also indicate such features. We present these exciting results and comparison with experimental data and also with the results obtained from the first order equations in Chapter 8.

Both first and second order theory requires information on viscosity and entropy density to obtain the strength of diffusion, i.e., the diffusion coefficient. The second order theory needs an additional coefficient - the relaxation time. Kinetic theory cal-

culations show that relaxation time is proportional to the diffusion coefficient. Therefore, both coefficients require η/s. This ratio is discussed in detail in Chapter 4. In that chapter we collect the available latest theoretical expressions for temperature dependent shear viscosity and discuss the equations of state that we use in our computations. We use two different equations of states: one is the equation of state based on the lattice QCD computations. The other equation of state we use is the standard equation of state based on the Bag Model. The equations stated gives entropy density which we combine with the temperature dependent shear viscosity to form a general temperature dependent η/s. The diffusion and relaxation coefficients are then obtained from the temperature dependent η/s.

We use only longitudinal expansion in our current work. The full 3+1 (space and time) dimensional treatment for two-particle correlations is our much more ambitious goal for the future work. Currently, there are theoretical and numeral challenges in that direction. Our future work in this regard is to address those challenges. We briefly discuss our immediate goal and the challenges in Chapter 9.

The generality of our results, as far as the observables are concerned, is not lost by the use of only longitudinal expansion. It turns out that the transverse expansion integrates out. We present this important point with a simple calculation in Chapter 9. This, however, does not reduce the importance of a full 3+1 dimensional theory. We need the full theory and computation because we want to understand the the whole correlation profiles in $\Delta\eta$ and $\Delta\phi$.

This dissertation has been organized in the following way. After this introductory chapter, we discuss the basics of heavy ion collisions and their most important features in Chapter 2. This is followed by a general detailed discussion of relativistic hydrodynamics which is geared toward building up the evolution equation for single particle transverse momentum current in Chapter 3. We then collect current information on viscosity and entropy density in Chapter 4. In that chapter, we discuss

the general temperature dependent η/s and the two different equations of state we use in our theory. In Chapter 5, we first discuss transverse momentum correlations in general and then obtain our major equation - the second order or causal deterministic diffusion equation for two-particle transverse momentum correlation. Next, we discuss the observables and the results of experimental measurements in Chapter 6. This is followed by the discussion of initial conditions, assumptions and parameters used in our computation in Chapter 7. We then present the results of numerical computations and compare with experimental results in Chapter 8. Finally, we make a brief but important statement on transverse expansion and present a sketch on our future work as well as make some concluding remarks in Chapter 9.

CHAPTER 2

BASICS OF HEAVY ION COLLISIONS

From ancient times, curiosity about nature, matter and the universe has guided the human quests toward two very diverged fronts of human knowledge. One is the quest about the basic units of matter. In other words, what are the basic building blocks of the matter? The other is just the opposite - how big is the universe? The great discoveries and paradigm shifts in the history of natural science are the consequences of human attempts to answer these apparently very diverged basic questions.

We know that our current knowledge of quarks, gluons, leptons and photons and their interactions are the results of our quest toward the basic units of matter. Our current knowledge in this respect is summarized in what is called the Standard Model. Our quest in the other direction has resulted in the current experimental knowledge, and the theoretical frameworks, about the vast universe we know so far. In fact the two diverged quests are not independent. We know more about the universe now because we know more about the basic building blocks of matter. The heavy ion collision experiments provide an excellent example of connecting these two seemingly diverged basic quests.

Currently the most accepted theory on the origin of the universe is the Big Bang theory. It is basically the extrapolation of the current expansion of the universe back in time using the theory of General Relativity. The Big Bang is the resulting (near) singularity containing extremely hot and dense matter. It is believed that the universe around one microsecond after the Big Bang was was made up of de-confined weakly bound quark and gluons. Such extreme matter is called quark-gluon plasma (QGP). The main purpose of heavy ion collision experiments is to create similar conditions in a small scale of space and time. This is the reason why relativistic heavy ion collision

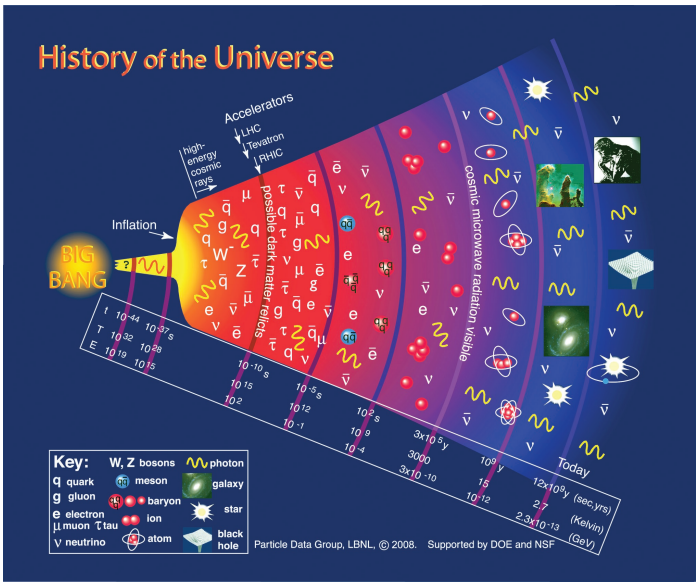

Figure 2.1: Time line of the universe according to the Big Bang theory. It is believed the form of matter was QGP at the time a few microseconds after the Big Bang. Image source: LBNL.

experiments are sometimes dubbed "Little Bangs". Thus, in a broad perspective, the goal of relativistic heavy ion collision experiments is to create and study quark-gluon plasma in order to look back into the universe's past, close to the time of the Big Bang.

Study of heavy ion collisions began to take real shape after the discovery of asymptotic freedom [1, 2]. Collins and Perry had suggested [3] that "superdense matter (found in neutron-star cores, exploding black holes, and the early big-bang universe) consists of quarks rather than hadrons. Figure 2.1 illustrates the likely scenario and the timeline of the universe, in accordance with the Big Bang theory.

The ultimate goal of the heavy ion colliders at RHIC and LHC is to create the quark-gluon plasma and study the properties of this extreme nuclear matter. The basic idea is that at very high temperature (compared to the QCD temperature scale, Λ_{QCD}), the confinements breaks and results in weakly coupled plasma of quarks and gluons. This is weakly coupled QGP (or wQGP). Theoretically, the regime of this matter is the regime of perturbative QCD. However, Hagedorn's work in 1970

demonstrated that hadronic matter has the phase boundary around 170 MeV, lower than Λ_{QCD} and out of the regime of perturbative QCD. Lattice QCD calculations [4] later also showed that phase transition occurs around that temperature. The plasma at this temperate is not wQGP, but rather a strongly interacting QGP, or sQGP. The unexpectedly high elliptic flow of the observed particles and the jet quenching shown by RHIC experiments indicated that the QGP produced in these collisions is strongly interacting QGP. At higher temperatures ($T \gg \Lambda_{QCD}$) the QGP may well be a weakly interacting QGP, but that has not been experimentally confirmed yet.

In this chapter we describe in detail the basics of heavy ion collisions. We start with a very brief discussion of basic idea of QCD in Section 2.1. Our purpose here is to be descriptive enough to put our subsequent discussions on quark-gluon colored plasma in context. In Section 2.2, we discuss some relevant aspects of heavy ion collisions. In following sections, we briefly discuss some basic features and elements of heavy ions physics and phenomena.

2.1 QCD and quark-gluon plasma

Our current knowledge of the most elementary building blocks of matter is described in a well established theoretical framework known as the Standard Model (SM) of particle physics. According to SM, the most fundamental building blocks are quarks, gluons, leptons, their antiparticles and the force carrier bosons. These particles are listed in the table of Fig. 2.2. The fundamental interactions among the particles are electromagnetic, weak interactions (called "electroweak" in combination) and the strong interactions (the "color force"). Electromagnetic interaction occurs between charged particles and the interaction is described by the theory of Quantum Electrodynamics (QED). Similarly, particles with color charge - the quarks and gluons, interact via the strong color force. Interactions these particles are governed by Quantum Chromodynamics (QCD).

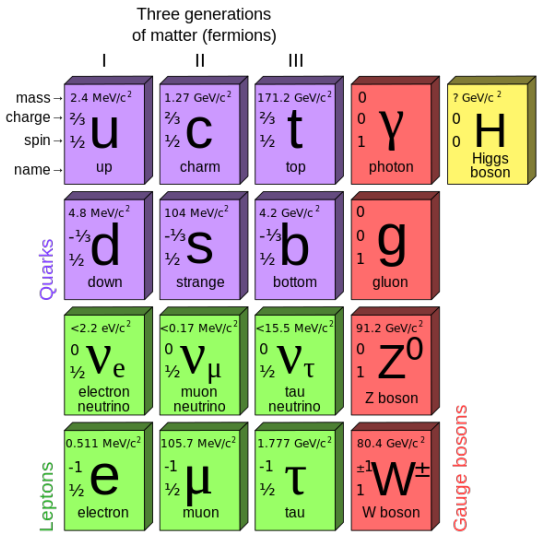

Figure 2.2: The "Periodic Table" of elementary particles (Standard Model). Current masses, charges and spins are indicated. The Higgs boson is responsible for assigning mass to an elementary particle according to the Standard Model. Image from Wikimedia.

According to the SM, protons, neutrons, pions and other hadrons are composite structures made up of quarks. Quarks come in 6 flavors: up, down, charm, strange, top and bottom. They are fermions and have fractional positive and negative charges. Up and down are the lightest quarks. They are often treated as massless in theoretical analysis. The bottom and the top are very heavy quarks. Fig. 2.2 shows the masses of quarks as well. We can see that mass of a strange quark is about 75% of the mass of a pion. Similarly a charm quark is slightly heavier than a proton.

An extra degree of freedom, besides the usual quantum numbers, is required to describe the interaction and dynamics in QCD. As an example, without this new quantum number, the exclusion principle does not allow for the existence of particles like Δ^{++}, which contains three strange quarks. This extra quantum number is called 'color'. It exists in three states: red, green and blue. Although 'colored' states can reside within a hadron, nature seems to dictate that free particles are always color singlet, i.e., color neutral. This is the reason one may never isolate a free quark. Analogous to photons of QED, and the $W^{\pm}$ and Z bosons of weak interactions, the

mediators of the strong interaction of QCD are gluons. There are eight gluons and an important distinction of QCD interactions is that gluons carry color charge and interact with themselves, along with the quarks.

Both QED and QCD are gauge theories. Each one has its own underlying symmetry and the exchange particle(s), called gauge bosons, for interactions. QED is a gauge theory with $U(1)$ symmetry having the photon as the gauge boson. In fact, QED is the abelian $U(1)$ component of the Standard Model symmetry $SU(3) \times SU(2) \times SU(1)$. Gauge bosons of this interaction, i.e., the mediators of QED interactions, are photons. The strength of interaction in any gauge theory is expressed by a coupling "constant", denoted by α. In general, α depends on the energy scale of the interaction. This results in a "running" coupling strengths. In QED at low energies (zero momentum transfer limit), $\alpha \approx 1/137$, and at about the scale of the Z boson ($m_Z \approx 91$ GeV), we have $\alpha(m_Z^2) \approx 1/129$. The coupling strengthen further at higher energy scales (or at lower length scales). At higher energy, $\alpha(E)$ grows further and diverges (the "Landau pole"). However, the perturbation techniques used for calculating the coupling looses its applicability at higher energy and the Landau pole is, most likely, not a reality. Thus, in QED, the coupling strength is very small ($\alpha(E) \ll 1$), and the method of perturbative calculations are applicable in QED. This also holds true for the weak interactions.

The underlying symmetry of QCD is $SU(3)$ and it is a non-abelian gauge theory. It has eight gauge bosons that interact with quarks and themselves. The interaction of gluons among themselves makes QCD more complicated than QED. A consequence is that the coupling strength in QCD has a feature that is very different from that of QED. First, the coupling strength is much higher and, second, it is much more sensitive to energy or momentum transfer. The dependence of coupling strength in the energy scale (or approximately the momentum transfer scale, Q) is given by the

so called Renormalization Group Equation (RGE):

$$Q^2 \frac{d\alpha_{QCD}}{dQ^2} \equiv \beta(\alpha) = b_0 + \mathcal{O}(\alpha^3_{QCD}) \tag{2.1}$$

In 1973, Gross, Wilczeck and Politzer first calculated [1, 2] this β function for QCD at the leading order (i.e., b_0 in Eqn. (2.1)), and found a negative value. A negative β means that the coupling decreases with increasing energy or momentum transfer. Ultimately, at very high energy coupling between quarks and gluons becomes very weak. This behavior is known as the asymptotic freedom. The value of b_0 is

$$b_0 = -\frac{33 - 2N_f}{12\pi} \tag{2.2}$$

Integrating Eqn 2.1 and using Eqn 2.2 one gets

$$\alpha_{QCD}(Q^2) = \frac{12\pi}{(33 - 2N_f) \ln\left(Q^2/\Lambda^2_{QCD}\right)} \tag{2.3}$$

Here, N_f is the number of flavors, and the constant of integration, Λ_{QCD}, is the QCD scale parameter ($\Lambda_{QCD} \approx 200$ MeV). Figure 2.3 shows the dependance of α_{QCD} with Q, along with the measured values from various experiments. We notice that for $Q^2 \gg \Lambda^2_{QCD}$, the coupling gets significantly smaller than unity and the interactions can be treated perturbatively.

We observe that at an energy scale of, say, a mass of 100 GeV, interactions between quarks and gluons are significantly weaker. Asymptotic freedom raises the hope of observing a plasma of free quarks and gluons. As is briefly mentioned in Chapter 1, Cabibbo, Parisi, Collins and Perry introduced the concept of super dense nuclear matter consisting of asymptotically free quarks and gluons [5, 3] in 1975. It was Shuryak who introduced the term 'qurak-gluon plasma' in 1978.

The quark-gluon plasma conceived originally is a weakly coupled quark-gluon

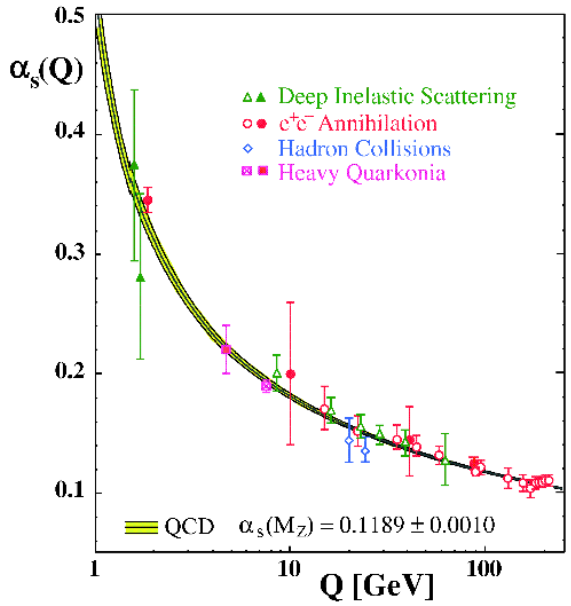

Figure 2.3: Running QCD coupling strength. Image is taken from [6].

plasma (wQGP) and it is predicted to exit at temperatures $T \gg \Lambda_{QCD}$. As is mentioned in Chapter 1, heavy ion collisions have found signatures of the production of quark-gluon plasma at much lower temperatures, $T \sim \Lambda_{QCD}$. This is not the regime of weakly coupled quarks and gluons. Instead, it turns out that hadrons like pions and protons melt to form a strongly coupled quark-gluon plasma (sQGP).

2.2 Heavy ion collisions

Relativistic heavy ion collisions have provided an opportunity to study extremely dense nuclear matter at extremely high temperature and pressure in laboratories. The extreme temperatures and pressures achieved at RHIC and LHC are produced by colliding heavy ions (like Au+Au at RHIC and Pb+Pb at LHC) head on at almost the speed of light. As mentioned in Chapter 1, the collision energy at these experiments for these ions can reach $\sqrt{s} = 200$ GeV and $\sqrt{s} = 2.76$ TeV, respectively.

The temperature in these collisions reaches more that 300 MeV at RHIC [8] and 420 MeV at LHC [9]. These temperatures are well above the QCD temperature scale

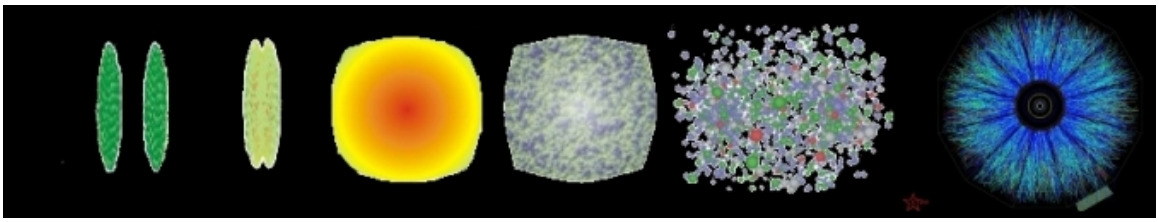

Figure 2.4: Stages of a heavy ion collision. Lorentz contracted nuclei (first image) pass through each other (second) depositing large amount of energy creating the QGP, which goes through hydrodynamic expansion (third). The system then hadronizes (fourth), free streams (second last) and the produced particles ultimately end up in the detector. The last image is what is seen in STAR detector. Image from S. Bass [7].

$\Lambda_{QCD} \approx 200$ MeV. Lattice QCD calculations have shown that, for vanishing baryon density, hadronic matter undergoes a phase transition to a medium of deconfined quarks and gluons at $T_C \approx 170$ MeV [4, 10, 11, 12]. The estimated energy at the transition is ~ 1 GeV. The energy density achieved in RHIC Au+Au collisions can reach about 5 GeV/fm^3.

One can see that the conditions for phase transition from hadrons to QGP are available in RHIC and LHC collisions of heavy ions. In fact, RHIC experiments carried out in the last decade have indicated the creation of such extreme nuclear matter [13, 14, 15, 16, 17]. As for the type of phase transition between the hadronic matter and the strongly coupled QGP, lattice QCD calculations indicate that the transition is a rapid crossover [4, 18, 12] around T_C.

Figure 2.4 describes the various stages of heavy ion collisions. At first, the two approaching Lorentz contracted nuclei collide and pass through each other depositing a large fraction of their energy in the overlap region. The region of extreme energy density is believed to be thermally equilibrated at around $\tau_0 \sim 1$ fm ($\tau =$ proper time). This is the quark-gluon plasma, indicated in the third image. The QGP undergoes hydrodynamic expansion and cools until the quarks and gluons hadronize. Hadrons lose energy and ultimately free stream (second to last image) into the detector. The last image in Fig. 2.4, illustrates the tracts of charged particles in the detector. A

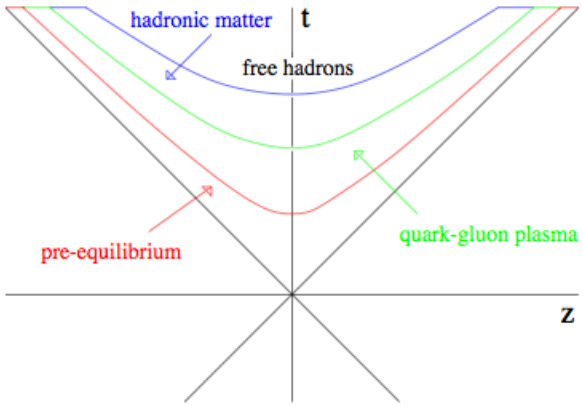

Figure 2.5: Evolution of a heavy ion collision. Various stages are shown. The hyperbolas represent the various constant proper times. Image from Ref. [19].

very large fraction of the detected particles are charged pions.

Figure 2.5 illustrates the evolution of the QGP created in a collision. Here, Z-axis is the collision axis. Hyperbolas are lines of constant proper time, $\tau = \sqrt{t^2 - z^2}$, for longitudinal expansion of the system. This figure shows the pre-equilibrium stage, the stage just after the collision and before the system thermalizes. Note that the world line of the incoming nuclei are like that of photons. In fact, the speed of the colliding nuclei is 99.995% the speed of light at RHIC energy. Nuclei at this speed and energy do not stop but pass through each other. In this process, they excite the QCD vacuum and create quarks, antiquarks and gluons. The system thermalizes locally and produces a quark-gluon plasma. In addition to the system of bulk matter, there are some partons or photons with much higher transverse momenta. Some of these particles manage to escape and ultimately end up being detected as "jets" in the detector after hadronization. We discuss jets shortly. After hydrodynamic expansion, the system cools and undergoes hadronization. During this time, the quarks and gluons recombine and result in formation of hadrons, most of which are pions. The hadrons further loose energy and ultimately end up in the detector.

A number of specialized detectors are used to detect particles produced in heavy ion collisions. Large experimental groups or collaborations analyze the tracks and

measures various properties, identify particles, and so on. STAR, PHENIX, PHOBOS and BRAHMS are the detectors and the respective collaborations at RHIC. At LHC, there are four major experimental groups associated with the four detectors: ATLAS, CMS, ALICE and LHCb. The details on these experimental groups and detectors are found on their web pages: [20] and [21].

2.3 Thermalization

When we talk about temperature of the medium created in heavy ion collisions, our tacit assumption is local thermal equilibrium. This is because the very concept of temperature requires that the system be in local thermal equilibrium. Local thermal equilibrium is also to apply the methods hydrodynamics and thermodynamics and treat the matter as a bulk. Small perturbation or fluctuations from local equilibrium form the basis of the study of transport properties like viscosity, thermal conductivity, relaxation time, etc. Therefore, in order to study such properties, we need the system under consideration be in thermal equilibrium. The question in our case is whether or not the medium created in heavy ion collisions thermalizes, at least approximately. One should note that a large number of particles are produced in heavy ion collisions at RHIC and the LHC. At RHIC the number is around 7000 and at the LHC it goes above 10,000. In terms of number of particles, the system can be treated as a bulk system.

Although we have no hard proof of thermalization yet, there is circumstantial evidence that helps us convince ourselves that the the medium produced at RHIC and LHC most likely equilibrates thermally, and it does so early in the evolution. How early? Again, no hard evidence. Based on several phenomenological arguments it is now more or less a consensus that the system thermalizes at $\tau_0 \leqslant 1$ fm.

A piece of evidence for thermalization is the observation of a large amount of flow of the observed particles. We will discuss flow in Section 2.4. Here, in the context of

thermalization, we note that experiments found a large amount of asymmetric flow called the elliptic flow. This kind of flow indicates multiple interactions among the constituents of the medium. A significant number of such interactions hint at the thermalization of the system early in its evolution.

An ddditional evidence, the evidence for chemical equilibrium, is provided by the excellent agreement of the observed particle multiplicity ratio with the ratio computed using the thermal equilibrium distribution of produced particles. Figure 2.6 compares the experimentally observed ratios of hadrons to the ratio computed using a thermal model, which assumes thermal equilibrium of the hadrons. Authors of Ref. [22], where this figure is taken from, state that: "The results demonstrate quantitatively the high degree of equilibration achieved for hadron production in central Au+Au collisions at RHIC energies." One, however, should also note that the particle ratios may not be a very reliable signal of an equilibrated medium as explained in [23]. This means that we also need to look for other piece of evidence. An excellent agreement of ideal hydrodynamic computations experimentally observed values for soft particles (disused in the next section), for example, may the an additional evidence. To paraphrase in slightly different way, the success of hydrodynamic models in explaining the collective behavior of soft particles observed at RHIC and the LHC has provided enough confidence to assume that the system is equilibrated early in the evolution.

2.4 Collective flow

One of the most striking findings from RHIC experiments is the observation of strong collective flow of produced particles. In particular, the observation of high elliptic flow was startling to the heavy heavy ion community at the beginning. Elliptic flow is an anisotropic flow observed in non-central collisions and is unique to heavy ion collisions. It is connected to initial geometry of collisions and, therefore, experimental

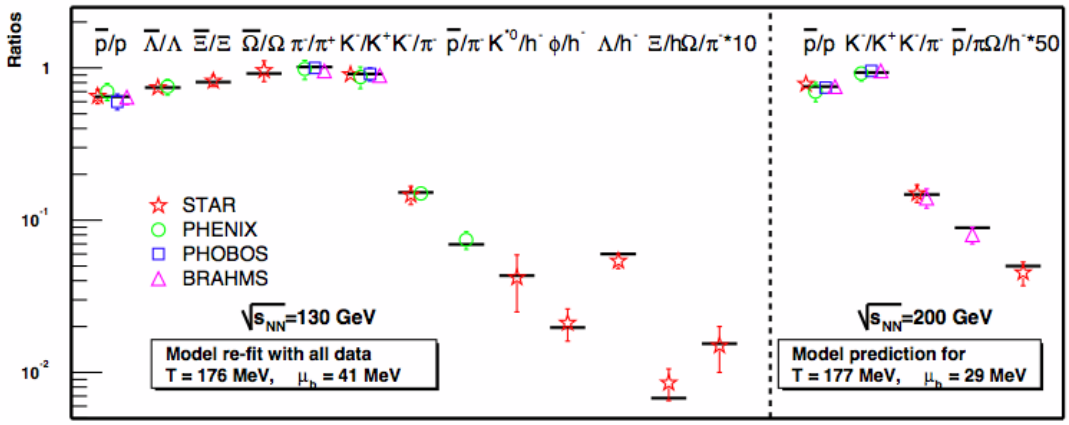

Figure 2.6: Comparison of experimentally observed particle multiplicity ratios computed using a thermal model. This figure is taken from Ref. [22].

data on this flow provides important information on the early stage of hydrodynamic expansion.

Anisotropy in flow largely results from the hydrodynamic response to the initial anisotropy in collision geometry. Figure 2.7 illustrates two different collision scenarios. The off-central collision, shown in the left panel, shows the creation of an almond shaped excited region. This spatial anisotropy in collision results in anisotropic pressure gradients. As the system undergoes hydrodynamic expansion and hadronizes, the final particles show anisotropic flow. It is clear that measured anisotropic flow gives us information on hydrodynamic response and, hence, on the properties of the matter created after the collision. The study of elliptic flow data from RHIC was one of the major sources leading to the discovery that the matter created in the collision (QGP) behaves like a perfect fluid [13, 14, 15, 16, 17].

Anisotropic flow studies use Fourier expansion of the azimuthal distribution of produced particles [24]. The azimuthal shape of the distribution varies with centrality and the components of the Fourier expansion provide the different harmonics of flow.

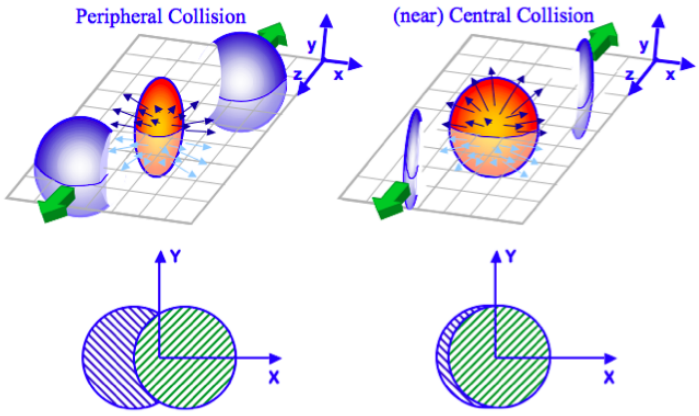

Figure 2.7: Collision geometry and the elliptic flow. Image on the left shows an off-center collision that creates an almond shaped excited medium. The pressure gradients result in a momentum gradient which leads to elliptic flow. The image on the right shows a central collision, which has more isotropic collision geometry and results in smaller elliptic flow. This image is created by Masashi Kaneta.

The Fourier expansion is written as

$$\frac{1}{N}\frac{dN}{d\phi} = 1 + 2v_1 \cos\left(\phi - \Psi_{RP}\right) + 2v_2 \cos\left[2\left(\phi - \Psi_{RP}\right)\right] + \cdots \tag{2.4}$$

The Fourier coefficients are given by

$$v_n = \langle \cos\left[n\left(\phi - \Psi_{RP}\right)\right] \rangle \tag{2.5}$$

Here Ψ_{RP} is the reaction plane angle. The average is taken over events. The reaction plane is spanned by the collision axis (z-axis in the figure) and the impact parameter. The components v_1 and v_2 are directed flow and elliptic flow, respectivey. Higher order flows have also been measured. The values of v_2 are significantly high. RHIC data for v_2 at $\sqrt{s} = 200$ GeV Au+Au collisions shows elliptic flow as high as $\sim 15\%$. This means that there are about 30% more particles in the direction of the reaction plane than out of plane. Figure 2.8 shows hydrodynamic model [25] calculations of v_2 with different values of η/s against the PHOBOS [26] and STAR [27]

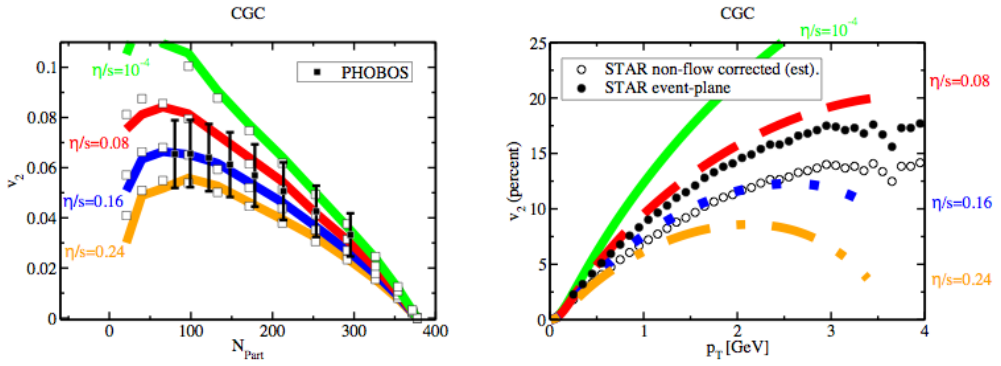

Figure 2.8: Hydrodynamic model calculations of v_2 from Ref. [25] compared with RHIC data. Left image shows comparison with PHOBOS data vs centrality. Image on the right shows comparison with STAR data. Figure is taken from Ref. [25]

data. We notice that, according to this model, values of η/s between the KSS bound ($1/4\pi = 0.08$) and twice this bound are consistent with the data.

One final note in our brief discussion of elliptic flow: RHIC data on v_2 demonstrates an explicit nature of quark constituency of the medium created in the heavy ion collision. The left panels of Fig. 2.9 shows v_2 for mesons (two quarks) and baryons (three quarks) plotted against p_T and KE_T. We see that v_2 of mesons and baryons data diverge. When the data are scaled with number of constituent quarks, all data (especially in the plot against KE_T/n_q) merge together is a single line. This demonstrates that patrons are the relevant degrees of freedom during the time elliptic flow is generated.

2.5 Jets

We will discuss jets very briefly here, enough to provide a little context for jet quenching, which is one of the most important discoveries of RHIC experiments. Jet quenching has provided an important piece of evidence for the creation of partonic matter, the quark-gluon plasma.

Jets are a group of several high p_t hadrons all moving approximately in the same direction. They originate from the hard scattering of incoming partons in hadron-

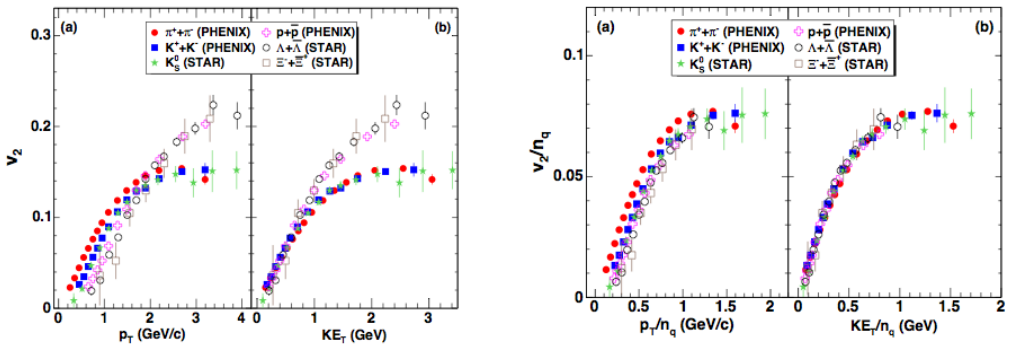

Figure 2.9: Quark scaling of elliptic flow for $\sqrt{s}$ =200 GeV Au+Au collisions. When scaled with number of constituent quarks, the baryon and meson data lies on the same curve. Figure is taken from Ref. [28]

hadron or nucleus-nucleus collisions. In the case of hadron-hadron collisions, high energy partons scatter off each other with large transverse momenta. These high p_t, colored partons radiate gluons which, in turn, split into quarks. These quarks ultimately become hadrons and form jets. When triggered correlations with associated hadrons are measured, large correlations are found on the near side (the side of the chosen trigger) as well as on the opposite side. This is the case of back to back jets. Back to back jets can be understood from momentum conservation. Momentum carried by a jet should be balanced by a jet in the opposite direction. This is actually what is observed in proton-proton collisions.

The so called quenching jets or more accurately the away side jet was observed from RHIC experiments [29]. Figure 2.10 shows a STAR analysis [29] that compares the triggered correlations in azimuthal angle for proton-proton, d+Au and Au+Au collisions. We see back to back correlations in the case of p+p collisions. We also see some away side correlations, though less than in the pp case, in 0-20% d+Au collisions. However in the case of central Au+Au collisions, the away side jet is conspicuously missing. On the other hand, the number of direct photons, which do not interact with the partonic medium, do not show this suppression [30]. This suppression of the away side jet is the well known jet quenching in heavy ion collisions and is one of the major

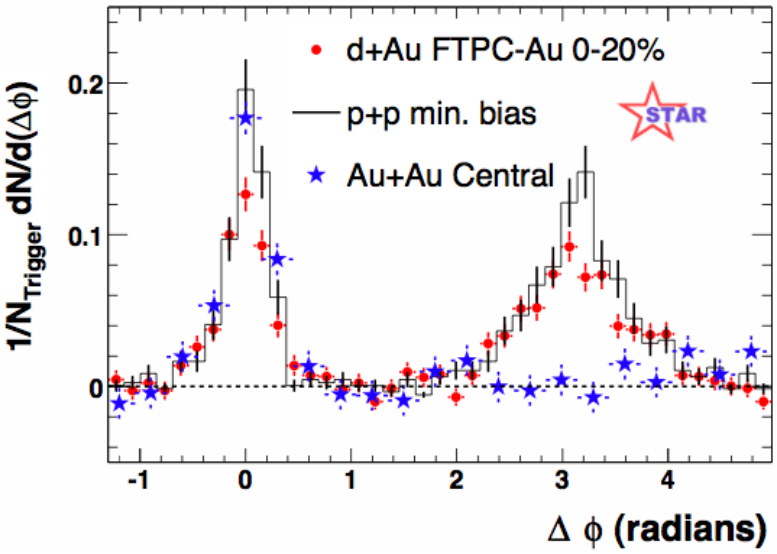

Figure 2.10: Measurements of azimuthal correlations in pp, d+Au and central Au+Au collisions. In central Au+Au collisions, the away side jet is missing, while jets on both sides show their full presence in pp collision. Figure is taken from Ref. [13]

discoveries at RHIC. Jet quenching results serve as a 3 dimensional tomography for the study of the medium created after the collision.

It is interesting to note that jet suppression had been predicted long before. Back in 1982, Bjorken [31] had said, "high energy quarks and gluons propagating through a quark gluon plasma suffer differential energy loss via elastic scattering from quanta in the plasma. An interesting signature may be events in which the hard collision occurs near the edge of the overlap region, with one jet escaping without absorption and the other fully absorbed." Later, Wang and Gyulassy [32] supplemented this idea with an important additional mode of energy loss - the energy loss to the medium by gluon bremsstrahlung. As we highlight shortly, RHIC experiments confirmed the jet suppression and suppression of high p_t particles in the spectra.

A simple qualitative explanation of jet quenching is the following. The large momentum taken away by the patrons, which fragment into near side jets ($\phi = 0$),

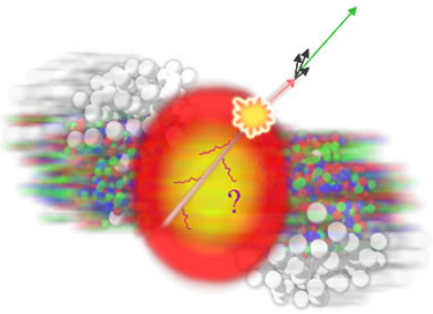

Figure 2.11: Jet quenching in heavy ion collision. A highly energetic parton near the surface of the medium escapes. The momentum conserving partner on the other side loses energy and cannot manage escape. Image: Lawrence Berkeley National Lab.

must be conserved. This results in a jet on the other side ($\phi = 180^o$). We see those back to back jets in pp collisions and also in d+Au collisions, as is already mentioned. In the case of Au+Au collisions, a dense partonic medium is created and the jets created near the surface of the medium escape and fragment into high p_t hadrons. The partons that go the other way encounter the dense partonic medium and lose energy before they fragment. Figure 2.11 illustrates this jet quenching scenario.

As a consequence of jet quenching, there is more suppression of high p_t particles in heavy ion collisions than one would expect if the collisions were a superposition of p+p collisions. Suppression, or lack thereof, may be quantified using the nuclear modification factor, R_{AB} for A+B collisions. It is defined as

$$R_{AB}(p_t) = \frac{dN_{AB}/d\eta d^2p_t}{T_{AB}d\sigma_{nn}/d\eta d^2p_t} \tag{2.6}$$

The nuclear thickness function (overlap integral), is $T_{AB} = \langle N_{binary}\rangle/\sigma_{pp,inelastic}$, is calculated using the Glauber model, and σ_{nn} is the nucleon-nucleon scattering cross section. If a nuclear collision is just a superposition of nucleon-nucleon collisions, we would expect a unit ratio. It deviates from unity if there is a modification. Figure 2.12 shows the results from STAR [33], PHENIX [34, 35], and ALICE [36].

The nuclear modification factor measures nuclear effects, i.e., effects of the nucleus

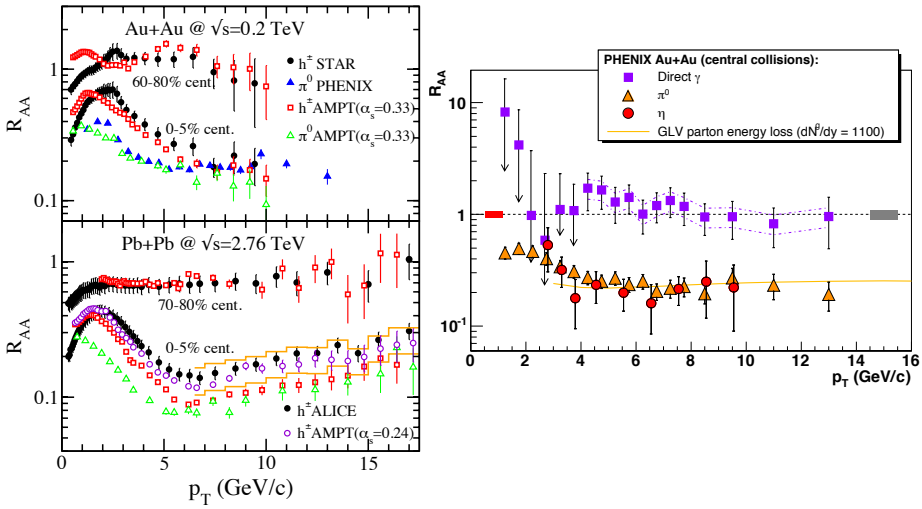

Figure 2.12: Nuclear modification factor in central and peripheral Au+Au collisions at RHIC (STAR, PHENIX) and Pb+Pb collisions at LHC (ALICE). Peripheral collisions have little nuclear effects (roughly like in pp collisions). The image on the right also shows PHENIX measurements of direct photons in Au+Au $\sqrt{s} = 200$ GeV collisions. Direct photons escape the medium without modification and show no suppression. The Image on the left is taken from Ref. [37], and that on the right is taken from Ref. [35].

in bulk. In the absence of nuclear effects the factor is expected to be unity, as shown by the direct photon data. The reason for the suppression is clearly the effect of the dense partonic medium created in collisions. In other words, it is a strong indication for the formation of quark-gluon plasma.

2.6 Correlations and the Ridge

Measurements of jet quenching and suppression of high p_t particles are examples of two-particle correlation measurements. As has been highlighted in Chapter 1, a correlation study of p_t fluctuations is the major goal of our investigation. We discuss the two-particle p_t correlations in detail in Chapter 5. Here, we briefly discuss the general features of the correlations used and measured in the field with specific focus on the short and long range correlations as well as the baseline of correlations called the "ridge". The baseline, also called the "offset", is one of the observables we are

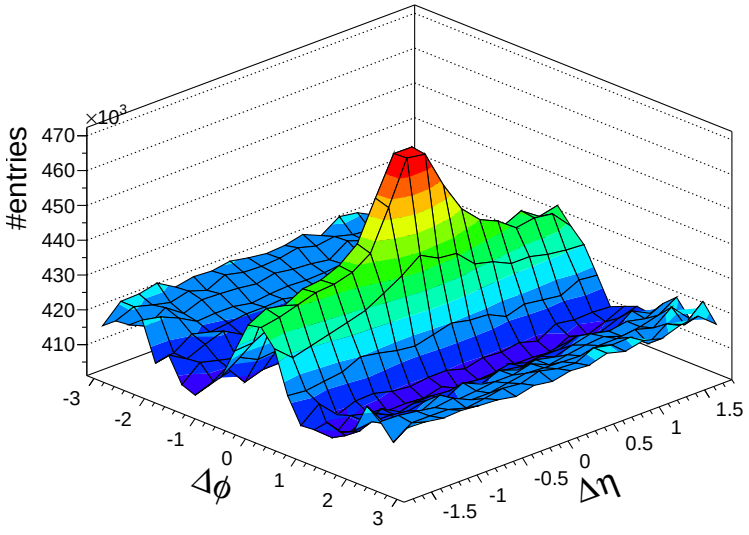

Figure 2.13: Triggered dihadron correlation measurements by STAR [38] for central Au+Au collisions at $\sqrt{s} = 200$ GeV. Source of this color image: Ref. [39].

interested in. We will discuss the offset in the chapter on observables (Chapter 6).

Besides jet quenching, a number of correlation measurements have been made in RHIC and LHC experiments. These measurements show complex valleys and ridges in relative azimuthal angle and pseudorapidity. Figure 2.13 shows triggered correlation measurements by STAR [38]. These results show the short range near side ($\Delta\phi = 0$) jet peak at $\Delta\eta = 0$ and correlation in the longer range in $\Delta\eta$. The ridge is the residual baseline structure left after one subtracts the jet and flow component v_2 from the correlations. It is obvious from the figure that the ridge in relative rapidity has much longer range that the size of the jets.

An even more dramatic long ridge was demonstrated by PHOBOS measurement results, shown in Fig. 2.14. This result is also for central Au+Au collisions at $\sqrt{s} = 200$ GeV. The acceptance in $\Delta\eta$ of this measurements is from -4 to 2. This result demonstrates that the ridge can extend to 6 units in $\Delta\eta$. What is interesting is that range of this big extension in $\Delta\eta$ is beyond any effect due to jets, resonances or hydrodynamic flows. The origin of the ridge must be from very early collision dynam-

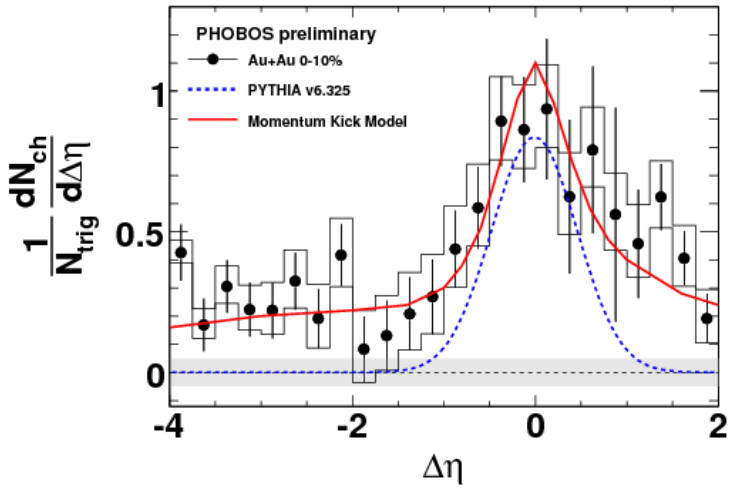

Figure 2.14: Long and short range correlation in $\Delta\eta$ for $\sqrt{s}$ = 200 GeV Au+Au collisions measured by PHOBOS with 0-10% centrality. Figure is from Ref. [44].

ics and from initial conditions. It should also be noted that the ridge phenomenon occurs in central collisions.

A recent explanation based on flux tubes and glasma initial conditions is offered in Ref. [40]. Other theoretical explanations of the ridge were discussed in Refs. [41] and [42].

In our model, we use hydrodynamic evolution of two-particle p_t-correlations and compute the offsets along with other observables. These observables have also been measured experimentally [43]. The observables and their experimentally measured values are discussed in detail in Chapter 6. The results from our computations of the offsets and comparison with experimental results are discussed in Chapter 8.

CHAPTER 3

HYDRODYNAMICS

Hydrodynamics or fluid dynamics is the study of dynamics of fluid in bulk. It consists of simple but general techniques and does not require a microscopic description of the constituent particles. The number of particles has to be large enough such that the fluid can be regarded as continuous rather than a system of discrete particles. It assumes local thermal equilibrium and is thus applicable as long as the inter-particle scattering is frequent enough to maintain local thermal equilibrium. In other words, the mean free path $\lambda = 1/n\sigma$ (n = density and σ = scattering cross section) has to be smaller than the length scale over which the thermal properties of the system varies. The system of fluid under study is divided into fluid cells such that each cell is small enough to regard properties like density, pressure, etc. constant within a cell but big enough to contain large number of particles so as to make it continuous. Hydrodynamics becomes indispensable for matter in bulk because it is simply hopeless to track and solve equations of motion for individual particles.

The idea of applying bulk matter treatment in elementary particle collisions goes back to the 1950s of the last century, long before QCD was discovered and long before there were heavy ion collision experiments. It started when Fermi [45] suggested the use of statistical methods to calculate the multiplicities and spectra of the mesons produced in high-energy collisions. The idea was extended by Landau [46] with his first use of relativistic hydrodynamics to describe the expansion of the medium after collisions. Later, Hagedorn [47, 48] made a major contributions on the possibility of limiting temperature in the hadronic phase and in thermal equilibrium. In 1983 Bjorken came up with a simple boost invariant hydrodynamic model [49] and gave an estimate of initial energy density. Interest in hydrodynamic models received a great

boost after the data from RHIC experiments [50, 51] turned out to be in good agreement with calculations based on relativistic hydrodynamics [52, 53]. This discovery is the main reason that led RHIC to announce the creation of "perfect liquid" [17]. Currently, hydrodynamics is a theoretical branch of its own in heavy ion physics. It is arguably the best theoretical framework to describe the space-time evolution of strongly interacting matter produced in ultra-relativistic collisions.

It should be noted that hydrodynamics best applies only to bulk matter consisting of the so called "soft" particles, the particles with transverse momenta, p_t, less than or around 2 GeV. However, more than 90% of the particles produces RHIC or LHC collisions fall into this category. Hydrodynamics is not suitable for the "hard" particles like highly energetic "jets", which have much larger transverse momenta. The assumption that there has to be local thermal equilibrium is fairly strong especially when one considers such high energy collisions in extremely small (a few fm) space and time scales. However, the particle spectra and the success of hydrodynamic calculations indicate that the system equilibrates very early ($\sim 1fm$).

3.1 Ideal hydrodynamics

We start from the simplest case: one-component non-relativistic ideal fluid dynamics. The degrees of freedom are the flow velocity $\mathbf{v}(t, \mathbf{x})$, the pressure $p(t, \mathbf{x})$ and the mass density $\rho(t, \mathbf{x})$. They are related [54] by the "continuity equation":

$$\frac{\partial \rho}{\partial t} + \nabla.(\rho \mathbf{v}) = 0 \tag{3.1}$$

and the "Euler equations":

$$\frac{\partial \mathbf{v}}{\partial t} + (\mathbf{v} \cdot \nabla)\mathbf{v} = -\frac{1}{\rho}\nabla p \tag{3.2}$$

In order to close the system of equations, an equation of state $p = p(\rho)$ must be included.

In the relativistic case, first of all we need to realize that mass density is not properly defined. One uses the total energy density $\varepsilon(x)$ replaces the mass density of non relativistic case. Also, the four-velocity $u^\mu \equiv dx^\mu/d\tau$ should replace the regular three-velocity of the fluid. The four velocity u^μ, or "flow", remains ambiguous especially in the context of dissipative flow. It leaves open the question: flow of what? The precise meaning will be made clear in the next section. Here $x = (t, \mathbf{x})$ and τ is the proper time given by $d\tau^2 = dt^2 - d\mathbf{x}^2$. The basic equations are conservation of current and energy-momentum:

$$\partial_\mu N_i^\mu = 0 \tag{3.3}$$

and

$$\partial_\mu T^{\mu\nu} = 0, \tag{3.4}$$

Using suitable expressions for N_i^μ and $T^{\mu\nu}$ in these conservation equations, one obtains [54, 55, 56, 57, 58, 59, 60, 61] the equations of relativistic hydrodynamics. The label i in (3.3) refers to the species of the particles constituting the conserved current, e.g., the baryon species.

For an ideal fluid (labeled by the subscript (0) below), currents and the energy-momentum tensor are given by

$$N_{i(0)}^\mu = nu^\mu \tag{3.5}$$

$$T_{(0)}^{\mu\nu} = (\epsilon + p)u^\mu u^\nu - pg^{\mu\nu} = \epsilon u^\mu u^\nu - p\Delta^{\mu\nu} \tag{3.6}$$

Here $g^{\mu\nu}$ is the Minkowski metric tensor $diag(1, -1, -1 - 1)$, and $\Delta^{\mu\nu}$ is the projection tensor operator that projects a tensor into the direction orthogonal to u^μ. A tensor is projected into the directions of u^μ or normal to u^μ by multiplying it by u^μ

or $\Delta^{\mu\nu}$, respectively. The former is a time-like projection and the later is space-like. In the local rest frame $u^\mu = (1,0,0,0)$ and $\Delta^{\mu\nu} = (0,-1,-1,-1)$. Note that, as mentioned in Chapter 1, we use the *mostly minuses* convention for the Miskowski metric and the speed of light is $c = 1$ so that $u_\mu u^\mu = 1$.

Relativistic hydrodynamics in heavy ion collisions is used mainly to model the evolution of baryon free quark-gluon plasma after the system thermalizes. Thus in baryon free case, we conserved baryon current (3.3) is not defined and equations are solely developed from the conservation of energy-momentum (3.4).

In order to get the equations of relativistic hydrodynamics one uses the conservation of energy-momentum, $\partial_\mu T^{\mu\nu} = 0$, and projects respectively into u^μ and $\Delta^{\mu\nu}$. Projection along u^ν, i.e., $u^\nu \partial_\mu T^{\mu\nu} = 0$, gives the *energy equation*:

$$D\epsilon + (\epsilon + p)\partial_\mu u^\mu = 0 \tag{3.7}$$

And, projection orthogonal to u^ν, i.e., $\Delta^\lambda_\nu \partial_\mu T^{\mu\nu} = 0$, gives the *momentum equation*:

$$(\epsilon + p)Du^\lambda - \nabla^\lambda p = 0 \tag{3.8}$$

Here $D = u^\mu \partial_\mu$ and $\nabla^\lambda = \Delta^{\lambda\mu}\partial_\mu$. Equations (3.7) and (3.8) are equations of relativistic ideal fluid dynamics. In the non-relativistic $|\mathbf{v}| \ll 1$, $D \approx \partial/\partial t + \mathbf{v}\cdot\nabla$ and $\nabla^i \approx \partial^i$. Also, in this limit $\epsilon \approx \rho$. These relativistic equations reduce to equations (3.1) and (3.2) in the non-relativistic case, $|\mathbf{v}| \ll 1$.

3.2 Dissipative hydrodynamics

In order to include dissipation, like viscosity, heat conduction etc, dissipative terms should be added to the energy-momentum tensor of ideal hydrodynamics. In this work, only viscous dissipation is considered. The form of the dissipative part of the energy momentum tensor, and hence, the equations of dissipative hydrodynamics

depend on how the local flow velocity u^μ is defined. There are two standard choices: Eckart's and Landau's approaches.

Eckart's [62] approach, in the context of heavy ion collisions, is to assign flow velocity to the conserved baryon current. In other words, u^μ is the velocity of the baryon number flow:

$$u^\mu = \frac{N^\mu}{\sqrt{N^\nu N_\nu}} \tag{3.9}$$

Landau's approach [54] is to assign velocity to the flow of energy. Thus, in this approach, u^μ is the velocity of energy flow. Since energy flow is $u_\nu T^{\mu\nu}$ (projection of energy momentum tensor in the direction of flow), the definition is

$$u^\mu = \frac{u_\nu T^{\mu\nu}}{\sqrt{u_\alpha T^{\alpha\beta} u_\beta}} = \frac{1}{\varepsilon} u_\nu T^{\mu\nu} \tag{3.10}$$

Thus, $\varepsilon u^\mu = u_\nu T^{\mu\nu}$, i.e., in the absence of baryon density all momentum density is due to the flow of energy in the Landau frame. In the Eckart frame, it is due to actual momentum current of baryon number flow.

It is clear the Landau frame is better suited to the study of the evolution of quark-gluon plasma created in relativistic heavy ion collisions. We therefore choose this frame, the Landau definition of flow, in our work. Also, we only consider viscous dissipation and do not consider dissipation due to heat conduction.

Writing $\Pi^{\mu\nu}$ for the viscous dissipative term, the energy-momentum tensor is:

$$T^{\mu\nu} = T^{\mu\nu}_{(0)} + \Pi^{\mu\nu} = \epsilon u^\mu u^\nu - p\Delta^{\mu\nu} + \Pi^{\mu\nu} \tag{3.11}$$

This does not mean anything unless $\Pi^{\mu\nu}$ is specified. A standard way to get an expression for $\Pi^{\mu\nu}$ is to make use of the second law of thermodynamics, i.e., entropy of the system never decreases:

$$\partial_\mu s^\mu \geq 0 \tag{3.12}$$

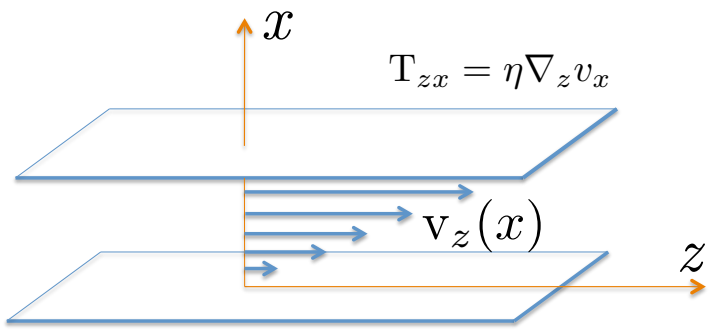

Figure 3.1: Shear viscosity results from shearing of fluid layers. In the process there is momentum transfer between the layers.

The equality sign here applies to the case of ideal fluid dynamics, in which entropy is conserved. The expression for s^μ in the dissipative case depends on the order of gradients (of flow, temperature) corrections we want to keep in the expansion about the ideal case $s^\mu = su^\mu$. In first order hydrodynamics, one keeps the first order correction and obtains the relativistic Navier-Stokes equations.

There are two kinds of viscous dissipation: bulk and shear viscous dissipation. Bulk viscosity arises in expansion and contraction of volume and shear viscosity is related to the momentum transfer when two layers of fluid move past each other (see Fig. 3.1). The contribution of bulk viscosity is negligible in comparison to that of shear viscosity. Bulk viscosity may, however, have some contribution around the critical temperature [63]. In this work, we ignore bulk viscosity - the only dissipation we consider is the shear viscous dissipation.

The dissipative term $\Pi^{\mu\nu}$ in Eqn.(3.11) is accordingly broken up into two terms:

$$\Pi^{\mu\nu} = \pi^{\mu\nu} + \Delta^{\mu\nu}\Pi, \tag{3.13}$$

where $\pi^{\mu\nu}$ is the shear viscous tensor and is traceless ($\pi^\mu_\mu = 0$), and Π is the bulk pressure.

Let us first get the equations of viscous hydrodynamics in the general form -

dissipative versions of (3.7) and (3.8). Taking the time-like component of energy-momentum conservation, $u^\nu \partial_\mu T^{\mu\nu} = 0$, we get

$$D\varepsilon + (\varepsilon + p)\partial_\mu u^\mu - \Pi^{\mu\nu}\nabla_{(\mu}u_{\nu)} = 0 \tag{3.14}$$

Similarly, picking up the components normal to the energy-momentum conservation, i.e., using $\Delta^\lambda_\nu \partial_\mu T^{\mu\nu} = 0$ one obtains

$$(\varepsilon + p)Du^\lambda - \nabla^\lambda p + \Delta^\lambda_\nu \partial_\mu \Pi^{\mu\nu} = 0 \tag{3.15}$$

Here $\Delta_{(\mu\nu)} = \frac{1}{2}(\nabla_\mu u_\nu + \nabla_\nu u_\mu)$, the symmetrized gradient of flow.

For the zero chemical potential case from thermodynamics we know that $\varepsilon + p = Ts$ and $Tds = d\varepsilon$. The later gives $TDs = D\varepsilon$ and when they are used in (3.14) we get

$$TDs + Ts\partial_\mu u^\mu - \Pi^{\mu\nu}\nabla_{(\mu}u_{\nu)} = 0 \tag{3.16}$$

3.3 First order dissipation and diffusion of transverse flow fluctuations

It should be noted that $\partial_\mu s^\mu = \partial_\mu(su^\mu) = Ds + s\partial_\mu u^\mu$, and Eqn.(3.16) now gives

$$\begin{aligned} \partial_\mu s^\mu &= \frac{1}{T}\Pi^{\mu\nu}\nabla_{(\mu}u_{\nu)} \\ &= \frac{1}{T}\Pi^{\mu\nu}(\nabla_{<\mu}u_{\nu>} + \frac{1}{3}\Delta_{\mu\nu}\nabla_\alpha u^\alpha), \end{aligned} \tag{3.17}$$

Here, $\nabla_{<\mu}u_{\nu>} = 2\nabla_{(\mu}u_{\nu)} - \frac{2}{3}\Delta_{\mu\nu}\nabla_\alpha u^\alpha$. From Eqn (3.13) and Eqn (3.17), we see that in order to make entropy production positive definite, i.e., to ensure Eqn (3.12) holds one must have

$$\pi_{\mu\nu} = \eta\nabla_{<\mu}u_{\nu>} \tag{3.18}$$

$$\Pi = \zeta\nabla_\alpha u^\alpha, \tag{3.19}$$

where $\eta, \zeta \geq 0$ are the coefficients of shear and bulk viscosity respectively. These results are the expressions for the coefficients of shear and bulk viscosities for relativistic Navier-Stokes theory. With (3.18) and (3.19), the expression for $\Pi^{\mu\nu}$ (3.13) becomes

$$\Pi^{\mu\nu} = \eta(\nabla^\mu u^\nu + \nabla^\nu u^\mu) + (\zeta - \frac{2}{3}\eta)\Delta^{\mu\nu}\nabla_\alpha u^\alpha. \tag{3.20}$$

This is the expression for the dissipative term $\Pi^{\mu\nu}$ in the first order, or Navier-Stokes, theory. When this expressions are substituted in (3.14) and (3.15), one obtains relativistic Navier-Stoke equations.

Transverse modes of hydrodynamic equations are diffusion modes while longitudinal modes are sound modes. It is the transverse modes we are interested in since we are going to relate the fluctuations in the transverse flow, and hence fluctuations in transverse momenta, to experimentally measured transverse momentum correlations.

We now linearize equations of first order relativistic hydrodynamics and take a transverse component. Let us consider small fluctuations on flow and other properties over their equilibrium values:

$$\begin{aligned} \varepsilon &= \varepsilon_0 + \delta\varepsilon(t, z) \\ p &= p_0 + \delta p(t, z) \\ u^\mu &= (1, \vec{0}) + \delta u^\mu(t, z) \end{aligned} \tag{3.21}$$

For simplicity in the argument, we have taken the perturbation as function of time and the coordinate z (later, it will be taken as the beam axis of collisions and x and y then become the transverse coordinates). Taking a transverse component ($\lambda = y$) in (3.15) and linearizing it gives

$$(\varepsilon_0 + p_0)\partial_t \delta u^y + \partial_z \delta\Pi^{zy} = 0. \tag{3.22}$$

Note that $D = u^\mu \partial^\mu = d/d\tau$ in general. In the local rest frame ($u^i = 0$), $D = \partial_t$. From (3.20),

$$\Pi^{zy} = \eta(\nabla^y u^z + \nabla^z u^y) + (\zeta - \frac{2}{3}\eta)\Delta^{zy}\nabla_\alpha u^\alpha. \tag{3.23}$$

Linearizing (3.23) using (3.21), we get

$$\delta\Pi^{zy} = -\eta_0 \partial_z \delta u^y \tag{3.24}$$

Equations (3.22) and (3.24) together now give

$$\frac{\partial}{\partial t}\delta u^y = \nu \frac{\partial^2}{\partial z^2}\delta u^y \tag{3.25}$$

Here $\nu = \eta_0/(\varepsilon_0 + p_0)$. This is a diffusion equation. We see that perturbation in flow diffuses in the medium with time. We know $\varepsilon + p = Ts$ and now see that the equilibrium value of η/Ts constitute the diffusion coefficient. Larger viscosity with constant temperature and entropy density means larger diffusion of transverse flow fluctuations.

3.4 Second order dissipation and causal diffusion

We see that transverse flow fluctuations diffuse in time in the medium and the evolution of the fluctuations is governed by diffusion equation like (3.25). There is however a well documented (see, for example [64, 65] and references therein) serious shortcoming in this kind of regular or "first order" diffusion equation. This is especially true if we want to use it for medium created in ultra-relativistic heavy ion collisions, when the fluid cells may have fairly good fraction of speed of light. The regular diffusion equation allows signals to propagate instantly and therefore the solutions violate causality. The other stated problem is the the stability of solutions for relativistic fluid [66]. Nonconformity with special relativity may not be a concern

for the fluid dynamics of most fluids. But the case of fluid consisting of relativistic quark and gluons is obviously a different matter.

Cattaneo devised a technique [67] to get around the problem by modifying Fourier's law of heat (which leads to the heat equation , one of the most common examples of diffusion equation). He added a time derivative of heat flux with relaxation time in Fourier law and it resulted in a hyperbolic equation, instead of the parabolic heat equation. Such an equation in mathematics literatures is known as the telegraph equation. Cattaneo's extra term was made up in order to preserve causality. It was later inferred from the second order Israel-Stewart theory [68] of fluid dynamics.

Second order hydrodynamics is built by taking corrections up to the second order gradients, in the way first order hydrodynamics is built using corrections up to the first order. The ntropy current, up to the second order gradients, is given by [56, 59]

$$s^\mu = su^\mu - \frac{\beta_0}{2T}u^\mu\Pi^2 - \frac{\beta_2}{2T}u^\mu\pi_{\alpha\beta}\pi^{\alpha\beta} \tag{3.26}$$

where, of course, small fluctuations from equilibrium of the medium are assumed. Now we take the divergence of (3.26). The first term on the right gives $\frac{1}{T}\Pi^{\mu\nu}\nabla_{(\mu}u_{\nu)}$, as before. The second term gives us $\Pi^2 D\left(\frac{\beta_0}{2T}\right) + \frac{\beta_0}{2T}D\Pi^2 + \frac{\beta_0}{2T}\Pi^2\partial_\mu u^\nu$. The last term produces $D\left(\frac{\beta_2}{2T}\right)\pi_{\alpha\beta}\pi^{\alpha\beta} + \frac{\beta_2}{T}\pi^{\alpha\beta}D\pi_{\alpha\beta} + \frac{\beta_2}{2T}\pi_{\alpha\beta}\pi^{\alpha\beta}\partial_\mu u^\mu$. Finally, manipulating the first term a little bit as done previously and putting together all the terms we obtain [56, 59] the expression for entropy production:

$$\begin{aligned}\partial_\mu s^\mu &= \frac{\pi^{\alpha\beta}}{2T}\left[\nabla_{<\alpha}u_{\beta>} - \pi_{\alpha\beta}TD\left(\frac{\beta_2}{T}\right) - 2\beta_2 D\pi_{\alpha\beta} - \beta_2\pi_{\alpha\beta}\partial_\mu u^\mu\right] \\ &\quad + \frac{\Pi}{2}\left[2\nabla_\alpha u^\alpha - \Pi TD\left(\frac{\beta_0}{T}\right) - \beta_0\Pi\partial_\mu u^\mu - 2\beta_0 D\Pi\right]\end{aligned} \tag{3.27}$$

Here the coefficients β_0 and β_2 are given by $\beta_0 = \frac{\tau_\Pi}{2\zeta}$ and $\beta_2 = \frac{\tau_\pi}{2\eta}$ [56]. The terms τ_π and τ_Π are relaxation times corresponding to shear and bulk viscous flow, respectively.

They characterize the times in which the second order (Israel-Stewart) hydrodynamics relaxes to the first order (Navier-Stokes) case.

As in the first order case, one needs to ensure that $\partial_\mu s^\mu$ is positive definite. This is always the case if

$$\pi_{\alpha\beta} = \eta \left[\nabla_{<\alpha} u_{\beta>} - \pi_{\alpha\beta} T D(\frac{\beta_2}{T}) - 2\beta_2 D\pi_{\alpha\beta} - \beta_2 \pi_{\alpha\beta} \partial_\mu u^\mu \right] \tag{3.28}$$

$$\Pi = \zeta \left[2\nabla_\alpha u^\alpha - \Pi T D\left(\frac{\beta_0}{T}\right) - \beta_0 \Pi \partial_\mu u^\mu - 2\beta_0 D\Pi \right] \tag{3.29}$$

As mentioned earlier, we ignore bulk viscosity and thus only consider shear viscous dissipation. Eqn (3.28) can be approximated [69, 70] to the Maxwell-Catteneo relation for $\pi_{\alpha\beta}$:

$$\tau_\pi D\pi_{\alpha\beta} + \pi_{\alpha\beta} = \eta \nabla_{<\alpha} u_{\beta>} \tag{3.30}$$

Thus, Israel-Stewart theory indeed gives us the Maxwell-Cattaneo relation. Now we linearize (3.28) or (3.30) using (3.21). The result is

$$\delta\pi^{\mu\nu} = \eta_0 \left(\partial^\mu \delta u^\nu + \partial^\nu \delta u^\mu - \frac{2}{3} g^{\mu\nu} \partial_\alpha u^\alpha \right) - \tau_\pi \partial_t \delta\pi^{\mu\nu} \tag{3.31}$$

This gives us

$$\tau_\pi \partial_t \delta\pi^{zy} + \delta\pi^{zy} = -\eta_0 \partial_z \delta u^y \tag{3.32}$$

Now from (3.22) and (3.32) one gets

$$\tau_\pi \frac{\partial^2 \delta u^y}{\partial t^2} + \frac{\partial}{\partial t} \delta u^y = \nu \frac{\partial^2}{\partial z^2} \delta u^y \tag{3.33}$$

This is the causal diffusion equation for transverse flow fluctuation. We see that the relaxation time τ_π moderates the speed and signals cannot propagate at superluminal speed. When τ_π vanishes we recover the regular diffusion equation. However, one

needs to be careful (especially from a numerical point of view) since in that limit the speed $\sqrt{\nu/\tau_\pi}$ becomes infinite.

Fluctuations in flow means fluctuations in momentum current. In the co-moving frame (where the average $u^y = 0$), the transverse momentum current of the fluid is given by $g_t \equiv \delta T_{0y} = T_{0y} - < T_{0y} > \approx (\varepsilon_0 + p_0)\delta u^y$ [71]. In terms of the transverse momentum current δT_{0y}, the second order diffusion equation (3.33) can be written as

$$\tau_\pi \frac{\partial^2 \delta T_{0y}}{\partial t^2} + \frac{\partial \delta T_{0y}}{\partial t} = \nu \nabla_z^2 \delta T_{0y} \tag{3.34}$$

Again, note that the diffusion coefficient ν is given by

$$\nu = \frac{\eta}{Ts} \tag{3.35}$$

We see that this coefficient contains an important ratio we often encounter in the physics of heavy ion collisions - the ratio of viscosity to entropy density, η/s.

The excess of momentum current over the average diffuses in the medium according to (3.34). In the limit $\tau_\pi \to 0$, this causal diffusion equation becomes identical to the regular diffusion equation. It should also be noted that the causal diffusion equation consists of two parts: a wave equation and a diffusion equation. In absence of the first order time derivative it becomes a wave equation describing the characteristic wavefronts traveling with a speed of $\sqrt{\nu/\tau_\pi}$. The presence of both wave propagation and diffusion leads to an interesting consequence in one of our observables. This feature will be discussed in detail in Chapter 8.

In Chapter 5, we extend this idea of diffusion of transverse momentum fluctuations to the more general concept of two-particle correlations. This will make the equations comparatively more complicated. We will employ Bjorken boost invariance in order to simplify the case. Boost invariance is briefly discussed in Section 3.5.

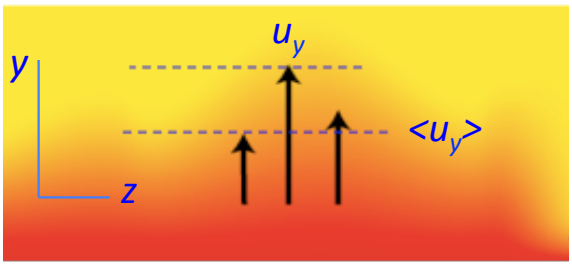

Figure 3.2: Flow fluctuation: excess from the ensemble average, $\delta u_y = u_y - < u_y >$ There is shear between layers since u_y has gradient along z. Shear viscosity involves momentum transfers and it goes on until the flow gets to its equilibrium level. Image: Sean Gavin (slightly modified here).

3.5 Bjorken model and boost invariance

Bjorken's hydrodynamic model [49] is a simple hydrodynamic model that employs a symmetry known as the boost invariance. Because of the simplification it offers in relativistic hydrodynamic calculations as applied to nuclear collisions, it has been applied in almost all hydrodynamic models heavy ion collisions. Bjorken model has been an an important booster for the application of relativistic hydrodynamics to nuclear collisions. The important step before this model was the introduction of the Landau model in the early history of hydrodynamic models [46]. Bjorken's boost invariance is based on the observation of the flatness of the rapidity distribution of charged particle multiplicity $dN_{ch}/d\eta$ in the mid rapidity region. This means the mid rapidity region is invariant under Lorentz boosts and the longitudinal (along the collision axis z) flow velocity can be put in the form v_z/t, like one dimensional Hubble expansion along the z-axis. All thermodynamic quantities used to describe the mid-rapidity region should then depend only on the longitudinal proper time $\tau = \sqrt{t^2 - z^2}$ and the transverse coordinates x and y. Figure 3.3 represents the idea of Bjorken's boost invariance expansion. With the simplicity brought about by the boost invariance, Bjorken was able to reduce the ideal relativistic hydrodynamic equations into a simple form that can be solved analytically. He was then able to

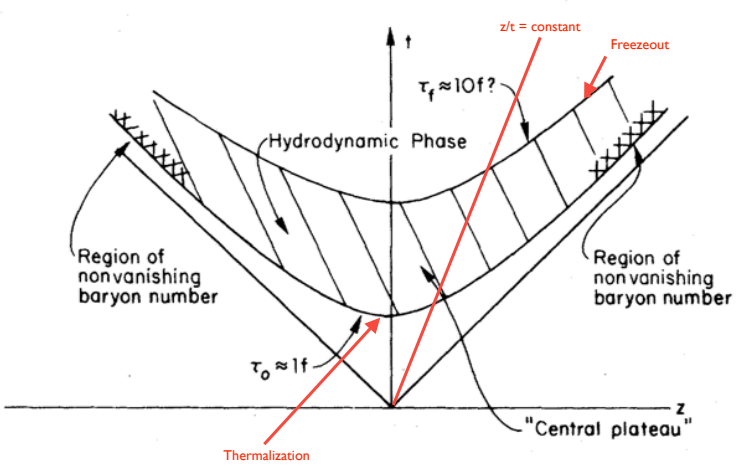

Figure 3.3: Bjorken boost invariant expansion. Hydrodynamic expansion starts after the thermalization time $\tau_0 \approx 1$ fm and lasts until the freeze out to hadrons. This figure is taken from the Bjorken's seminal paper [49] on boost invariant hydrodynamics. The text and lines in red are added labels.

estimate the initial energy density of the matter formed in heavy ion collisions.

Since we use Bjorken boost invariant expansion in our model, it is relevant to discuss its main concepts, especially the mathematical simplicity it brings about briefly. We first note that the flow velocity for longitudinal expansion with boost invariance can be written as

$$\bar{u}^\mu = \gamma(1, 0, 0, z/t) = (t/\tau, 0, 0, z/\tau) \tag{3.36}$$

Here, γ is the Lorentz factor $\gamma = 1/\sqrt{1-v^2}$ for longitudinal boost. The bar is used in order to reserve u^μ for flow in a different coordinate system we are going to use here (the Milne coordinates). We note that this form of flow already embodies the boost invariance. We can also write the flow in terms of proper time and rapidity variable. The rapidity variable is defined as

$$y = \tanh^{-1} v^z = \frac{1}{2}\ln\frac{1+v^z}{1-v^z} = \frac{1}{2}\ln\frac{E+p^z}{E-p^z} \tag{3.37}$$

where $E = p^0$ is the energy of the particle or fluid cell in question. For Bjorken boost invariance expansion $v^z = z/t$ and the flow rapidity reduces to spacetime rapidity

$$\eta = \frac{1}{2}\ln\frac{t+z}{t-z} \tag{3.38}$$

We then see that

$$t = \tau\ \cosh\eta \qquad z = \tau\ \sinh\eta \tag{3.39}$$

The four flow (3.36) can thus be written as

$$\bar{u}^\mu = (\ \cosh\eta, 0, 0,\ \sinh\eta) \tag{3.40}$$

This simplicity brought about by the Bjorken longitudinal boost invariance becomes even more revealing and its application in hydrodynamic equations becomes even simpler if we use the Milne coordinates $x^\mu = (\tau, x, y, \eta)$. In this coordinate system the four-flow (3.40) becomes

$$u^\mu = (1, 0, 0, 0). \tag{3.41}$$

This follows since $u^\tau = 1$ and $u^\eta = -\bar{u}^t\ \sinh\eta/\tau + \bar{u}^z\ \cosh\eta/\tau = 0$. This is interesting - there is no flow in the Milne coordinates. The coordinate system instead stretches by right amount to maintain the Bjorken boost invariance. As far as calculations are concerned, the flow (3.41) cannot get any simpler. However, this might be a little deceiving since the affine connections (the Christoffel symbols) of the Milne coordinates are not all zero. It turns out that only two are nonzero and they are $\Gamma^\eta_{\eta\tau} = 1/\tau$ and $\Gamma^\tau_{\eta\eta} = \tau$. Therefore, wherever necessary, we need to replace derivatives by covariant derivatives with these $\Gamma's$. For example,

$$\nabla_{,\mu}u^\mu \to \nabla_{;\mu}u^\mu = \partial_{;\mu}u^\mu = \partial_\mu u^\mu + \Gamma^\mu_{\mu\nu}u^\nu = \Gamma^\eta_{\eta\tau}u^\tau = 1/\tau \tag{3.42}$$

We know $D \equiv u^\mu \partial_\mu = d/d\tau$. Now with (3.42), Eqn. (3.14) for ideal hydrodynamics (without the last viscous term) becomes

$$\frac{d\varepsilon}{d\tau} + \frac{\varepsilon + p}{\tau} = 0 \tag{3.43}$$

With $p = \varepsilon/3$ for relativistic gas, one then gets

$$\varepsilon(\tau) = \varepsilon(\tau_0) \left(\frac{\tau_0}{\tau}\right)^{4/3}, \tag{3.44}$$

which is one of the famous Bjorken results.

As mentioned before, we are going to use the Bjorken boost invariant expansion in the hydrodynamics of two particle correlation in Chapter 5. In Chapter 4, we discuss the entropy production equations for first and second order hydrodynamics. Here, let us obtain evolution equation for entropy density for ideal hydrodynamics. We first note that in ideal hydrodynamics entropy conserves, i.e., $\partial_\mu s^\mu = \partial_\mu (s u^\mu) = 0$. Applying the same technique we used to get (3.43) and using $\varepsilon + p = Ts$, we obtain

$$\frac{ds}{d\tau} + \frac{s}{\tau} = 0, \tag{3.45}$$

which gives $s(\tau) = s(\tau_0)\tau/\tau_0$, another Bjorken result, which is basically just a statement of entropy conservation in a system that expands at the rate of $1/\tau$.

We use the techniques mentioned here to get the entropy production equations in Chapter 4. The results we obtain are the standard results already obtained in the last decade in the context of heavy ion physics. However, since we use the first and second order entropy production equations in our model, we are going to briefly demonstrate how they are obtained.

CHAPTER 4

VISCOSITY AND ENTROPY

Viscosity is a measure of diffusion of momentum parallel to the flow velocity and transverse to the gradient of the flow velocity [72]. Basically, it represents the ability to transport momentum. Shear viscosity arises as layers of fluid shear pass each other, as illustrated in Fig. 3.1. Bulk viscosity arises in compressible fluid when it expands or contracts. As we have already stated in Chapter 3, we consider only shear viscosity in our work. In the context of quark-gloun plasma, shear viscosity is the dominant mode of dissipation. It has been a standard practice to use the the ratio η/s rather than just η to describe viscous properties of fluids in relativistic hydrodynamics. This is similar to using kinematic viscosity $\eta/\rho = \eta/mn$ (ρ = density, m = mass, and n = number density of fluid particles) in Newtonian fluid dynamics. We are familiar with the convenience of kinematic viscosity over the dynamic viscosity. First the ratio appears in many useful hydrodynamic quantities, as in the Reynolds number. Also, it is the kinematic viscosity that determines the viscous term in the Navier-Stokes equations. Second, η varies widely in orders of magnitudes if one compares viscosities of various fluids while η/s is better in this respect. In the relativistic case, η/ρ or η/mn is not suitable since the number of particles are not conserved. Thus, η/s is most often taken as the kinematic viscosity for a relativistic fluid.

The main subject of our study is the diffusion of transverse momentum fluctuations and correlations. It was pointed out in Chapter 3 that the strength of diffusion, the diffusion coefficient ν in equation (3.34), is determined by η/s. In Chapter 5, we develop the diffusion equations for a two-particle transverse momentum correlation function. The structure of the diffusion coefficient however remains the same. We use a general temperature dependent η/s in our model and this leads to temperature

and, hence, time dependent diffusion and relaxation coefficients. The main focus of this chapter is to highlight the form of η/s as a function of temperature as used in our model.

4.1 Viscosity

RHIC experiments have shown that the matter created in collisions of heavy ions is strongly interacting quark-gluon plasma, not the weakly interacting QGP originally expected from perturbative QCD calculations. The good agreement of radial and elliptic flow data with ideal hydrodynamics has indicated that the matter has very low viscosity. On the other hand, lattice calculations have shown that the entropy density of this matter differs from Stephan-Boltzmann values only by $\sim$10% for temperatures higher than $\sim 2\ T_C$ (where $T_C \approx 170MeV$ is the critical or crossover temperature from the quark-gluon plasma to hadronic matter). In other words, according to lattice QCD calculations, the entropy density at higher temperatures ($T > 2T_c$) is not very different from that of the relativistic ideal gas. (We should note here that this picture has not been verified experimentally. High elliptic flow at LHC energy [73] cast some doubt on the idea of approximately weakly interacting quark-gluon plasma even at $T \sim 2T_C$). This means is that one needs to connect different pictures together: hadronic gas at low temperatures $T < T_C$, a weakly interacting ideal gas approach for T somewhat higher than T_C and strongly interacting partonic and hadronic matter in the in-between region, especially around T_C.

There has been a great deal of work ([74, 75, 76, 77, 78, 79, 80, 81], also covered in reviews like [82, 83]) on calculations of the viscosity of QGP on both sides of the critical temperature including the neighborhood of T_C. The most recent and detailed calculations on viscosity in the low temperature hadron phase were done in Ref. [84]. On the high temperature side, the most detailed and recent calculations for viscosity are found in Ref. [78, 79].

In Ref. [85], Hirano and Gyulassy have surveyed most of the works on calculations of shear viscosity. They argue that the low η/s of QGP does not arise from the sudden drop of viscosity at the transition, but rather is due to the sudden increase in entropy density. In their phenomenological model, they include the strongly coupled $\mathcal{N} = 4$ supersymmetric Yang-Mills (SYM) gauge theoretical calculations for η and η/s. The minimum for shear viscosity normalized to entropy density is taken to be the the conjectured lowest bound, the so called Kovtun-Son-Starinets (KSS) bound, $(\eta/s)_{KSS} = 1/4\pi$. It should be noted that kinetic theory calculations based on the uncertainty principle [75] also obtain values close to the KSS bound.

In our model, we use shear viscosity as a function of temperature in the form provided by Hirano-Gyulassy in Ref. [85]:

$$\eta(T) = \begin{cases} [1 + w \ln(T/T_C)]^2 T^3 & \text{for } T > T_C, \\ T_C^2 T & \text{for } T \leq T_C. \end{cases} \tag{4.1}$$

Here w is a parameter that depends on the running QCD coupling strength. Its suggested value in Ref. [85] is ~ 1. Fig. 4.1 shows how η depends on temperature. We note that the viscosity η increases monotonically at all temperatures below and above the critical temperature $T = T_C$.

4.2 Entropy

The expression of entropy as a function of temperature is the equation of state (EOS). Two different equations of state are used in our work. The first EOS, which we label as EOS I, is the lattice QCD EOS. This is basically the numerical values for for temperature and the corresponding entropy density obtained from lattice QCC calculations. We have used the values from Ref. [86], and details on the calculations are in Ref. [11]. In particular, we have used s95p-v1 from these references. As explained in this reference, the name s95 means that entropy density values reache

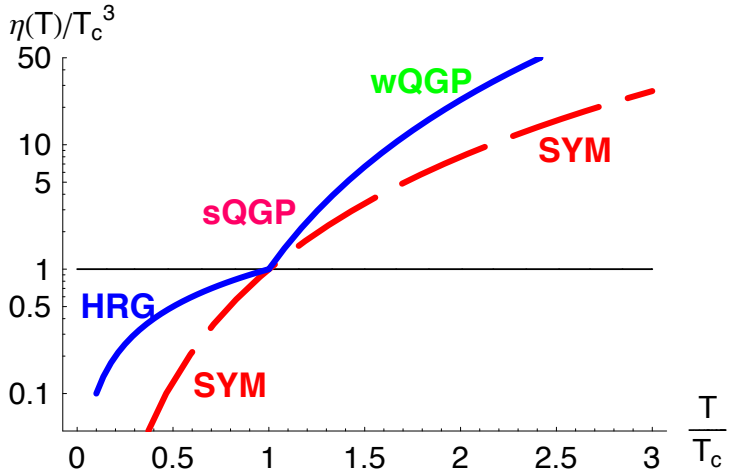

Figure 4.1: Shear viscosity as a function of temperature. Figure is taken from Ref. [85]. It shows $\eta(T)$ for strongly coupled QGP, weakly coupled QGP, hadron resonance gas and values calculated from infinitely coupled $\mathcal{N} = 4$ Super Symmetric Yang-Mills (SYM) theory.

at 95% of the ideal gas values at T = 800 MeV. There are slightly different values for entropy density depending on different parametrizations of the trace anomaly $(\varepsilon - 3p)/T^4$. Fig. 4.2 shows the different parametrizations and s95p-v1 is the solid line. Note that at both ends, the hadron resonance gas at low temperature limit and the partonic matter at the high temperature end, the system is close to a relativistic ideal gas, for which the trace anomaly vanishes ($\varepsilon = 3p$).

The lattice results are listed, as indicated in the figure 4.2, in Ref. [86] covers a big range of temperatures. As will be discussed in Chapter 8, we use constant temperature freeze out in our work and we choose the constant temperature to be 150 MeV. The initial temperature in then a function of centrality of the collision. and is not fixed. Initial temperature is higher for more central collisions and the system evolves for longer time before freeze out occurs. Therefore, we do not use the whole range of temperature given in the lattice numbers cited here. We cut the list off at 150 MeV in accordance with the choice of freeze out temperature in our model.

We also use an equation of state that is based on the Bag Model and assumes a

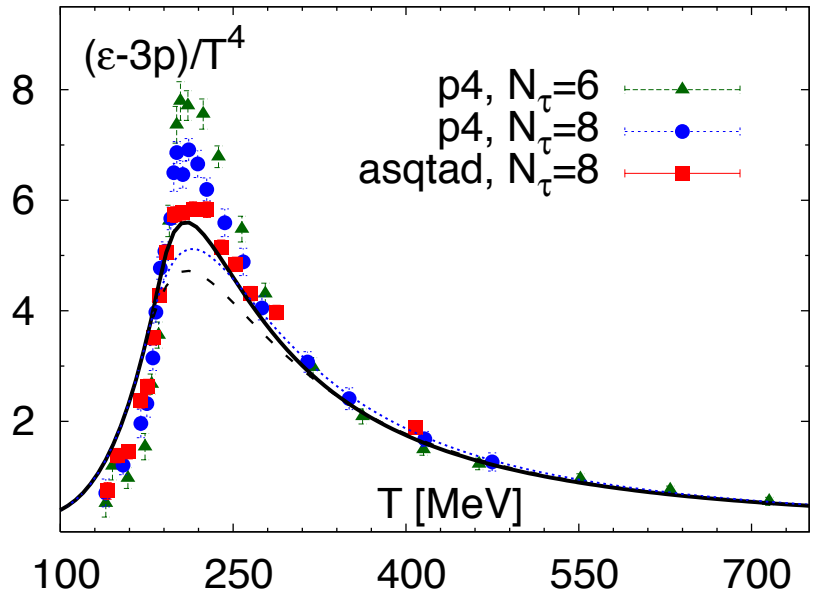

Figure 4.2: Parametrization of the trace anomaly calculated from lattice QCD. Figure is taken from Ref. [11], which has the details on the numbers and parametrization. In our calculation we have used s95-v1, which is represented by the solid line.

first order phase transition. This is the model discussed in the reference we have cited above for the expression of entropy density [85]. We label this EOS as EOS II. In this model, the phase transitions occurs at T_C with a jump in the entropy density. The abrupt rise in entropy density accounts for the low viscous behavior (i.e., low η/s) and is not because of a sudden drop in viscosity. Viscosity does not drop at T_C, as indicated in Fig 4.1. The entropy jump is given by the ratio s_Q/s_H, where s_Q and s_H are entropy densities of the quark-gluon phase and the hadronic phase, respectively. In this model the minimum η/s occurs at $T = T_C$ and equals the KSS bound. We add a linear interpolation of the mixed phase at $T = T_C$ to the Hirano-Gyulasssy model. The expression for $s(T)$ is:

$$s(T) = \begin{cases} 4\pi T^{1/c_s^2} & \text{for } T > T_C, \\ \frac{4\pi}{a}[f(a-1)+1]T_C^3 & \text{for } T = T_C, \\ (\frac{4\pi}{a})T^{1/c_H^2} & \text{for } T < T_C. \end{cases} \tag{4.2}$$

Here, $a = s_Q/s_H$. Clearly, a depends on the number of flavors in the model. Also, f is the fraction of quark-gluon plasma to hadronic matter in the mixed phase and varies from 0 for hadronic gas to 1 for QGP. The quantities c_s and c_H are speeds of sound in quark-gluon and hadronic phases respectively.

4.3 Entropy producion equations

The temperature dependent viscosity and entropy density discussed in the last section provides us a temperature dependent η/s. In order to apply this to the evolution of the system, we need to express both entropy and temperature of the system(hence, η/s) as functions of time. Using the Bjorken boost invariant longitudinal expansion, we apply the techniques mentioned in Section 3.5 and use the hydrodynamic equations from Chapter 3.

Eqn. (3.16), neglecting bulk viscosity, can be written as

$$TDs + Ts\partial_\mu u^\mu = \pi^\mu_\nu \nabla_\mu u^\nu \tag{4.3}$$

Using the methods from Section 3.5 we get

$$\frac{ds}{d\tau} + \frac{s}{\tau} = \frac{\pi}{T\tau}. \tag{4.4}$$

Here $\pi = \pi^\eta_\eta$. Note that we have used the Milne coordinates here, where π^μ_ν reduces to this simple form. In regular coordinates (t, x, y, z), it equals $\pi^0_0 - \pi^z_z$.

For the first order theory, i.e., the Navier-Stokes theory, the expression for π^η_η is obtained from (Eqn 3.18) using boost invariance. This gives $\pi \equiv \pi^\eta_\eta = \nabla_{<\eta} u^\nu_{>} = \eta(2/\tau - (2/3)\cdot 1/\tau) = 4\eta/3\tau$. Thus, for the first order theory, π is given by

$$\pi = \frac{4\eta}{3\tau} \tag{4.5}$$

Therefore, from Eqn. (4.4), the first order entropy production equation is

$$\frac{ds}{d\tau} + \frac{s}{\tau} = \frac{4\eta}{3T\tau^2}. \tag{4.6}$$

Similarly, using Eqn (3.28), one gets

$$\pi = \eta \left(\frac{4}{3\tau} - \pi T \frac{d}{d\tau} \frac{\beta_2}{T} - \frac{\tau_\pi}{\eta} \frac{d\pi}{d\tau} - \frac{\tau_\pi}{2\eta\tau} \pi \right) \tag{4.7}$$

Using $\beta_2 = \tau_\pi / 2\eta$, and rearranging terms, this last equation gives

$$\tau_\pi \frac{d\pi}{d\tau} + \left(1 + \frac{\tau_\pi}{2\tau} + \frac{1}{2} \eta T \frac{d}{d\tau} (\frac{\tau_\pi}{\eta T}) \right) \pi = \frac{4\eta}{3\tau} \tag{4.8}$$

Thus Eqn. (4.4) with π given by Eqn. (4.8) is the second order entropy production equation. Eqn. (4.8) was first obtained in [64] (also, see erratum [87]).

4.4 The ratio η/s

In previous sections, we discussed shear viscosity and entropy density as functions of temperature. The later comes from two different equations of state (EOS): EOS I and EOS II. The first is based on lattice QCD calculations while the second is based on the bag model. In the case of EOS II, we added the mixed phase, as described in Section 4.2. We parametrized the lattice results for s and T as $T(s^{1/3})$. Using the expressions and entropy productions equations we then obtain η/s as a function of proper time. The results are used to obtain diffusion coefficient ν and relaxation time τ_π as function of proper time. These time coefficients are then used in diffusion equations, which we discuss in subsequent chapters. Fig. 4.3 shows how η/s varies with temperature in our model. The dotted red line is for EOS II, and the blue solid line is for EOS I.

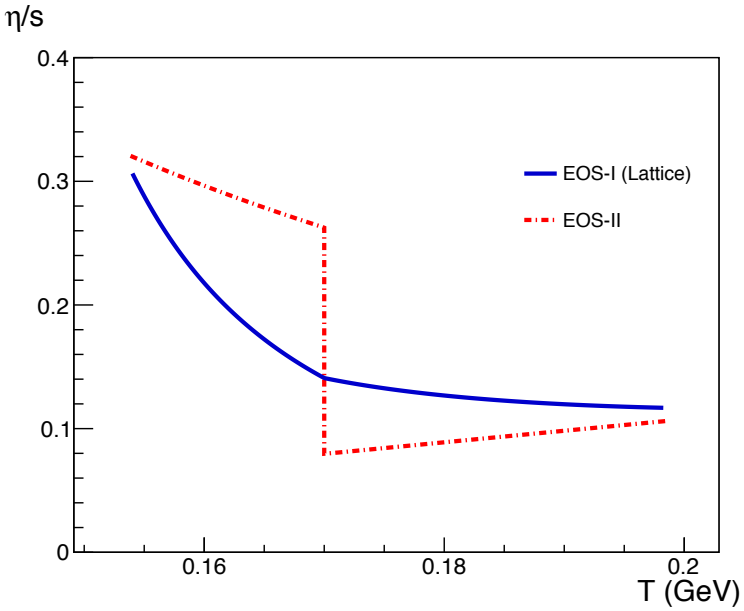

Figure 4.3: η/s vs temperature from EOS I and EOS II. Entropy density for EOS I is from lattice QCD calculations and viscosity is from [11]. For EOS II, η/s is from Ref. [85].

CHAPTER 5

CORRELATIONS AND FLUCTUATIONS

In the most basic terms, "correlation" is used to indicate how particles at two locations in space and time influence each other. Correlation functions are constructed in such a way that if there is no influence at all, the functions are zero on the average. Correlation measurements of detected particles have played very important roles in several discoveries at RHIC [13, 14, 15, 16] and LHC [73, 88, 89] and demonstrated strong flow, jet quenching effect, which indicate that the presence of quark-gluon medium. The "ridge" obtained from RHIC data is basically a long range correlation [90, 91]. Correlation measurements reveal space-time information on particle production. There are many likely sources for correlations. They include particle being produced from the same source, like same fluid cell, or resonance decays (e.g., pions coming out of the same ρ), energy momentum conservation, collective effects like anisotropic flows. Particles produced from the same source is a major factor for long range correlations. Long range correlations reveal that the particle should be produced at the early stage, right after the collision. Our study is focused on the hydrodynamic evolution of correlations. Hydrodynamics, however, is unlikely to contribute to long range correlations. Events that are highly separated in rapidity are too far (in rapidity space) to be causally connected to occur later in evolution. Long range correlations like that shown in Fig. 2.14 are casually disconnected for any hydrodynamic evolution.

Our study deals with correlations of fluctuations. We discussed transverse flow fluctuations and resulting transverse momentum fluctuation. We have already discussed diffusion of transverse momentum fluctuations in previous chapters. Fluctuations of especially conserved quantities are interesting and important as they, for

example, indicate the phase transition. A simple and common example of fluctuation is the critical opalescence of water. The generally discussed fluctuations in heavy ion physics are the fluctuations of multiplicity, charge and of traverse momentum.

In our work, we deal with fluctuations of transverse momentum. It is different from multiplicity fluctuations in that number of particles is not a conserved quantity but transverse momentum is. The focus of our work is on the correlations of transverse momentum fluctuations. In this chapter, we start by going over the diffusion of single particle transverse momentum fluctuations in Section 5.1, discuss the two-particle transverse momentum density fluctuations in Section 5.2. In Section 5.3, we develop the second order diffusion equation for two-particle correlation function including Langevin noise. We then demonstrate that we can get a deterministic diffusion equation for the correlation above the background thermal noise. The development of second order deterministic equation is our new work. Finally, we discuss the relaxation time in the last two sections. We have already seen that the relaxation time arises due to causality constraint - a consequence of second order hydrodynamics. We will very briefly mention an interesting effect of the second order time derivative term in the causal diffusion equation.

5.1 Transverse momentum fluctuations

The momentum density current of a single fluid particle is given by

$$T^{0i} = \gamma(\epsilon + p)u^i \tag{5.1}$$

As mentioned in Chapter 3, we use the Landau frame (or Landau definition of flow u^μ). In this frame $\pi^{0i} = \pi^{i0} = 0$. We also introduced fluctuation in momentum current there

$$\delta T^{0i} \approx (\epsilon + p)\delta u^i \tag{5.2}$$

Obviously, fluctuations in flow give rise to fluctuations in momentum current. We consider only transverse flow and, hence, only transverse momentum fluctuations. Fig. 3.2 illustrates the transverse flow fluctuations. We have already seen that transverse momentum fluctuations diffuse in fluid and that diffusion brings the system back to the local equilibrium. Fluctuations do not last long and ultimately become thermal background fluctuations - the fluctuations that exist even in equilibrium. Realistically, there is always background noise. The quantity δT^{0i} is the fluctuation on the top of the background average. The diffusion of δT^{0i} involves momentum transfer, which is related to shear viscosity. In fact, shear viscosity determines the strength of diffusion, as we have already seen in Chapter 3. Let us rewrite the first order version of Eqn. 3.34 (this follows from (3.25) in the same way)

$$\frac{\partial \delta T_{0y}}{\partial t} = \nu \nabla^2 \delta T_{0y}, \tag{5.3}$$

and Eqn. (3.34)

$$\tau_\pi \frac{\partial^2 \delta T_{0y}}{\partial t^2} + \frac{\partial \delta T_{0y}}{\partial t} = \nu \nabla^2 \delta T_{0y}. \tag{5.4}$$

Eqn. (5.3) clearly expresses that the momentum density fluctuations diffuse over the time - following a regular or first order diffusion equation. Eqn. (5.4) includes the second order corrections. Note that the diffusions coefficient contains shear viscosity: $\nu = \eta/Ts$. As we have already mentioned, we consider only shear viscosity.

5.2 Two-particle transverse momentum correlation function

Transverse momentum fluctuations can be used to construct a two-particle correlation function. This can then be used to obtain the expression for a relation on how such fluctuations diffuse over time. Let us label a pair of particles or fluid cells by 1 and 2. Note that we are dealing with transverse momentum and therefore pick up a transverse component for i, let us say $i = y$. A two-particle correlation function for

transverse momentum can then be defined as

$$r = \langle T_1^{0y} T_2^{0y} \rangle - \langle T_1^{0y} \rangle \langle T_2^{0y} \rangle \tag{5.5}$$

This is equal time correlations and the labels 1 and 2 actually represent the two locations of the fluid particles being correlated, i.e., $T_1^{0y} \equiv T^{0y}(\mathbf{x}_1)$ and $T_2^{0y} \equiv T^{0y}(\mathbf{x}_2)$. The angular brackets represent average over ensembles of events. Now we consider a small perturbation on T_1^{0y}:

$$\delta T_1^{0y} = T_1^{0y} - \langle T_1^{0y} \rangle \tag{5.6}$$

Obviously, we see that $\langle \delta T_1^{0y} \rangle = 0$. However, average of $\delta T_1^{0y} \delta T_2^{0y}$ does not vanish, as it would be expected in the case of a deterministic quantity.

We treat perturbations as stochastic term and employ the stochastic methods ([92, 93]) from here on. From (5.5) we get

$$r = \langle \delta T_1^{0y} \bar{T}_2^{0y} \rangle + \langle \bar{T}_1^{0y} \delta T_2^{0y} \rangle + \langle \delta T_1^{0y} \delta T_2^{0y} \rangle. \tag{5.7}$$

The bar over T_1^{0y} also represent the average over an ensemble of events and is used for notational simplicity. Following standard stochastic methods, we keen the last term although it appears as a second order in fluctuations. This term becomes a contributing factor because of the stochastic nature of perturbations (which also gives $\langle \delta T_1^{0y} \rangle = \langle \delta T_2^{0y} \rangle = 0$). In absence of noise it vanishes as δt^2. In the presence of noise, however, this term evolves only as $\sqrt{\delta t}$ and does not vanish as δt^2, as one might expect [92].

5.3 Diffusion of the correlation function

We proceed to obtain a diffusion equation for a two-particle correlation function, similar to Eqn (5.4). For that we differentiate (5.7) and evaluate $\left(\tau_\pi \frac{\partial^2}{\partial t^2} + \frac{\partial}{\partial t}\right) r$.

Differentiating and arranging the terms gives

$$\begin{aligned}\left(\tau_\pi\frac{\partial^2}{\partial t^2}+\frac{\partial}{\partial t}\right)r &= \langle\left(\tau_\pi\frac{\partial^2}{\partial t^2}+\frac{\partial}{\partial t}\right)\delta T_1^{0y}\bar{T}_2^{0y}\rangle \\ &+ \langle\bar{T}_1^{0y}\left(\tau_\pi\frac{\partial^2}{\partial t^2}+\frac{\partial}{\partial t}\right)\delta T_2^{0y}\rangle \\ &+ \left(\tau_\pi\frac{\partial^2}{\partial t^2}+\frac{\partial}{\partial t}\right)\langle\delta T_1^{0y}\delta T_2^{0y}\rangle \end{aligned} \tag{5.8}$$

The last term represents noise and is non-zero only when $\mathbf{x}_1 = \mathbf{x}_2$. We will call this term Γ and note that $\Gamma \propto \delta(\mathbf{x}_1 - \mathbf{x}_2)$. Now, plugging this result into (5.7) gives

$$\begin{aligned}\left(\tau_\pi\frac{\partial^2}{\partial t^2}+\frac{\partial}{\partial t}\right)r &= \nu\nabla_1^2\langle T_1^{0y}\delta\bar{T}_2^{0y}\rangle + \nu\nabla_2^2\langle\delta T_1^{0y}\bar{T}_2^{0y}\rangle + \Gamma \\ &= \nu\left(\nabla_1^2+\nabla_2^2\right)\langle T_1^{0y}\delta\bar{T}_2^{0y}\rangle \\ &+ \nu\left(\nabla_1^2+\nabla_2^2\right)\langle\delta T_1^{0y}\bar{T}_2^{0y}\rangle + \Gamma \\ &= \nu\left(\nabla_1^2+\nabla_2^2\right)r + \Gamma', \end{aligned} \tag{5.9}$$

where $\Gamma' = \Gamma - \nu\left(\nabla_1^2+\nabla_2^2\right)\langle\delta T_1^{0y}\delta T_2^{0y}\rangle$. In equilibrium ($r = r_{eql}$), the left-hand side vanishes. This means Γ' must satisfy

$$\Gamma' = -\nu\left(\nabla_1^2+\nabla_2^2\right)r_{eql} \tag{5.10}$$

Again, since the left side of (5.9) vanishes for r_{eql}, we finally obtain the second order diffusion equation for $\Delta r \equiv r - r_{eql}$:

$$\tau_\pi\frac{\partial^2\Delta r}{\partial t^2}+\frac{\partial\Delta r}{\partial t} = \nu(\nabla_1^2+\nabla_2^2)\Delta r \tag{5.11}$$

In the same way we can obtain the first order diffusion equation for Δr

$$\frac{\partial\Delta r}{\partial t} = \nu(\nabla_1^2+\nabla_2^2)\Delta r \tag{5.12}$$

The last equation, was first obtained and discussed in detail in [71]. The second order equation, Eqn. 5.11, is our new result. Note that a similar equation for correlation of multiplicity fluctuations was obtained in Ref. [65]. However, transverse momentum fluctuation is very different from multiplicity fluctuation. As is already pointed out earlier, transverse momentum is a conserved quantity while the number of particles is not. The underlying reasoning behind the derivation of these two causal diffusion equations is different.

We see that the two-particle transverse momentum correlation above the background thermal noise diffuses in the medium over time. The strength of diffusion, i.e., the diffusion coefficient is determined by the viscosity to entropy ratio η/s and the temperature. The ratio itself, in general, is a function of temperature. Viscosity, entropy density and their temperature dependence were discussed in Chapter 4. In short, the diffusion coefficient encapsulates all the information on the specific viscosity η/s of the medium.

To exploit the general techniques and simplicity offered by Bjorken boost invariant expansion, we want to write Eqn. (5.11) in boost invariant form. We do not use transverse expansion, as can be noted by the fact that we are already developing the equations in the forms suitable for longitudinal expansion. In Chapter 9, we will show that, as far as our integral observables (discussed in Chapter 6) are concerned, the transverse expansion integrates out and we do not loose generality by considering longitudinal expansion only. It should be noted that our current work is about the correlations in rapidity only, not the correlations in the azimuthal angle. Our current theory is therefore about a (1+1) dimensional (one space and one time dimension) boost invariant evolution of two-particle p_t correlations. To paraphrase again, our theory deals with longitudinal boost invariant evolution of Δr. It should be noted that, since its two-particle correlations, it is not just a (1+1) dimensional equation as far as numerical calculations are concerned. Even though we are using boost in-

variance, the diffusion equations are not independent of rapidity η. Computationally we still have three coordinates: η_1, η_2 and τ, with (1+1)D boost invariant hydrodynamics. This fact highlights the challenge of the full (3+1)D hydrodynamic model for two-particle p_t correlations.

In order to write Eqn. (5.11) in Bjorken boost invariant form we need to go over the linearization again but with the simplification of boost invariance and use the Milne coordinate. We recall from Section 3.5 that in the Milne coordinate system, $x^\mu = (\tau, x, y, \eta)$, and the four-flow is given by $u^\mu = (1, 0, 0, 0)$. We find that $D = u^\tau \partial_\tau + 0 = \partial_\tau$ and $\nabla_z^\mu \nabla_{z\mu} = (1/\tau^2)\partial^2/\partial\eta^2$. Thus instead of getting Eqn. (3.34), one gets

$$\tau_\pi \frac{\partial^2 \delta T_{0y}}{\partial \tau^2} + \frac{\partial \delta T_{0y}}{\partial \tau} = \nu \nabla_\eta^2 \delta T_{0y} \tag{5.13}$$

For two-particle correlations, as before, this finally leads to

$$\tau_\pi \frac{\partial^2 \Delta r}{\partial \tau^2} + \frac{\partial \Delta r}{\partial \tau} = \frac{\nu}{\tau^2}(\nabla_{\eta 1}^2 + \nabla_{\eta 2}^2)\Delta r \tag{5.14}$$

Eqn. 5.14 is the most important equation in our model. The diffusion coefficient ν and the relaxation time τ_π are temperature dependent and, hence, Eqn. 5.14 has a complicated dependence on time. Numerical solutions are the only options. We have discussed in detail the viscosity to entropy ratio in Chapters 3 and 4, and we know this ratio constitutes the diffusion coefficient ν and the relaxation time τ_π. The first order version can be obtained from the first order diffusion of δu^i discussed in Chapter 4, using the same method:

$$\frac{\partial \Delta r}{\partial \tau} = \frac{\nu}{\tau^2}(\nabla_{\eta 1}^2 + \nabla_{\eta 2}^2)\Delta r \tag{5.15}$$

Eqn. (5.15) was first derived in Ref.[71].

5.4 Relaxation time

The relaxation time is another transport coefficient. In our context here, it is the time in which the second order effects relaxes taking us back to the first order effects. Relaxation times are calculated from kinetic theory. Kinetic theory calculations for Boltzmann gas indicates that $\tau_\pi = 3\eta/2p$ [59]. For relativistic massless Boltzmann gas $\epsilon = 3p$ and this gives $\tau_\pi = 6\eta/Ts$. For massive Boltzmann gas it modifies to [59]

$$\tau_\pi = \frac{\eta}{Ts}\left(3 + \frac{T}{s}\frac{ds}{dT}\right) \tag{5.16}$$

For $s \propto T^3$, this again gives $\tau_\pi = 6\eta/Ts$. Let us write β for the ratio of τ_π to η/Ts,

$$\tau_\pi = \beta\frac{\eta}{Ts}. \tag{5.17}$$

Thus we see from the two simple examples here that $\beta = 6$ for kinetic theory. More extensive calculations can be found in Ref. [94], where τ_π depends on the coupling strength. The suggested value of β in this reference is between 5 to 6. Ref. [95] use a value as large as 6.32. Smaller values of β have also been used in some hydrodynamic models (see, for example [96, 97]). In this work, we use the kinetic theory value. We will show in Chapter 8, that this value of β, enables a better match with the experimental data.

We note that the relaxation coefficient for shear viscosity, τ_π (Eqn.(5.17)), is proportional to the diffusion coefficient ν (Eqn.(3.35)), with β as the constant of proportionality,

$$\tau_\pi = \beta\nu. \tag{5.18}$$

5.5 Diffusion and wave propagation

The value of $\beta \sim 6$ is a generic result of kinetic theory. Higher values of the relaxation coefficient as compared to the diffusion coefficient have interesting consequences. We will discuss them in Chapter 6. Here we note that the second order diffusion equation (5.11) is not just a diffusion equation. It has a propagating wave part as well. In absence of the second order time derivative, the equation is a regular (first order) diffusion equation. An initial function Δr, such as a gaussian, spreads out like a solution of a diffusion equation. On the other hand, if the first order time derivative vanishes, the equation is a typical wave equation. It describes the propagation of wavefronts in both directions. Therefore, the second order diffusion equation is expected to represent competing diffusion and propagating wave behavior. Higher values of β put more weight on the wave part, but at the same time reduces the propagation speed $\sqrt{\nu/\tau_\pi}$. In rapidity space (i.e., if we use (5.14), diffusion effects are further suppressed because of the $1/\tau^2$ factor attached to the diffusion coefficient.

The feature of competing wave and diffusion is, obviously, absent in the first order theory, which has only diffusion. The consequences of this feature of the second order theory in our observables will be discussed in detail in Chapter 8.

CHAPTER 6

CORRELATION OBSERVABLES

In Chapter 5, we developed the equations that describe the hydrodynamic evolution of two-particle p_t correlations. We showed that second order Israel-Stewart hydrodynamics and first order Navier-Stokes hydrodynamics, respectively, lead to second order diffusion equation and first order regular diffusion equation for Δr. We observed that these equations turn out to be deterministic despite the fact that the local equilibrium value r_{eql} is not zero due to stochastic thermal noise. The first order diffusion of δr was developed in Ref. [71]. The second order equation for Δr is our new result and is the main framework for our theory. The second order diffusion applied to charge fluctuations is first developed in Ref. [65].

In this chapter, we begin by discussing the main observables that connect our theoretical model with experimental measurements. One observable is the quantity $\mathcal{C}$, described in detail in the following section. The other important observable is the width of Δr. These observables are first developed and discussed in Ref. [71]. We follow this reference in our discussion here. The concept and method developed in Ref. [71] have actually stimulated experimental measurements by STAR [43]. These are the measurements of the observables we just mentioned. The STAR results have proven to be a valuable resource for testing the calculations based on our model. We discuss the experimental results in this chapter and compare them with our computations in Chapter 8.

We discuss the definition of the observables in Section 6.1. The analysis of these observables by STAR is discussed in Section 6.2. Finally, in Section 6.3, we discuss computations by the NEXSPHERIO group and the results relevant for our own computations.

6.1 Observables

6.1.1 p_t covariance, $\mathcal{C}$

We demonstrated in Chapter 5 that the quantity Δr obeys deterministic diffusion equations. Navier-Stokes theory leads to regular diffusion equation while Israel-Stewart second order theory leads to the second order diffusion equation for Δr. Recall from Section 5.3 that the diffusion equations for the correlation function r contain the Langevin noise. The equations for Δr are, nonetheless, deterministic since the background thermal noise cancels out. In Ref. [71], Gavin and Abdel-Aziz have demonstrated how the quantity Δr may be used to obtain the observables and thus established a connection with the experimental measurements. One of the observables they proposed is the transverse momentum covariance, or p_t covariance, $\mathcal{C}$, given by

$$\mathcal{C} = \langle N \rangle^{-2} \langle \sum_{i \neq j} p_{ti} p_{tj} \rangle - \langle p_t \rangle^2 \tag{6.1}$$

Here $\langle p_t \rangle$ is the average transverse momentum: $\sum \langle p_{ti} \rangle / \langle N \rangle$. The brackets represent the event average. The index i labels particles in each event. At local equilibrium momenta are uncorrelated, the number fluctuations satisfy Poisson statistics and $\mathcal{C}$ should vanish.

It should be noted that $\mathcal{C}$ is slightly different form the p_t covariance or correlation function measured by many experiments. For example, STAR previously measured the differential p_t correlation [98, 99]

$$\langle \delta p_{t1} \delta p_{t2} \rangle = \frac{\langle \sum_{i \neq j} \delta p_{ti} \delta p_{tj} \rangle}{\langle N(N-1) \rangle} = \int d\mathbf{p_1} d\mathbf{p_2} \frac{\Delta\rho(\mathbf{p_1}, \mathbf{p_2})}{\langle N(N-1) \rangle} \delta p_{t1} \delta p_{t2} \tag{6.2}$$

Here, $\delta p_{ti} = p_{ti} - \langle p_t \rangle$ and $\Delta\rho(\mathbf{p_1}, \mathbf{p_2})$ is the correlation function

$$\Delta\rho(\mathbf{p_1}, \mathbf{p_2}) = \rho_2(\mathbf{p_1}, \mathbf{p_2}) - \rho_1(\mathbf{p_1}) \rho_1(\mathbf{p_2}) \tag{6.3}$$

with $\rho_2(\mathbf{p_1}, \mathbf{p_2}) = dN/dy_1 d^2p_{t1} dy_2 d^2p_{t2}$ and $\rho_1 = dN/dy d^2p_t$ respectively being the densities of pairs and single particles. The correlation measured by $\mathcal{C}$ is different from that given by Eqn. (6.2) and other p_t correlations used in RHIC experimental analyses in that $\mathcal{C}$ is more sensitive not only to number density fluctuations but also to p_t fluctuations because of its explicit dependence on particle momenta [43, 100].

The relation of the observable $\mathcal{C}$ to Δr, as established in Ref. [71], is given by

$$\mathcal{C} = \langle N \rangle^{-2} \int \Delta r(\mathbf{x_1}, \mathbf{x_2}) d^3x_1 d^3x_2 \tag{6.4}$$

Thus, $\mathcal{C}$ is obtained by integrating Δr over space and normalizing with $\langle N \rangle^2$. Recall that r is the correlation of two-particle momentum current T_{0i}. It can be written as an integral of a phase space distribution function over the momenta

$$T_{0i} = \int \frac{d^3p}{(2\pi)^3} f(\mathbf{x_1}, \mathbf{x_2}) p_t \tag{6.5}$$

We numerically solve the diffusion equations for Δr taking into account the temperature and time dependence of the transport and relaxation coefficients, as well as different equations of state. The solutions obtained are Δr, which are then integrated to compute the observable $\mathcal{C}$.

6.1.2 Correlation width σ

The correlation width is another important observable that can be measured from experiments. From the solutions Δr, we first calculate the variance. We use this standard relation:

$$V = \langle \eta^2 \rangle - \langle \eta \rangle^2 = \frac{\int (\Delta r)^2 d\eta_1 d\eta_2}{\int d\eta_1 d\eta_2} - \left(\frac{\int \Delta r d\eta_1 d\eta_2}{\int d\eta_1 d\eta_2} \right)^2 \tag{6.6}$$

The width is then taken as $\sigma = \sqrt{V}$.

The STAR group has measured correlation widths at different centralities [43]. In Section 6.2, we discuss their results. We present our computed results and compare with the experimentally measured values in Chapter 8.

In Ref. [71], the width is an observable used to estimate the value of the specific viscosity, η/s, of quark-gluon plasma. In this reference, Gavin and Abdel-Azis develop the first order deterministic diffusion equation of Δr and use Bjorken invariant expansion to obtain the width of two-particle p_t correlations. They demonstrated that the viscosity of the medium broadens the correlation width, and this very broadening can be used to estimate η/s. Their calculations show that the width increases with time τ starting from some initial value τ_0 according to

$$\Delta V \equiv \sigma^2 - \sigma_0^2 = 4\nu \left(\frac{1}{\tau_0} - \frac{1}{\tau} \right) \tag{6.7}$$

If we consider the whole course of hydrodynamic evolution, the final time τ in Eqn. 6.7 can be naively identified with the freeze out time τ_F. Experimentally, the width at τ_F can be identified with the width of $\mathcal{C}$ for the most peripheral collisions and that at τ_0 with width for the most central collision, as suggested in the this reference. Thus from the measurable width one can estimate η/s. It is clear that the final width depends on the η/s and the life time of the quark-gluon plasma. This method for extracting η/s is clearly different from the traditional methods that use the flow data (see for example, [101] and [102] for latest estimates). The uncertainties like initial conditions, freeze-out and event-by-event fluctuations demand more than just one method. This alternate method, in fact, motivated the STAR measurement of Ref. [43]. This experimental measurements provided a range for the values for η/s, that are obtained from the flow data. In addition, they have provided a wealth of data on correlation amplitude $\mathcal{C}$ and width σ for various centralities. These data have proven to be very important to our current work.

Estimation of η/s, however, is not the main point of our work in this dissertation. Our work here has a broader goal. We study hydrodynamic response and behavior of the system and its effects on correlations, with the focus on the p_t correlations in rapidity.

6.1.3 The offsets

We recall that the diffusion equations of Δr are linear homogenous equations. This means that if Δr is a solution, then $A + B\Delta r$, where A and B are constants, is also a solution. The constant A can be thought of as a pedestal over which the distribution Δr stands on. It is called the "offset". We attempt to identify this offset as a part of the long range correlation in $\Delta\eta$, known as the "ridge". Ridges are discussed in detail in Chapter 2.

As already discussed in Chapter 2, the ridge measured by STAR [38, 103], extends to about 3 relative rapidity units (about -1.5 to 1.5) and that measured by PHOBOS [44] extends from -4 to +2 in $\Delta\eta$, (see Fig.6.1). As we have pointed out earlier, it is very unlikely that hydrodynamics plays a role in the long range correlation. This is because correlations in the large rapidities are causally disconnected. The long range correlation of the ridge must have its origin in the initial conditions, or before thermalization. However, a part of the ridge is present as baseline of the short range correlation around $\Delta\eta \sim 0$. In other words, a part of the ridge which is present at large rapidities serves as the pedestal of the short range correlations where hydrodynamics contribute.

We have mentioned in Chapter 2 that there have been attempts to explain the ridge. One explanation, for the ridge in $\Delta\eta$, is based on flux tubes and glasma [40]. According to this interpretation, the long range correlations in $\Delta\eta$, result from particles produced in the same flux tube. They emanate from the same transverse position irrespective of their relative rapidity. Their transverse momenta are then

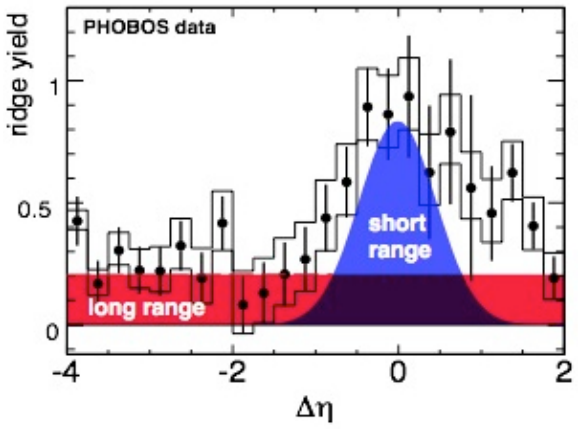

Figure 6.1: Long and short range correlations in PHOBOS measurements for Au+Au at $\sqrt{s} = 200$ GeV. Taken from S. Gavin's presentation at Initial State Fluctuations and Final State Correlations in Heavy Ion Collisions (2012), Trento, Italy. This figure itself is adapted from the PHOBOS paper of Ref. [44].

correlated even for long rapidity ranges and, hence, a ridge in $\Delta\eta$. It is therefore natural to assume that the same mechanism must also play a role in short range correlations and the corresponding part of the ridge. On top of this part of the ridge lies the modification from the various factors like jets, resonance decays, freeze out, and most importantly from hydrodynamic evolution. The correlations in our study is are short range correlations and our focus is on the role of viscous hydrodynamic evolution.

We will see in Chapter 8 that our hydrodynamic calculations reproduce the correlations in the window of $\Delta\eta \sim 2$, and we identify the constant A as the part of the ridge in this window. The STAR analysis of Ref. [43] also uses a constant baseline or offset for the correlations. The use of a flat offset is not the only approach though. The STAR analysis of Cu-Cu collision data of Ref. [104], for example, uses a wide Gaussian offset.

6.2 Correlation observables measured by STAR

As pointed out earlier, the suggestion of an alternate method for estimating η/s of quark-gluon plasma in Ref. [40] motivated an experimental analysis from the STAR group [43]. In their analysis to measure the rapidity profile of the correlation observable $\mathcal{C}$, they fit the peak with a double gaussian and a constant baseline. The baseline or offset can be identified as the part of the ridge in the rapidity window of the measurements.

The STAR group also reported the rms width of the near side peak of two-particle correlations. For the most central collision, their measured value is $\sigma_{central} = 1.0 \pm 0.2$. For the peripheral collision the measurement is $\sigma_{pepheral} = 1.0 \pm 0.2$. From the rms width of the peak, they estimated the ratio of viscosity to entropy density to be of the order of 0.17 ± 0.08. This value is well within range of the values obtained from flow data (see [40] and references therein).

Fig. 6.2 shows the observable $\mathcal{C}$. Notice that the systematic errors are mostly on the offsets. Also, note a lone data point, off from the general trend of the other data points, in the case of the most central collision. The reason for the deviation of this point has been ascribed to track merging [43], and is, therefore, a detector artifact.

Fig. 6.3 shows the experimentally measured width as a function of the number of participants. We know that the evolution time for more central collisions, which corresponds to the larger number of participants and multiplicity, is longer. Similarly, the most peripheral case has almost no evolution time.

In addition to the peaks, Ref. [43], also gives the baseline or offset. We already know that offsets make yet another observable and will be discussed in Section 6.1.3. In the experimental measurements [43], the correlation profiles and the base lines are fit according to

$$\mathcal{C}(b, a_w, \sigma_w, a_n, \sigma_n) = b + a_w \exp(-\Delta\eta^2/2\sigma_w^2) + a_n \exp(-\Delta\eta^2/2\sigma_n^2) \qquad (6.8)$$

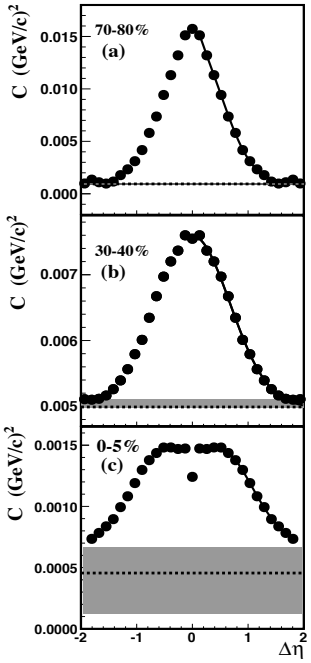

Figure 6.2: STAR result: Projection of the covariance $\mathcal{C}$ for $|\Delta\phi| < 1.0$ radians on $\Delta\eta$ axis for three centralities shown in the plots. The results are for Au-Au collisions at $\sqrt{s} = 200$ GeV. This figure is taken from [43].

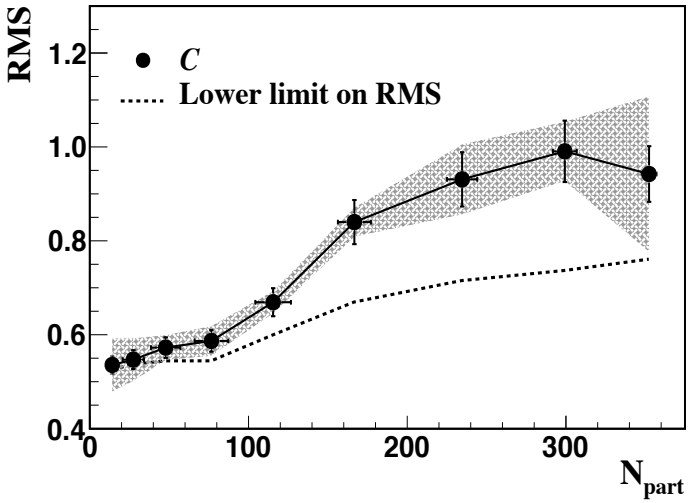

Figure 6.3: STAR result: rms width as a function of number of participant. The dotted line represents the absolute lower limit and the shaded band represents systematic uncertainties. The results are for Au+Au collisions at $\sqrt{s} = 200$ GeV. This figure is taken from [43].

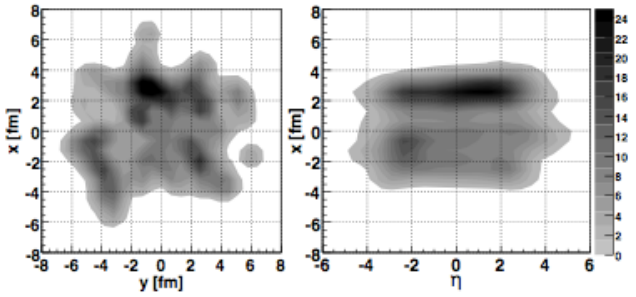

Figure 6.4: Transverse and longitudinal profile of initial energy density distribution in GeV/fm^3 generated using NEXUS code, for $\sqrt{s} = 200$ GeV Au+Au collisions with centrality of top 10%. This figure is taken from [107].

Here b is the baseline or the offset, a_w and a_n are the amplitudes of the wide and narrow Gaussians used for the fit. The widths of the Gaussians are σ_w and σ_n, respectively. We should note here that a flat offset, given by b in Eqn. 6.8, has been applied here.

6.3 Observables computed by NEXSPHERIO

NEXSPHERIO is a combination of the computational codes SPHERIO [105] and NeXUS [106] developed by the Sao Paulo and Rio de Janeiro collaboration. SPHERIO is a relativistic hydrodynamic code that uses Smoothed Particle Hydrodynamics (SPH) originally developed for astrophysics and later adapted for the hydrodynamics of heavy ion collisions. NEXUS is a Monte Carlo code that generates smooth and fluctuating initial conditions using Monte Carlo string fragmentation model called NEXUS. Figure 6.4, taken from the Ref. [107], shows an example of an initial energy density profile created by the NEXUS code. Thus NEXSPHERIO codes generates a fluctuating initial conditions and simulates hydrodynamic evolution starting from those initial conditions.

NEXSPHERIO model computations have been shown to describe many features of correlations, including anisotropic flow, and azimuthal correlations, the shape of the ridge [107, 108, 105].

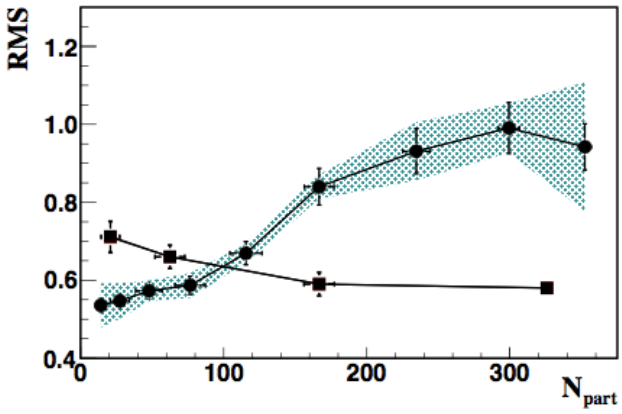

Figure 6.5: NEXSPHERIO computations vs STAR results on RMS widths. The lower line is results from NEXSPHERIO, which uses equations of inviscid hydrodynamics. The figure is taken from [100]. NEXSPHERIO computations show narrowing instead of increasing width shown by STAR data.

In the context of our work, NEXSHERIO results have two important relevant points. First, in our hydrodynamic theory, we have not included the ideal hydrodynamics. In their results for the same correlation observables, it is important to check if any effect that we ascribe to viscous dissipation are present or not. Second, their computation include the resonances and we can see if there is any effect of resonances, especially, on the width of the correlation.

Fig. 6.5 shows the correlation widths computed by NEXPHERIO and compares them with the STAR data discussed in the previous section. Is is clear from this result that, first, there is no broadening of the width with increasing centrality. Interestingly, the width slightly narrows instead. Second, the resonances, appears to have no broadening effect. The later observation is important to us since it removes some doubt on whether is any effect of resonance decays in our own correlation widths.

CHAPTER 7

INITIAL CONDITIONS AND PARAMETERS

In this chapter we state and discuss the assumptions and parameters used in the theory, especially in the context of numerical computations. However, before we get there, we start with summarizing the main equations we use in our computations. In Section 7.1, we give the summary of these equations. Then in Section 7.2, we discuss these parameters and assumptions. Finally, we briefly discuss our numerical methods.

7.1 Summary of major equations used in computation

The following is the summary of equations that we use in our numerical computations. Results of the numerical computations are presented in Chapter 8.

First order diffusion of Δr in coordinate space:

$$\frac{\partial \Delta r}{\partial t} = \nu(\nabla_1^2 + \nabla_2^2)\Delta r \tag{5.12}$$

The same equation in rapidity space:

$$\frac{\partial \Delta r}{\partial \tau} = \frac{\nu}{\tau^2}(\nabla_{\eta 1}^2 + \nabla_{\eta 2}^2)\Delta r \tag{5.15}$$

The second order diffusion equations for Δr in the same order:

$$\tau_\pi \frac{\partial^2 \Delta r}{\partial t^2} + \frac{\partial \Delta r}{\partial t} = \nu(\nabla_1^2 + \nabla_2^2)\Delta r \tag{5.11}$$

$$\tau_\pi \frac{\partial^2 \Delta r}{\partial \tau^2} + \frac{\partial \Delta r}{\partial \tau} = \frac{\nu}{\tau^2}(\nabla_{\eta 1}^2 + \nabla_{\eta 2}^2)\Delta r \tag{5.14}$$

Viscosity as a function of temperature:

$$\eta(T) = \begin{cases} [1 + w(T)\ \ln(T/T_C)]^2 T^3 & \text{for } T > T_C, \\ T_C^2 T & \text{for } T \leq T_C. \end{cases} \tag{4.1}$$

Entropy density for EOS I is from lattice QCD calculations [86, 11] and is discussed in Section 4.2. For EOS II entropy density is:

$$s = \begin{cases} 4\pi T^{1/c_s^2} & \text{for } T > T_C, \\ \frac{4\pi}{a}[f(a-1)+1]T_C^3 & \text{for } T = T_C, \\ (\frac{4\pi}{a})T^{1/c_H^2} & \text{for } T < T_C. \end{cases} \tag{4.2}$$

The strength of diffusion, the diffusion coefficient ν, is determined by η/s. The relaxation time is proportional to ν:

$$\nu = \frac{\eta}{Ts} \tag{3.35}$$

$$\tau_\pi = \beta \frac{\eta}{Ts} = \beta\nu. \tag{5.17}$$

Time evolution of entropy density:

$$\frac{ds}{d\tau} + \frac{s}{\tau} = \frac{\pi}{T\tau}. \tag{4.4}$$

For first order theory π is given by

$$\pi = \frac{4\eta}{3\tau} \tag{4.5}$$

And, for the second order theory π is the solution of this differential equation:

$$\tau_\pi \frac{d\pi}{d\tau} + \left(1 + \frac{\tau_\pi}{2\tau} + \frac{1}{2}\eta T \frac{d}{d\tau}(\frac{\tau_\pi}{\eta T})\right)\pi = \frac{4\eta}{3\tau} \tag{4.8}$$

Experimental observable, transverse momentum covariance:

$$\mathcal{C} = \langle N \rangle^{-2} \langle \sum_{i \neq j} p_{ti} p_{tj} \rangle - \langle p_t \rangle^2 \tag{6.1}$$

The connection between experimental and theoretical observables, $\mathcal{C}$ and Δr:

$$\mathcal{C} = \langle N \rangle^{-2} \int \Delta r(\mathbf{x_1}, \mathbf{x_2}) d^3x_1 dx_2^3 \tag{6.6}$$

7.2 Initial conditions and parameters

In order to obtain the correlation observables, first we need to solve the first and second order diffusion equations for Δr. Recall that the diffusion coefficient ν contains the viscous dissipation information. It has an intricate temperature and hence time dependence, as discussed in Chapter 4. This makes it impossible to analytically solve even the first order diffusion equation. The second order gets even more complicated. We must use a numerical method to solve these equations. Temperature dependence of η/s is discussed in detail in Chapter 4. Entropy density as a function of time is a solution of Eqn.(4.4) where the quantity π, in the case of second order theory, is a solution of Eqn.(4.8). For the simple first order Navier-Stoke case π is given by Eqn.(4.5).

Rapidity dependence of correlation functions are expressed in rapidity widths. We, therefore, solve equations in relative rapidity coordinates rather that the individual rapidity coordinates of the two particles being correlated. The relative and average rapidities of two particles at η_1 and η_2 are

$$\Delta\eta = \eta_1 - \eta_2 \qquad\qquad \eta_a = \frac{1}{2}(\eta_1 + \eta_2). \tag{7.1}$$

Note again hat our notation for spacetime rapidity and coefficient of viscosity are the

same. As mentioned before, there should not be any confusion because of the context of their use.

We take the initial correlation function (over the thermal background noise), Δr, as a gaussian given by

$$\Delta r(\Delta\eta, \eta_a, \tau_0) \propto \exp(-\Delta\eta^2/2\sigma_0^2 - \eta_a^2/2\Sigma_0^2), \tag{7.2}$$

where σ_0 and Σ_0 are initial widths of Δr in $\Delta\eta$ and η_a, respectively. This is the same initial condition that is used in Ref. [71]. The scale of Σ_0 is of the order of the system size and we take $\sigma_0 \ll \Sigma_0$. Specifically, in our numerical solution we have used $\sigma_0 = 0.54$ to make it consistent with the experimental data (the STAR data we discussed in Section 6.2) for the most peripheral collisions. We have assumed that the time rate of change of correlation at the beginning is zero: $\partial\Delta r/\partial\tau|_{\tau_0} = 0$. In solving the entropy production equations we naturally take the initial entropy density to be the entropy density corresponding to the initial temperature, for both equations of states. The initial value of $\partial\pi/\partial\tau$ in Eqn (5.14) is taken to be the corresponding value for the Navier-Stokes case: $\pi(\tau_0) = 4\eta/3\tau$.

As we have already noted here and discussed in detail in Section 5.4, the relaxation time τ_π is proportional to the diffusion coefficient ν. The proportionality constant β in Eqn. (5.17) is taken as $\beta = 6$, in accordance with kinetic theory calculations, as mentioned in Section 5.4. In that section, we have also pointed out that there are some hydrodynamic models which use values much smaller than the kinetic theory values. We, however, proceed exclusively with the kinetic theory values.

The initial or thermalization time (proper time, to be precise), which we denote by τ_0, is taken to be $\tau_0 = 1$ fm. Starting from this time, the system undergoes hydrodynamic expansion before the quark-gluon plasma freezes out into a stream of hadrons. Note that our theory does not include the so called 'after burner'. The

hadrons, mostly pions, ultimately end up in the detector. Hydrodynamics breaks at the freezeout. In our model we assume that freeze out occurs at a constant temperature, T_F. We basically make the hydrodynamic evolution stop at T_F, where $T_F = 150$ MeV in our model.

We run the numerical codes to solve the equations at different impact parameters b. The impact parameters range from $b = 0$ to $b = b_{max}$, which is divided in a number of intervals or bins, typically 100. We take $b_{max} = 12.8$ fm, the maximum impact parameter listed by STAR (in Ref. [109]) for $\sqrt{s} = 200GeV$ Au-Au collisions. The STAR reference uses Monte-Carlo Glauber calculations to connect the impact parameters to the number of participants. In our work, we have used the optical Glauber model for this purpose.

How long a system evolves hydrodynamically depends on the freezeout time τ_F, which is different for different centralities. The matter created in the most central collision has longer hydrodynamic evolution. We have taken the longest time τ_{Fc}, the freeze out time for the most central collisions, to be $\tau_{Fc} = 9$ fm. The evolution time reduces quickly as we go from the most central to the peripheral cases. We have assumed that the freeze out time is proportional to average participant area, $\tau_F - \tau_0 \propto (R_{max} - R_{min})^2$. This is one of our assumptions and its validity ultimately lies with whether or not it accords with experimental data.

7.3 A brief note on computation

A major part of the numerical solver consists of codes for solving the diffusion equations and the entropy equations - the first and second order. For diffusion equations as well as the entropy production, both first and second order, we use explicit forward time centered space method. With our values of diffusions coefficient, space and time grid sizes used, we obtained stable solution for our obviously short time period of evolution. The results presented in Chapter 8, especially the profiles of

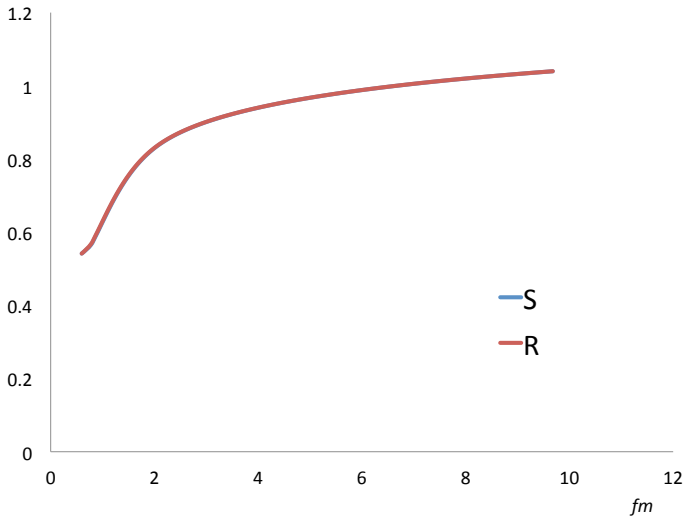

Figure 7.1: Widths calculated from two different method. The letter R labels the solution obtained by solving the partial differential method, and S labels the solution obtained differently, see text for detail.

correlation show our solutions were stable in the overall short evolution time.

First, let us briefly mention our numerical method and test of its validity. A test of correctness of our codes involves the calculation of correlation widths by two very different methods. The first method is to integrate the solutions Δr that we obtain from our diffusion equation and calculate moments and hence widths. The second method is to integrate the equations themselves, make the "surface terms" vanish by taking the surface to 'infinity'. The second method is used to derive the evolution equation for variance in Ref. [65]. It should be noted that the later method is useful for finding width only. Fig. 7.1, shows the evolution of width calculated from the second order diffusion equation using these two very different methods. We observe that the solutions perfectly overlap. This is one of the strong bases for the confidence in our numerical method.

In the case of EOS II, the viscosity and entropy density are both known functions of temperature, expressed by Eqns. 4.2 and 4.1. Using the entropy production equation, Eqn. 4.4 (with π given by Eqns. 4.5 and 4.8 for the first order and second order entropy equations, respectively), the ratio η/s can be evaluated as a function of proper

time. Then equation 3.35 is used for evaluating the diffusion coefficient as a function of time. To solve the second order equation, one also needs the relaxation time τ_π, which is a function of time as well, via Eqn. 5.17. Gathering all this information, the diffusion equations are solved for one value of impact parameter or centrality. The solutions are Δr, which are then integrated to compute the moments. The second moment is the variance which gives the width. This is iterated over the number of intervals we have divided the the impact parameters into. The impact parameters vary between 0 and $b_{max} = 12.8 fm$.

CHAPTER 8

COMPUTATIONAL RESULTS AND DISCUSSION

In this chapter, we will present, discuss, and explain the results of our numerical computations. Note that we summarized the main equations, the initial conditions and the parameters used in our numerical computations in Chapter 7.

First we start with a discussion, in section 8.1, of some of the interesting generic features forced by causal constraints upon the diffusion equation. These features constitute an important aspect in the final results. In Section 8.2, we once again briefly discuss the temperature dependence of the transport coefficients. Then we discuss the experimentally measured values of our observables. The observables are discussed in detail in Chapter 7. Since our theory is about viscous hydrodynamics and viscosity gives rise to diffusion of correlation, ideal hydrodynamics is not a part of our theory. In order to compare with ideal hydrodynamic calculations we use the results by NEXSPHERIO group. As mentioned briefly in Secction 6.3, NEXSPHERIO code employs fluctuating initial condition and inviscid hydrodynamics.

8.1 Waves versus diffusion

We observed in Chapter 3, how the need for maintaining causality forces us to look for second order Israel-Stewart hydrodynamics from the first order Navier-Stokes theory. In our context of transverse flow and momentum fluctuations, the second order corrections lead to causal or second order diffusion equations. We have seen that the causality constraint introduces another transport coefficient - the relaxation time. The second order time derivative, that contains the relaxation time, significantly alters the nature of the diffusion equation. The causal diffusion equation is a hyperbolic equation - not the usual parabolic diffusion equation. If we look at the extra second

order time derivative term in Eqn.(5.11), we observe that this equation incorporates propagating waves as well. If the first order time derivative vanishes, it reduces to a wave equation with wavefronts propagating away from the center at the characteristic speed of $\sqrt{\nu/\tau_\pi}$. On the other hand, in the limit of vanishing relaxation time, the equation reverts to the the regular diffusion equation, without any propagating waves. The solution "spreads" out with time, as we know very well from the textbook example of the heat equation solution.

The second order diffusion equation is not a new concept. In mathematics, it is a standard equation known as the *telegraph equation*. The causal theory of hydrodynamics has been used for modeling the evolution of the matter created in heavy ion collisions for about a decade (for example, see [64, 65, 70, 97]). Part of our work is also related to looking at aspects of the wave and diffusion parts of the equation and examining their consequence to the observables. We discuss the consequences in later sections. In this section, we want to show the competing wave and diffusion parts embodied in the causal diffusion equations. We first note that our equation is more complicated than the telegraph equation since the relaxation time and the diffusion coefficient in our equation are complicated functions of time, obtained in pieces from the temperature dependence of the transport coefficients and entropy density.

Figure 8.1 illustrates the wave and diffusion effects. The characteristic wavefronts propagate away leaving behind more and more empty space. On the other hand, the diffusion spreads and the initial function, say a gaussian, broadens with time. We, therefore, expect that the overall effect is a combination of these two different trends. The spreading of initial correlation by diffusion fills in the space left behind by the propagating waves.

Fig. 8.2 shows the solutions obtained from the actual numerical computations using Eqn. 5.11, the equation in coordinate space, and for special case of a constant $\nu = \eta/Ts$ and, hence, constant τ_π. The combination of the diffusion and wave effects

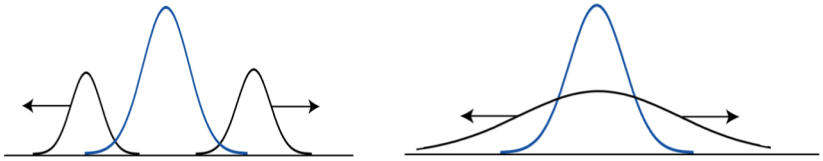

Figure 8.1: Wave vs diffusion effects of second order diffusion equation. Waves propagates away from the center leaving behind empty space while the diffusion fills the space by spreading the initial peak over time. Image: Sean Gavin.

can be seen clearly: the wave fronts recede away, while the diffusion part fills the space in between them.

In the rapidity space version, Eqn. 5.14, which incorporates Bjorken longitudinal expansion, one can notice the factor $1/\tau^2$ attached to the diffusion coefficient. This means that the effective diffusion coefficient gets smaller and smaller with time. The diffusion part, therefore, does not appear to fill up the space in between as it does in the case of coordinate space. Also, the effective wave speed $\sqrt{\nu/\tau_\pi}$ gets smaller with proper time. And, finally, there is an effect associated with the Bjorken expansion velocity $v = z/t$. The overall effect is that the propagation saturates and the diffusion does not fill up the gap as much as in the case of coordinate space solutions as, seen Fig. 8.3.

The telegraph equation (i.e, the causal diffusion equation constant coefficients) has analytical solution [110]. Fig. 8.4 shows the surface plot of the semi-analytical solution of the telegraph equation. It is "semi-analytical" because the integral of the Bessel function of the second kind involved in the analytical solution was performed numerically. We notice that the solution of generic telegraphic solution incorporates both wave and diffusion effects.

As already noted, the relaxation time is β times the diffusion coefficient ν. As discussed in Sections 5.4 and 7.2, we take $\beta = 6$. The high value of β demanded by

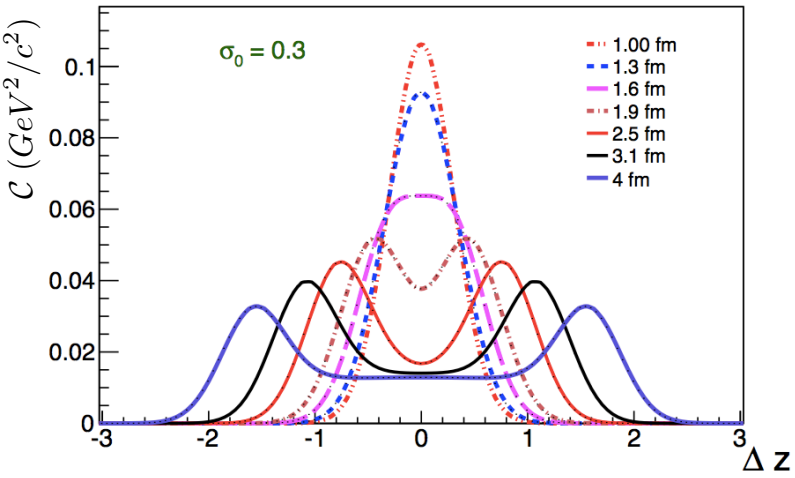

Figure 8.2: Wave vs. diffusion effects of the second order diffusion equation in coordinate space. Waves propagate away from the center leaving behind empty space while diffusion fills the space by spreading the initial peak with time. Width of initial gaussian is $\sigma_0 = 3$ and ν and τ_π are constant for these plots.

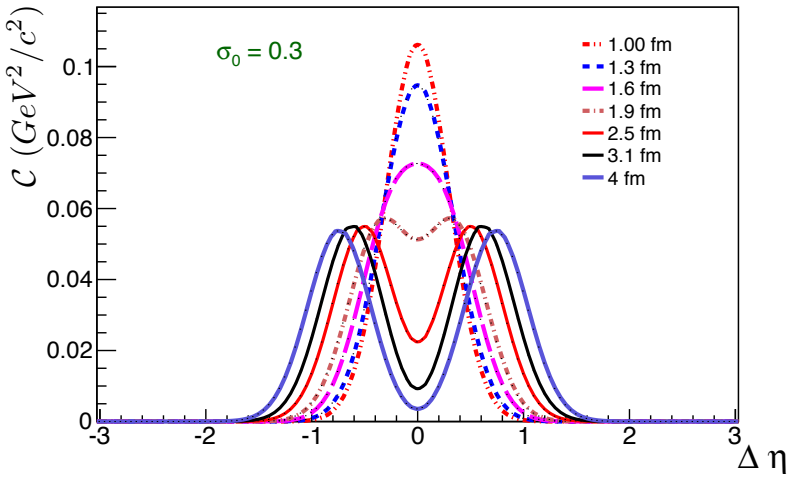

Figure 8.3: Wave vs. diffusion effects of the second order diffusion equation in rapidity space. This appears different from Fig. 8.2, though the physics is the same. See the text for explanation.

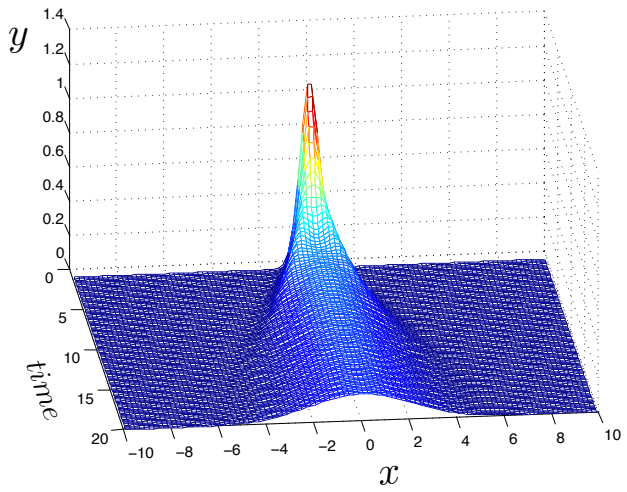

Figure 8.4: Wave vs. diffusion effects in the telegraph equation (a simple, generic causal diffusion equation with constant coefficients). The solution of telegraph equation is y in one dimensional space x. The quantities are in arbitrary units. We notice the wave going outward while the diffusion fills up the space. Initial function is a narrow Gaussian. The scales are, however, not related to Figs. 8.2. The wave part in this figure is given less weight than than diffusion, as compared to Fig. 8.3, where a high value of τ_π is demanded by kinetic theory.

kinetic theory puts a significantly bigger weight on the wave part compared to the diffusion part. As a result, we observe the wave dominating the diffusion part in the examples of Fig. 8.2 and Fig. 8.3.

8.2 Diffusion and relaxation coefficients and centrality

We have taken the constant temperature freeze out at $T_F = 150$ MeV. The initial temperature T_0 depends on the centrality. The more central the collision, the higher the initial temperature of the system. The higher the initial temperature, the longer the evolution time for the system. Thus, the hydrodynamic evolution time for the system, before the freeze out at 150 MeV, depends on the centrality.

As mentioned in Chapter 7, we have taken the freeze out time for the most central collision to be 9 fm. The diffusion coefficient, $\nu = \eta/Ts$, depends on temperature. This means that the strength of the diffusion depends on the centrality of the colli-

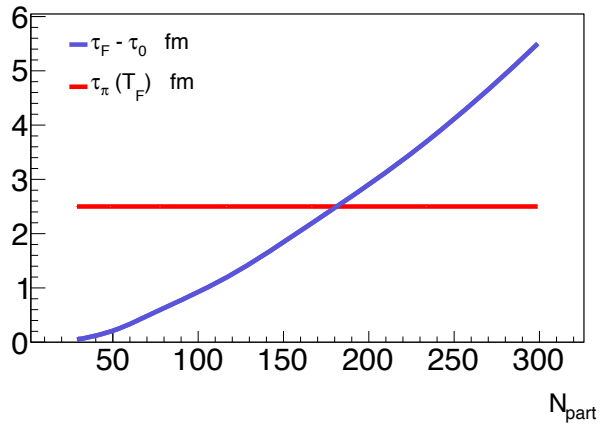

Figure 8.5: Evolution time $\tau - \tau_0$ and relaxation time τ_π plotted against centralities. The relaxation time shown here is evaluated at the freeze out temperature. Since freeze out temperature is taken to be constant, relaxation time shown here is constant.

sions. However, it should be noted that at freeze out the diffusion coefficient is the same for all centralities since we are at the same freeze out temperature T_F. Notice the relaxation time, $\tau_\pi = \beta\nu$, shows the same behavior (i.e., constant for all centralities).

Figure 8.5 shows the evolution time and relaxation time at freeze out vs centrality. We observe that for peripheral collisions the evolution time becomes shorter than the relaxation time. Recall that the relaxation time is the time needed for the system to relax to the first order Navier-Stoke case. We discuss this situation in the section on width of correlation below.

8.3 Observables and comparison with experimental data

We discussed the observables in Chapter 6. Here we are presenting the observables computed from our theory. In addition, we compare our results with the STAR experimental data [43]. Note again that the details on the initial conditions, assumptions and parameters are in Chapter 7.

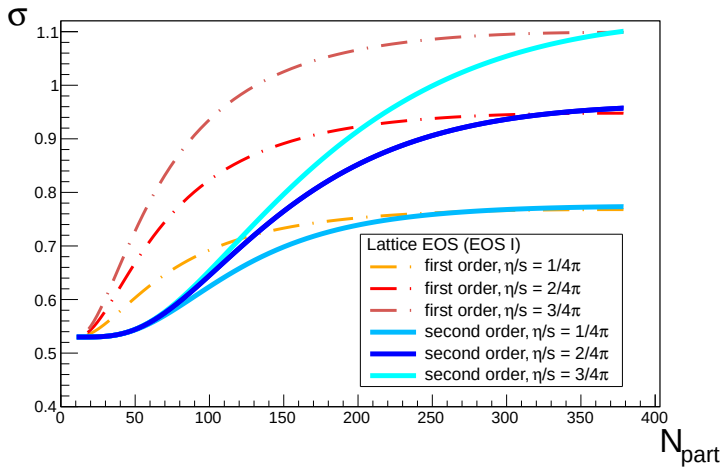

Figure 8.6: p_t-correlation widths calculated from first and second order diffusion equations using constant η/s. The lowest value $\eta/s = 1/4\pi$ is the KSS bound. Equation of state used is the the equation of state based on lattice QCD calculations (EOS I).

8.3.1 Correlation width

Correlation width σ is one of our most important observables. In Section 6.1.2, we discussed this observable in detail along with the STAR measurements of this quantity. Here we present our theoretical results, computed directly by solving the diffusion equations, both first and second order. We also compare our results with the experimental data.

Before we present our general results on how width varies with centralities, we would like to show how the width varies with centrality for a special case of constant η/s. Note that constant η/s does not make the diffusion coefficient a constant since temperature is also a factor there: $\nu = \eta/Ts$. Figure 8.6 shows the results for η/s equal to 1, 2 and 3 times the KSS bound $\eta/s = 1/4\pi$. The results are from both the first and second order diffusion equations. The equation of state is EOS I, i.e., the one that uses lattice QCD calculations. The two equations of state we have used are explained in Chapter 4. The second order entropy equation is used for second order diffusion, while the first order entropy equation is used for first order diffusion.

We already know from the work of Gavin and Abdel Aziz [71], that the viscous medium responds to the initial-p_t correlation by broadening its width with increased evolution time and, hence, with increased centrality. Different values of η/s should lead to different amount of broadening. Such broadening of width, using the results of the first order diffusion equation, is already discussed in the Ref. [71]. Note, however that this reference uses constant diffusion coefficient η/Ts, not constant η/s. The effect of different constant η/s to the width from our computations is shown in Fig. 8.6. The values of η/s chosen are the KSS bound ($\eta/s = 1/4\pi$) and its next two multiples, as indicated. These widths are calculated using both the first and the second order diffusion equations and the lattice QCD based equation of state (EOS I). This result shows that response of the system is well sensitive to values of η/s, and also that the first and the second order diffusion gives significant differences except for the cases of the most central collisions.

We now move on to the general case of temperature dependent η/s. The results are shown in Fig. 8.7. It also includes the width measured by STAR [43] and that computed by NEXSPEHERIO using ideal hydrodynamics with fluctuating initial conditions. STAR results are discussed in detail in Section 6.2. NEXSPEHERIO computation is discussed in Section 6.3. Widths are computed using both equations of state, EOS I and EOS II. As explained in Chapter 4, EOS II is the conventional equation of state based on the Bag Model.

In Fig. 8.7, we first notice that using two different equations of state does not make much difference. This is interesting since using a more realistic equation of state based on lattice QCD calculations is not expected to give the same result as that obtained using the traditional EOS based on the Bag Model. There is some difference, but it is not significant ($\sim 2\%$ maximum in the case of second order diffusion) compared to the overall width.

The most noticeable feature to observe in Fig. 8.7 is the difference between the

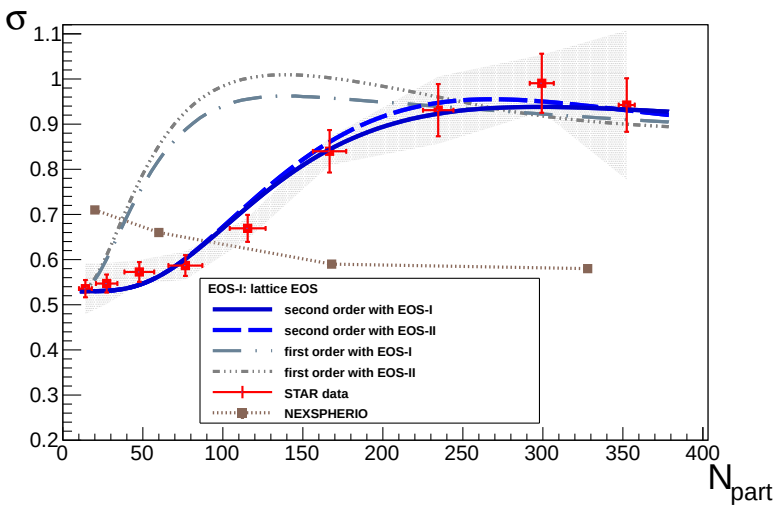

Figure 8.7: Widths from computations using the first order and second order diffusion equation using both EOS's. The data are STAR measurements for Ref. [43]. Also shown are widths computed by NEXSPHERIO using ideal hydrodynamics [100].

first and second order computation results. It is significant, except in the case of the central collisions. The difference gets bigger for collisions less central than about 25% (note that 0% is the most central). This is a little surprising since second order hydrodynamics, in principle, is the next order correction in perturbations to first order hydrodynamics, as we have highlighted in Chapter 4. We notice that both first and second order computational results agree well with the experimental data for $\sim 25\%$ and more central collisions. As collisions get more peripheral, the first order results begin to deviate from the second order results and the experimental data.

The most sensitive parameters that affects the results are the initial time τ_0 and the factor β. In the case of the former parameter the values from 0.6 to 1 are often used. There is no satisfactory reason yet to decide on a particular value yet. In this context we just want to use the mostly used value, $\tau_0 = 1$ fm. We also use this value because it better fits the data. Therefore, in the case of initial time, we are using 'the end justifies the means' methods. Unless there is any compelling reason, we also employ this approach. In the case of the other important parameter we have the

kinetic theory computation as a compelling reason. Quantum kinetic theory puts the values around $\beta \sim 6$. We have chosen $\beta = 6$.

In order to see the effects of other choiceS of these parameters, we show the results obtained using different values of β and the initial time τ_0. We have observed that they are the parameters that affect the final results significantly. Our choice for the factor β is 6, in accordance with kinetic theory, as we pointed out earlier. First let we would like to mention that if we choose $\beta = 6.5 - 7$, the resulting width match even better than with $\beta = 6$. The result is not shown here and we are not interested in taking a bigger value of this factor just to get a better match with experimental data. As we have noted that bigger this factor is the smaller will be the diffusion compared to the wave effect. We do not want to undermine diffusion. We therefore stick with the value consistent with the kinetic theory. However, in order to show the effect of this factor in our results we first present the results obtained using smaller β. Figs. 8.8 and 8.9 show the results with $\beta = 2$ and 4 , respectively.

Fig. **??** shows the results with $\tau_0 = 0.8$ and 1.2 fm. In these results, we used only the lattice EOS, i.e., the EOS I. We see that a smaller value of β gives a less weight to the wave part. Consequently, results of second order computation more and more like the results of the first order theory. We clearly notice this trends if we compare Figs. 8.7, 8.8 and 8.8. The later two use only EOS I.

As for the value of β, we get slightly better fit with $\beta = 7$ (the result is not shown here). However, this will not be consistent with kinetic theory calculation and we use $\beta = 6$.

The computational results from the second order equations agrees very well with the experimental data at all centralities. This leads us to conclude that the first order diffusion equation and, thus, the first order relativistic hydrodynamic theory is not suitable for accurately describing the evolution of, at least, the correlation function. We need to use second order hydrodynamics for a more accurate description.

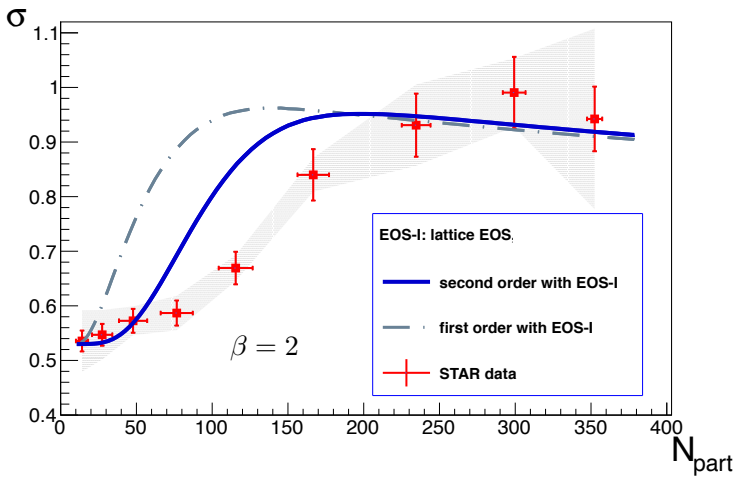

Figure 8.8: Widths from computations using smaller β, $\beta = 2$. The data are STAR measurements for Ref. [43]. Smaller β shifts the second order toward the first order.

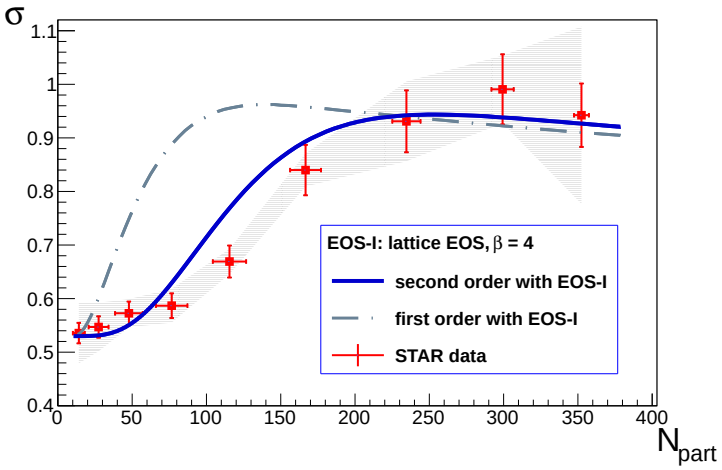

Figure 8.9: Same as Fig.8.8 except that $\beta = 4$ here. The data are STAR measurements for Ref. [43].

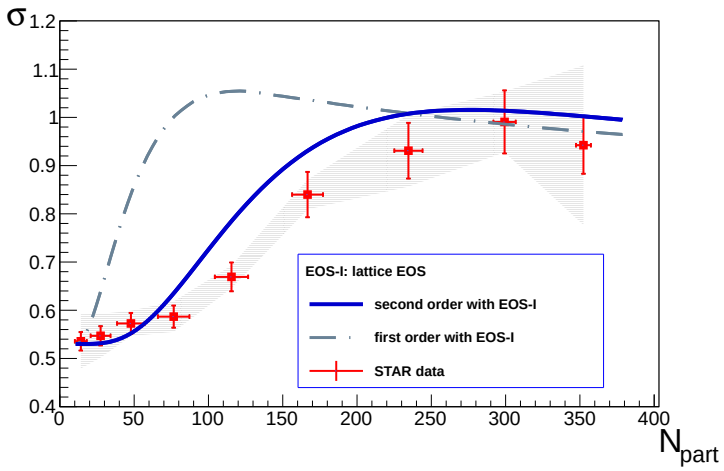

Figure 8.10: This result is obtained using different initial time: $\tau_0 = 0.8$ fm. The data are STAR measurements for Ref. [43].

We may try to understand the difference between the first and second order results by comparing the evolution time with the relaxation time. Going back to Fig. 8.5, we see that the system's evolution time is greater than its relaxation time if the number of participants is greater than ~ 200. For $\sqrt{s} = 200$ GeV Au-Au collisions, this corresponds to a centrality of about 30%. Therefore, in reality the system may not have enough time to evolve before relaxation. This leads us to question our assumptions of thermodynamic equilibrium for mid-central to peripheral collisions. We, however, believe that results from full 3+1 dimensional hydrodynamics are necessary to make any strong claim about deviation from equilibrium. It should be noted that 3+1 dimensional codes for two-particle correlations, are like 6+1 dimensional in terms of computation. Longitudinal Bjorken boost invariance does reduce the dimensionality since, as we have seen, diffusion depends on η. This is a real computational challenge. One should note that a full 3+1dimensional hydrodynamic calculations are comparatively very recent developments in the field [111, 112].

We have found, to a good approximation, that the transverse expansion does not contribute to our integral correlation observables, like $\mathcal{C}$. The longitudinal expansion in our model, therefore carries the significance of a more general three dimensional

expansions, albeit in approximation. We will discuss this important point in Chapter 9.

Again, the we see an excellent agreement of the widths computed using second order theory. This is not so with the results we get from the first order theory. This leads us to conclude that the second order theory is much well equipped to describe the hydrodynamic evolution of of p_t correlations in comparison to the first oder theory.

Fig. 8.7 also shows the results of the NEXSPHERIO computation of the width. We observe that the results do not agree with the data. In fact, we see the widths decreasing rather than increasing with increasing centrality. Here, we need to note, as was pointed out in Chapter 6, that NEXSPHERIO uses ideal hydrodynamics, not viscous hydrodynamics. Also, NEXSPHERIO uses fluctuating initial conditions. We ascribe these features (especially the use of ideal hydrodynamics) for the different results from NEXSPHERIO computations. Comparison with the NEXSPHERIO results leads us to conclude that ideal hydrodynamics does not provide accurate description of the evolution of the correlation function.

One other reason we wanted to refer to NEXSPHERIO computation is to show that the resonance decays does not appear to be contributing to the width. We expect the same in the results of our model.

8.3.2 p_t covariance, $\mathcal{C}$

Another observable we have computed is the amplitude of two-particle p_t covariance, $\mathcal{C}$. As mentioned in Chapter 6, STAR group has also measured this quantity as well [43]. Figure 8.11 shows our results for eight different centralities. We have not included the plot for the 50 - 60% case as the behavior is similar to its neighboring centrality bin. This figure also shows the published STAR data from Ref. [43]. We note an excellent agreement between the computed and experimental data. Here, the computed numbers are from the calculations using the second order, or causal,

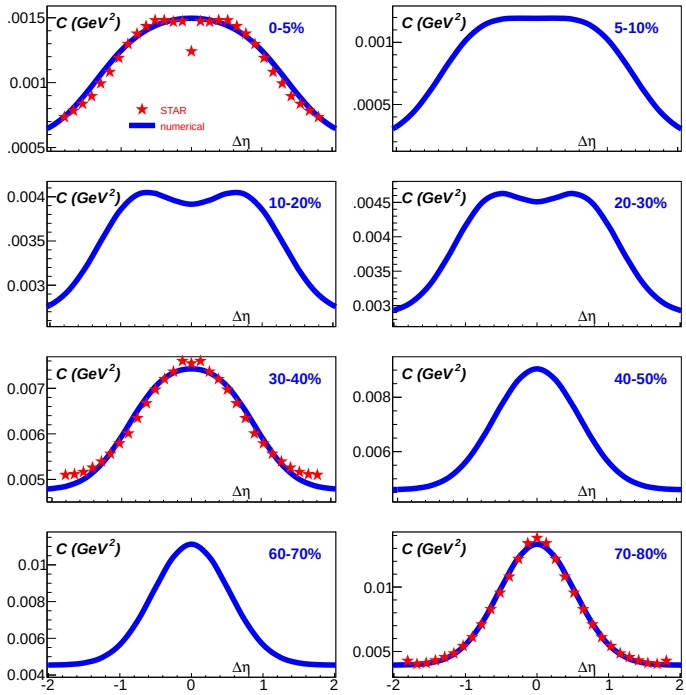

Figure 8.11: p_t correlation amplitude $\mathcal{C}$ for various centrality bins. The experimental data are from [43]. As discussed in Chapter 6, the noticeable errors on experimental data are at the offsets only (not shown here).

diffusion equation. We would like to point out that the errors in the experimental data are mainly on the offsets, as is mentioned in Chapter 6. The errors for the peaks are too small (of the order of 10^{-5}) to be noticeable in the plots and have not been included in preparing Fig. 8.11.

In Fig. 8.11, we notice an interesting feature in the plots of the central and near central collision cases. This feature is the double hump structure in the peak of the correlation. This double hump occurs in the central collision cases and the plots indicate that it modifies the very short range correlations. In the peripheral case there is no double hump at all.

In order to understand the double hump we first want to see if there are any other centralities in the experimental data showing this feature. Fig. 8.12 shows the comparison that includes data from other centralities [113] as well. We notice that the comparison is not as close as in Fig. 8.11, but the double humps appear at the

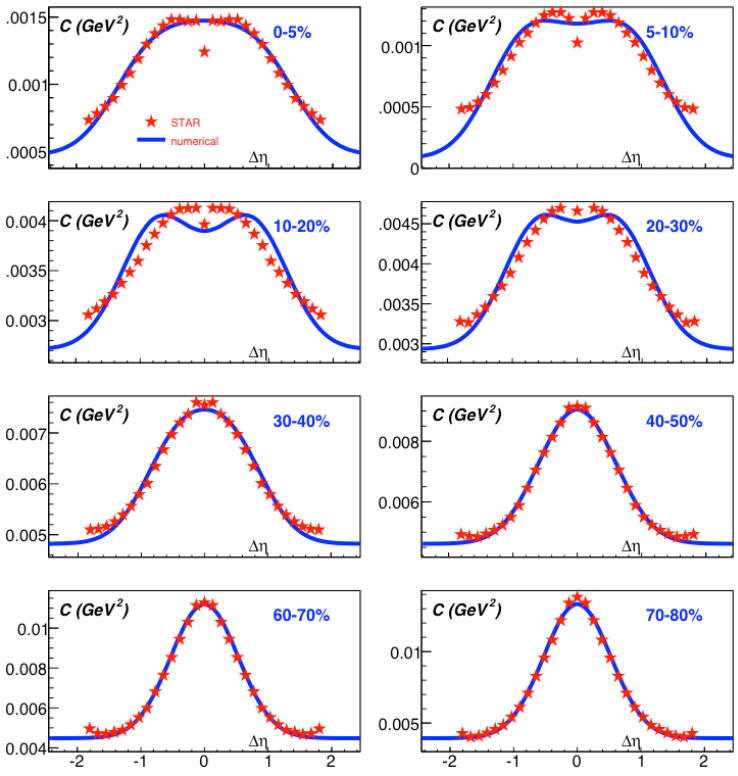

Figure 8.12: p_t correlation amplitude $\mathcal{C}$ for various centrality bins. This figure is the same as Fig. 8.11 except that it includes the experimental data for other centralities [113].

same centrality bins in both experimental data and the numerical computations.

We now compare the correlation $\mathcal{C}$ computed from the first and second order diffusion equations. Figure 8.13 shows this comparison.

We observe that there is no double hump in the results from the first order diffusion calculations. The comparison of the computations from first order and second order diffusion equations indicates that the double hump effect on the short range correlation peaks is the consequence of the competing wave and diffusion part of the equations. This occurs mostly in central collisions. It should be noted that more particles gain transverse momenta in central collisions than in peripheral ones. So even if we consider the soft particles, they collectively have a higher p_t than in the case of peripheral collisions and hence a more relativistic effect. So, we can expect more

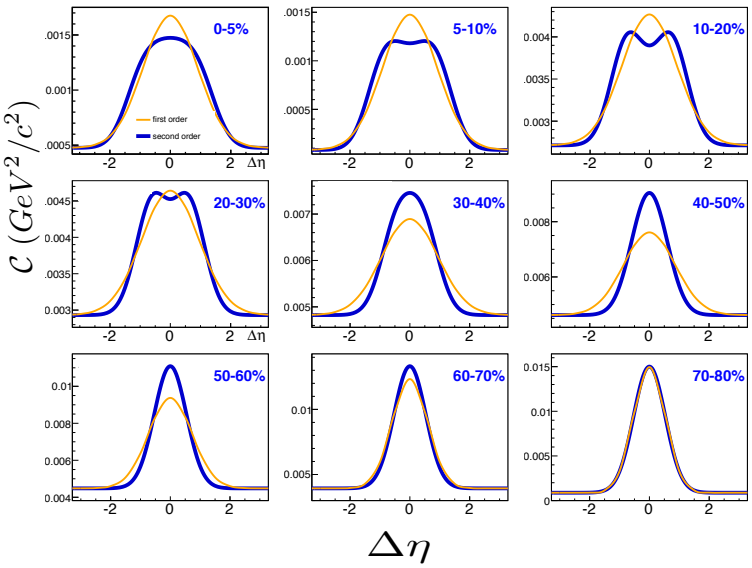

Figure 8.13: Correlation amplitude $\mathcal{C}$ from first order and second order diffusion of Δr. The main difference is in the double hump for mostly the central collisions.

deviations from first order diffusion. However, a stronger second order effect means the inclusion of propagating wave behavior on top of diffusion. As we have already pointed out, that kinetic theory requires a high value of relaxation time compared to the strength of diffusion. This puts a significant weight on the wave behavior. As a result, we see double humps in the central collisions.

Figure 8.14 shows the evolution of the correlation amplitude $\mathcal{C}$ before it gets the shape of the double hump structure from the previous plots at freeze out. This figure shows how the initial gaussian evolves and acquires the double hump when the system nears end of hydrodynamic evolution at the freeze out temperature. This also shows that it is not all wave propagation - the waves takes over relatively late int the short evolution time, which is 4.7 fm for 10-20% centrality. The evolution time decreases very quickly as the collision becomes more peripheral, as can be seen in Fig. 8.5. When the effective diffusion coefficient (ν/τ^2) becomes smaller. At the beginning it is clearly diffusion while the wave effect becomes more dominant later. We should note that this profile is plotted in rapidity space. In rapidity space the wave propagation

appears to saturate, as discussed earlier in this chapter.

In the case of a smaller β, the wave part is not as dominant (but still present to make the distribution deviate more from a Gaussian) and we should get mostly the diffusion effect. This is indeed the case. Fig. 8.15 shows the same evolution but with different value of beta, $\beta = 2$. We need to note that this is unrealistically low value for β from kinetic theory point of view. Kinetic theory suggests a value $\sim$ 5-6, as has been pointed out earlier. Moreover, correlation widths obtained using this low value of beta differ significantly from the experimentally measured values, as demonstrated in Section 8.3.1. The choice of β consistent with the values given by kinetic theory makes both observables, the width and the correlation amplitude, better match with the experimental data. These observations demonstrate that the second order theory with reasonable diffusion and relaxation coefficients is better equipped to explain the experimental data and is, therefore, should be more realistic.

We want to emphasize again that our reasoning for the double humps (or the flattening of the Gaussian) in the results of second order computation of $\mathcal{C}$ is simple. To paraphrase again, it is the interplay between the diffusion and wave propagation behavior contained in the causal diffusion equation. The strong weight factor for wave propagation, due to comparatively large relaxation time, causes the double hump structure in the correlation profile. The double hump is an extreme case, the wave behavior is responsible for the flattening of the otherwise Gaussian like profile. Note that, regular or first order diffusion alone does not change the Gaussian nature of the initial distribution. Fig. 8.13, clearly demonstrates this point. It should be note that the second order solutions here clearly deviates from the Gaussian distribution as compared to the first order solution.

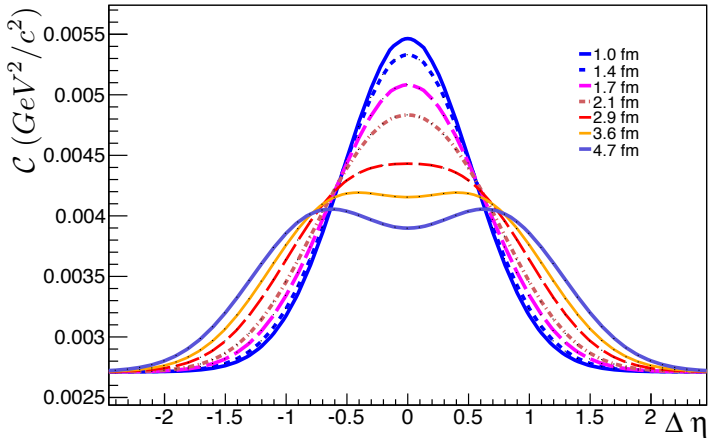

Figure 8.14: Evolution of the correlation amplitude profile for 10 - 20% centrality. It reaches freeze out at the proper time of 4.7 fm.

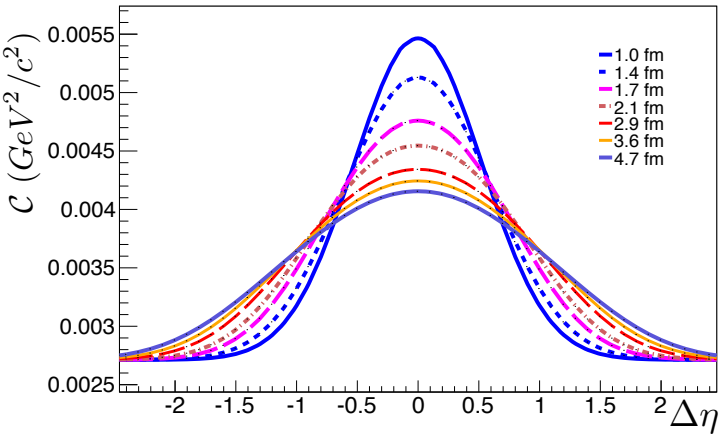

Figure 8.15: Evolution of the correlation amplitude profile for 10 - 20% centrality. Parameters used to obtain this results are the same except for β, which is 2 here instead of 6.

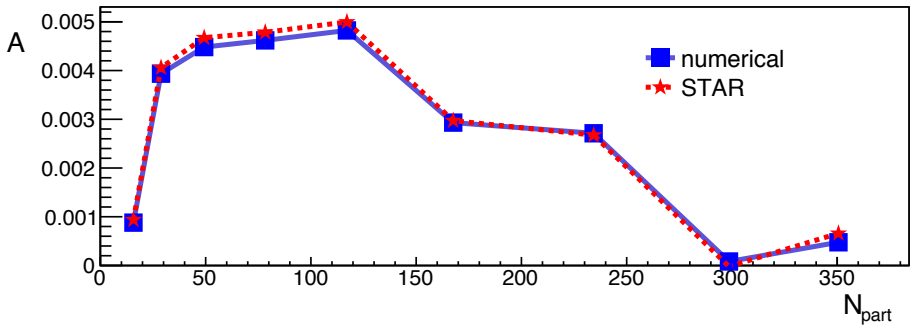

Figure 8.16: Offset or baseline, A. As shown in the labels, the blue squares are offsets from our computations using second order diffusion equation. The red stars are from STAR data of Ref. [43, 113].

8.3.3 The offset

We have discussed the offset in Chapter 6 in some detail. There we also discussed how a constant solution of the diffusion equations serves a the offset and may be a basis of explanation of a part of the ridge. Note that, the offset is the constant A discussed there.

Here we present the constant solution A we need to fit the data and the constant baseline STAR used in their analysis [43, 113]. It is very interesting that the values match very well. This matching indicates that understanding the background thermal noise can help understanding the ridge. Currently the use of flat baseline is not unique. For example, in Ref. [104], a wide gaussian has been used as the base line. Use of different baselines in experimental analysis simply reflects the fact that we have yet to understand what ridge is. Understanding ridge can be subject of our future research.

In Fig. 8.16, we compare the offsets we needed to fit our computations and those from the STAR analysis of Ref. [43]. We need to note here that we do not have the statistical and systematic errors for the offset data. This figure shows a good agreement of computed offsets with the offsets applied in the experimental analysis.

CHAPTER 9

OUTLOOK AND SUMMARY

In this chapter we summarize our work as well as present a brief sketch of our future work. Before going there we, however, start this chapter by demonstrating the redundancy of the transverse expansion. In Chapter 6 we briefly stated that we would later show this redundancy in the context of our observables. Using a simple conservation principle argument we show that how the transverse expansion integrates out. We then discuss the possible extension of this work and the subject of future study. Finally, we finish this dissertation with some concluding remarks.

9.1 Transverse expansion and our observables

We recall that the evolution of the p_t correlation in our model is dictated by first and second order hydrodynamics. We used Bjorken longitudinal boost invariance and ignored the transverse expansion making it possible to solve the equations numerically. As discussed briefly in Chapter 6, a full 3+1 dimensional evolution of two-particle correlations poses a real computational challenge. The consideration of only the longitudinal expansion was done to get around this challenge. However, our analysis and results are more general than they appear in that light. In fact, it can be demonstrated with a simple argument that we barely loose generality using the longitudinal expansion alone, as far as our observables are concerned.

Here we make a simple but general argument based on first principles - the conservation of energy momentum: $\partial_\mu T^{\mu\nu} = 0$. Let us integrate this relation over $\mathbf{r}_\perp$, which is basically same as integrating over the azimuthal angle ϕ. We get

$$\int d\mathbf{r}_\perp \partial_0 T^{0\nu} + \int d\mathbf{r}_\perp \partial_i T^{i\nu} = 0 \tag{9.1}$$

For simplicity, let us pick y as the transverse component, i.e., take $\nu = y$. We get

$$\begin{aligned} 0 &= \int \mathrm{d}x\,\mathrm{d}y\,\partial_0 T^{0y} + \int \mathrm{d}x\,\mathrm{d}y\,\partial_i T^{iy} \\ &= \int \mathrm{d}x\,\mathrm{d}y\,\frac{\partial T^{0y}}{\partial t} + \int \mathrm{d}x\,\mathrm{d}y\,\left(\partial_x T^{xy} + \partial_y T^{yy}\right) + \int \mathrm{d}x\,\mathrm{d}y\,\frac{\partial T^{zy}}{\partial z} \\ &= \frac{\partial}{\partial t}\int \mathrm{d}^2 r_\perp\, T^{0y} + \int \mathrm{d}^2 r_\perp\,\frac{\partial T^{zy}}{\partial z} \end{aligned} \tag{9.2}$$

The integral of the middle term in the second line is a surface integral of a gradient. If we take the surface to "infinity", i.e., to a large $r_\perp$, we see that this term vanishes. Note that this is the very term that contains the transverse expansion. The last one is the longitudinal expansion term. Upon linearization and using $T_{zy} = -\eta\partial_z v^y$ we obtain the diffusion equation, which is the first order version of Eqn. (3.34). Note the generality of this simple argument. It does not depend on whether the energy momentum tensor has the Navier-Stokes or the Israel-Stewart form. This argument is, therefore, valid for the second order diffusion equation for T^{0i} as well. We recall that we generalized an Israel-Stewart form of T^{0i} to obtain our second order diffusion equation for Δr, Eqn. (5.11). It is then evident that our observable $\mathcal{C}$, which is an integral of Δr (Eqn. (6.6)), does not depend on the transverse expansion. Here need to note the assumptions made to get to the conclusion - that the transverse coordinates $\mathbf{r}_\perp$ of the expanding system can be taken large enough to make the surface term in Eqn. 9.2 vanish. Therefore, the results computed using the longitudinal expansion are general results, as long as the assumptions used here are valid. Also note that we have used Bjorken longitudinal boost invariance, which itself is an approximation. Bjorken boost invariance is used in almost all hydrodynamic models because of the simplifications it provides in deriving relations.

It is also important to note the role of current or energy momentum conservation for making the transverse expansion redundant. In our case the current is the current of transverse momentum, which is a conserved quantity. We cannot make the same

argument with quantities like particle number. Particle numbers or multiplicities are not conserved.

A relevant quantity that was integrated out in our treatment is the mean transverse flow of particles, the quantity $\langle u_y \rangle$ in Fig. 3.2. We have taken this mean flow to be zero. This is also reflected in the use of a co-moving frame, or $u^\mu = (1, \mathbf{0}) + \delta u^\mu$, in our linearization of the equations of motion in Chapter 3. Now, we can rely on this assumption, since the transverse expansion integrates out and we use Bjorken boost invariance for the longitudinal expansion. If one wants to include the effect of the mean flow one must solve a full 3+1 dimensional problem. For $v \ll 1$ (i.e., the almost non-relativistic case) with Bjorken boost longitudinal invariance, one gets (see Ref. [114, 115])

$$\frac{\partial \mathbf{g_t}}{\partial \tau} + (\mathbf{v}_\perp \cdot \nabla_\perp)\mathbf{g_t} + (\mathbf{g_t} \cdot \nabla_\perp)\mathbf{v}_\perp = \nu \left(\frac{1}{\tau^2} \frac{\partial^2}{\partial \eta^2} + \nabla_\perp^2 \right) \mathbf{g_t} \tag{9.3}$$

Solving Eqn. 9.3, when generalized for two-particle correlations, is not a trivial numerical task. Also, form a theoretical point of view, it remains to be generalized to fully relativistic case. The latter is also a challenge when looking at the almost intractable terms one gets from the expression of $\pi^{\mu\nu}$ if one does not assume a co-moving frame, or zero mean flow.

9.2 Future Work

We have mentioned in previous chapters that experimental measurements of two-particle correlations of detected particles show complex valleys, hills and ridges in $\Delta\eta$ and $\Delta\phi$. The complex correlation profiles must be the results of various effects - jets, various anisotropic flows, resonances, and so on. What we have done here is an attempt to understand a limited aspect of it, viz., the contribution of shear viscosity to the correlations in $\Delta\eta$. We definitely want to understand and explain a bigger

picture, which means at least some aspects of the whole three dimensional profile of the experimentally measured correlations. Any attempt in that direction requires the solution of full 3+1 dimensional hydro. Currently, there are challenges, as we have mentioned in the previous section. Overcoming these challenges and extending our current work will be our immediate future work.

The challenges mentioned in the previous section are opportunities as well. There are two immediate extensions. Let us call them "project one" and "project two". These two projects basically involve the extension of current work to full 3+1 dimensions. In brief, the first is to develop equation for evolution of two-particle correlation from Eqn. (9.3) and solve it. Project two involves developing a fully relativistic form of Eqn. (9.3) and starting from there. Note that Eqn. (9.3) holds for near the non-relativistic limit, $v \ll 1$. Thus both involve going to full 3+1 dimensions.

The challenge we have now with "project one" is mainly numerical. As was pointed out previously, a full 3+1 dimensional treatment of such an equation, for the two-particle case, turns out to be like dealing with a 6+1 dimensional problem as far as numerical computations are concerned. Even when we exploit the Bjorken invariance to make the beam axis coordinate redundant, the diffusion equation still depends on that coordinate. The quantities like energy density, temperature, etc., depend only on the proper time and not on η, but Δr diffuses in η. In this context, our future work will attempt to look for viable numerical techniques to solve equations in higher dimensions. One needs to note that full 3+1 dimensional hydrodynamics are recent entrants in the field [111, 112]. So far, we have developed a way to handle 4+1 dimensional solutions. Therefore our attempt will be looking for the possibility to extend it further or to look for a way to reduce the dimensionality of the equations involved.

When we achieve the goal of solving full 3+1 dimensional equations for two-particle correlations, project two is then more of about theoretical generalization.

We have noted that Eqn. (9.3) assumes a near non-relativistic limit for fluid particle speed. Linearizing the equations of motion with a general form of $\pi^{\mu\nu}$ (see Eqns. 3.18 and 3.28) and including the mean flow requires rather tedious theoretical calculations. In order to simplify we can first do this without the mean flow. This makes the model similar to current one but extended to full 3+1 spacetime dimensions. Then we attempt to include the mean flow. It should be noted again that in our current work the mean flow is taken as zero. Even if we had not taken it to be zero, it would have been integrated out, as explained in the previous section. The purpose of including the mean flow is to get rid to the requirement of large $r_\perp$ necessary for the surface term to vanish.

The obvious reason to generalize to $3 + 1$ dimensions is that it is more realistic and we want to understand the overall correlation profile including that in $\Delta\phi$, not just in $\Delta\eta$. We want to understand how much dissipative effects like shear viscosity contribute to the overall correlation profile. The reason for studying the effect of the mean flow is similar.

One interesting aspect of hydrodynamics and correlation study is related to the longitudinal modes. So far our study is focused only on transverse modes, which are the shear modes. Our focus on the shear modes was initially motivated by the shear viscosity of quark-gluon plasma. The longitudinal modes are the sound modes. Interest in fluctuating hydrodynamics of longitudinal modes has begun to grow recently (see Ref. [116], for example).

In order to elaborate on the shear and longitudinal modes in the simplest way, we may take the non-relativistic linearized Navier-Stoke equation, with (somewhat) relativistic momentum current $\mathbf{g}_i = T_{0i} - \langle T_{0i} \rangle \approx (\varepsilon + p)\mathbf{v}_i \approx sT\mathbf{v}_i$

$$\partial_t g_i + \nabla_i p = \frac{\eta/3 + \zeta}{sT} \nabla_i \left(\nabla \cdot \mathbf{g}\right) + \frac{\eta}{sT} \nabla^2 \mathbf{g}_i \tag{9.4}$$

Now we use the Helmholtz decomposition into longitudinal and transverse components $\mathbf{g} = \mathbf{g}_L + \mathbf{g}_T$, where $\nabla \times \mathbf{g}_L = 0$, and $\nabla \cdot \mathbf{g}_T = 0$. Then we find that these components decouple into the equations for transverse and longitudinal modes. The transverse mode, obviously, satisfies the diffusion equation

$$\partial_t \mathbf{g}_T = \frac{\eta}{Ts} \nabla^2 \mathbf{g}_T \tag{9.5}$$

The longitudinal modes, on the other hand, are compression waves damped by viscosity:

$$\partial_t \mathbf{g}_L + \nabla p = \frac{4\eta/3 + \zeta}{sT} \nabla \left(\nabla \cdot \mathbf{g}_L \right) \tag{9.6}$$

We note that our study of this work is solely on the the diffusion of the transverse shear modes. It will definitely be interesting to include the longitudinal modes in our study.

9.3 Conclusion

This dissertation details our work on the study of the two-particle transverse momentum correlation function of particles produced in ultra-relativistic heavy ion collisions. We used second order Israel-Stewart hydrodynamics and stochastic techniques to develop equations for the evolution of the p_t correlations. We found that such correlation above the thermal background fluctuations follows a deterministic second order diffusion equation. The first order case had previously been studied by Gavin and Abdel-Aziz [71], which also provided an alternative method for estimating the shear viscosity to entropy ratio, η/s, for quark-gluon plasma. In addition to the second order diffusion equation we developed, we also used the first order equation to compute experimentally measurable observables discussed in Chapter 6.

We used a general temperature dependent η/s in order to compute the diffusion and relaxation coefficients at each temperature. These coefficients determines the

strengths of competing wave and diffusion behavior of the second order diffusion equation. This is discussed in detail in Chapter 8. Dependency of shear viscosity on temperature is based on the relations put together in the work of Hirano and Gyulassy in Ref. [85]. Information on entropy density is obtained from lattice QCD calculations and also from standard Bag Model based calculation. We have also used the latest information on the relaxation coefficient. This is all discussed in Chapter 4. The main point is that we have used the latest information on necessary transport coefficients and equations of state.

In our numerical computations we especially focused on $\sqrt{s} = 200$ GeV Au+Au collisions at RHIC. This allowed us to compare the computed observables with the same observables measured by STAR for these Au+Au collisions [43]. We have mentioned the experimental results in Chapter 6 and compared the results with our computations in Chapter 8 with discussion.

Our model only uses the longitudinal expansion since, as explained in Section 9.1, the transverse expansion turns out to be redundant as far as our observables are concerned. The underlying assumptions behind this result is also explained in that section.

We observed in Chapter 8 that the second order diffusion model better reproduces the experimental data. The computational results from the first order equation deviates from the experimental results except for the case of central collisions. As explained in Chapter 8, we attributed the better agreement to the effects of the interplay between the relaxation time and diffusion strength, both of which contains the information on the shear viscosity to entropy density ratio. No viscosity information means, we use equations of ideal hydrodynamics. We used the computations by NEXSHPERIO to compare our results with ideal hydrodynamic computations. As stated in Chapters 6 and 8, NEXSPHERIO uses ideal hydrodynamics with fluctuating initial conditions. The correlation widths resulting from those computations,

however, showed wide discrepancy from our viscous hydrodynamics computations and the experimental results.

Computations using a second order diffusion equation also gives a feature that is not present in the results of the first order case. We have ascribed the feature to the wave part of the second order diffusion equation, which becomes significant in light of the fact that the relaxation coefficient has a larger value as compared to the diffusion coefficient, according to the latest theoretical calculations. This is explained in Chapters 4 and 8. This feature is also present in experimental results [43], at the same centralities. We also ascribed a part of the ridge to a constant solution to our diffusion equation. This is demonstrated by the fact that there is a good agreement with the offset taken in the experimental analysis and the values of our constant solutions for all centralities.

In order to understand the full correlation profiles in $\Delta\eta$ and $\Delta\phi$, we need to generalize our model to include transverse expansion as well. In our current work, we integrated out transverse expansion. We also want to see the effect of non-zero mean flow. Overall, we need to see the contributions from all possible effects on the correlation results. This can be done by going to full 3+1 dimensional hydrodynamics for two-particle correlations. Our future work will be to address this challenging task.

The importance of correlation and related fluctuation studies and measurements in heavy ions collisions and related physics can hardly be exaggerated. This work is an attempt to make a small contribution to the bigger goal in an attempt to understand the correlation features RHIC and LHC experiments have given to us. The need to properly understand the correlation features has increased even more since now we see the ridge features even in p+p and p+Pb collisions at LHC energies.

REFERENCES

[1] D. Gross and F. Wilczek, "Ultraviolet Behavior of Nonabelian Gauge Theories," *Phys.Rev.Lett.* **30** (1973) 1343–1346.

[2] H. D. Politzer, "Reliable Perturbative Results for Strong Interactions?," *Phys.Rev.Lett.* **30** (1973) 1346–1349.

[3] J. C. Collins and M. Perry, "Superdense Matter: Neutrons Or Asymptotically Free Quarks?," *Phys.Rev.Lett.* **34** (1975) 1353.

[4] F. Karsch, "Lattice results on QCD thermodynamics," *Nucl.Phys.* **A698** (2002) 199–208, arXiv:hep-ph/0103314 [hep-ph].

[5] N. Cabibbo and G. Parisi, "Exponential Hadronic Spectrum and Quark Liberation," *Phys.Lett.* **B59** (1975) 67–69.

[6] S. Bethke, "Experimental tests of asymptotic freedom," *Prog.Part.Nucl.Phys.* **58** (2007) 351–386, arXiv:hep-ex/0606035 [hep-ex].

[7] http://qgp.phy.duke.edu/.

[8] A. Adare *et al.*, (PHENIX Collaboration collaboration), "Enhanced production of direct photons in Au+Au collisions at $\sqrt{s_{NN}} = 200$ GeV and implications for the initial temperature," *Phys.Rev.Lett.* **104** (2010) 132301, arXiv:0804.4168 [nucl-ex].

[9] M. Luzum and P. Romatschke, "Viscous Hydrodynamic Predictions for Nuclear Collisions at the LHC," *Phys.Rev.Lett.* **103** (2009) 262302, arXiv:0901.4588 [nucl-th].

[10] F. Karsch, E. Laermann, and A. Peikert, "The Pressure in two flavor, (2+1)-flavor and three flavor QCD," *Phys.Lett.* **B478** (2000) 447–455, arXiv:hep-lat/0002003 [hep-lat].

[11] P. Huovinen and P. Petreczky, "QCD Equation of State and Hadron Resonance Gas," *Nucl.Phys.* **A837** (2010) 26–53, arXiv:0912.2541 [hep-ph].

[12] A. Bazavov, T. Bhattacharya, M. Cheng, N. Christ, C. DeTar, *et al.*, "Equation of state and QCD transition at finite temperature," *Phys.Rev.* **D80** (2009) 014504, arXiv:0903.4379 [hep-lat].

[13] J. Adams *et al.*, (STAR Collaboration collaboration), "Experimental and theoretical challenges in the search for the quark gluon plasma: The STAR Collaboration's critical assessment of the evidence from RHIC collisions," *Nucl.Phys.* **A757** (2005) 102–183, arXiv:nucl-ex/0501009 [nucl-ex].

[14] K. Adcox *et al.*, (PHENIX Collaboration collaboration), "Formation of dense partonic matter in relativistic nucleus-nucleus collisions at RHIC: Experimental evaluation by the PHENIX collaboration," *Nucl.Phys.* **A757** (2005) 184–283, arXiv:nucl-ex/0410003 [nucl-ex].

[15] B. Back, M. Baker, M. Ballintijn, D. Barton, B. Becker, *et al.*, "The PHOBOS perspective on discoveries at RHIC," *Nucl.Phys.* **A757** (2005) 28–101, arXiv:nucl-ex/0410022 [nucl-ex].

[16] I. Arsene *et al.*, (BRAHMS Collaboration collaboration), "Quark gluon plasma and color glass condensate at RHIC? The Perspective from the BRAHMS experiment," *Nucl.Phys.* **A757** (2005) 1–27, arXiv:nucl-ex/0410020 [nucl-ex].

[17] http://www.bnl.gov/bnlweb/pubaf/pr/pr_display.asp?prid=05-38.

[18] Y. Aoki, G. Endrodi, Z. Fodor, S. Katz, and K. Szabo, "The Order of the quantum chromodynamics transition predicted by the standard model of particle physics," *Nature* **443** (2006) 675–678, arXiv:hep-lat/0611014 [hep-lat].

[19] H. Satz, "Parton percolation in nuclear collisions," arXiv:hep-ph/0212046 [hep-ph].

[20] http://www.bnl.gov/rhic/.

[21] http://lhc.web.cern.ch/lhc/LHC_Experiments.htm.

[22] P. Braun-Munzinger, K. Redlich, and J. Stachel, "Particle production in heavy ion collisions," arXiv:nucl-th/0304013 [nucl-th].

[23] V. Koch and A. Majumder, "Equilibrium in heavy ion collisions," *Heavy Ion Phys.* **21** (2004) 273–278, arXiv:nucl-th/0305085 [nucl-th].

[24] S. Voloshin and Y. Zhang, "Flow study in relativistic nuclear collisions by Fourier expansion of Azimuthal particle distributions," *Z.Phys.* **C70** (1996) 665–672, arXiv:hep-ph/9407282 [hep-ph].

[25] M. Luzum and P. Romatschke, "Conformal Relativistic Viscous Hydrodynamics: Applications to RHIC results at s(NN)**(1/2) = 200-GeV," *Phys.Rev.* **C78** (2008) 034915, arXiv:0804.4015 [nucl-th].

[26] B. Alver *et al.*, (PHOBOS Collaboration collaboration), "The Eccentricities of flow: Elliptic flow fluctuations and evidence for transverse localization in the initial state of the matter in relativistic heavy ion collisions," arXiv:nucl-ex/0702029 [nucl-ex].

[27] B. Abelev *et al.*, (STAR Collaboration collaboration), "Centrality dependence of charged hadron and strange hadron elliptic flow from

s(NN)**(1/2) = 200-GeV Au + Au collisions," *Phys.Rev.* **C77** (2008) 054901, arXiv:0801.3466 [nucl-ex].

[28] A. Adare *et al.*, (PHENIX Collaboration collaboration), "Scaling properties of azimuthal anisotropy in Au+Au and Cu+Cu collisions at s(NN) = 200-GeV," *Phys.Rev.Lett.* **98** (2007) 162301, arXiv:nucl-ex/0608033 [nucl-ex].

[29] J. Adams *et al.*, (STAR Collaboration collaboration), "Evidence from d + Au measurements for final state suppression of high p(T) hadrons in Au+Au collisions at RHIC," *Phys.Rev.Lett.* **91** (2003) 072304, arXiv:nucl-ex/0306024 [nucl-ex].

[30] S. Adler *et al.*, (PHENIX Collaboration collaboration), "Centrality dependence of direct photon production in s(NN)**(1/ 2) = 200-GeV Au + Au collisions," *Phys.Rev.Lett.* **94** (2005) 232301, arXiv:nucl-ex/0503003 [nucl-ex].

[31] J. Bjorken, "Energy Loss of Energetic Partons in Quark - Gluon Plasma: Possible Extinction of High p(t) Jets in Hadron - Hadron Collisions,".

[32] X.-N. Wang and M. Gyulassy, "Gluon shadowing and jet quenching in $A + A$ collisions at $\sqrt{s}$ =200 A gev," *Phys. Rev. Lett.* **68** (Mar, 1992) 1480–1483. http://link.aps.org/doi/10.1103/PhysRevLett.68.1480.

[33] J. Adams *et al.*, (STAR Collaboration collaboration), "Transverse momentum and collision energy dependence of high p(T) hadron suppression in Au+Au collisions at ultrarelativistic energies," *Phys. Rev. Lett.* **91** (2003) 172302, arXiv:nucl-ex/0305015 [nucl-ex].

[34] S. Adler *et al.*, (PHENIX Collaboration collaboration), "High p_T charged

hadron suppression in Au + Au collisions at $\sqrt{s}_{NN} = 200$ GeV," *Phys.Rev.* **C69** (2004) 034910, arXiv:nucl-ex/0308006 [nucl-ex].

[35] S. Adler *et al.*, (PHENIX Collaboration collaboration), "High transverse momentum η meson production in p^+p, d^+ Au and Au+Au collisions at $S(NN)^{(1/2)} = 200$-GeV," *Phys.Rev.* **C75** (2007) 024909, arXiv:nucl-ex/0611006 [nucl-ex].

[36] K. Aamodt *et al.*, (ALICE Collaboration collaboration), "Suppression of Charged Particle Production at Large Transverse Momentum in Central Pb–Pb Collisions at $\sqrt{s_{NN}} = 2.76$ TeV," *Phys. Lett.* **B696** (2011) 30–39, arXiv:1012.1004 [nucl-ex].

[37] S. Pal and M. Bleicher, "Suppression of high transverse momenta hadrons in Pb+Pb collisions at LHC," *Phys.Lett.* **B709** (2012) 82–86, arXiv:1201.2546 [nucl-th].

[38] J. Putschke, "Intra-jet correlations of high-p(t) hadrons from STAR," *J.Phys.* **G34** (2007) S679–684, arXiv:nucl-ex/0701074 [NUCL-EX].

[39] J. Putschke. Private communications.

[40] S. Gavin, L. McLerran, and G. Moschelli, "Long Range Correlations and the Soft Ridge in Relativistic Nuclear Collisions," *Phys.Rev.* **C79** (2009) 051902, arXiv:0806.4718 [nucl-th].

[41] C.-Y. Wong, "The Ridge structure associated with the near-side jet in the Delta phi - Delta eta correlation," *Phys.Rev.* **C76** (2007) 054908, arXiv:0707.2385 [hep-ph].

[42] E. Shuryak, "On the origin of the 'Ridge' phenomenon induced by jets in

heavy ion collisions," *Phys.Rev.* **C76** (2007) 047901, arXiv:0706.3531 [nucl-th].

[43] H. Agakishiev *et al.*, (STAR Collaboration collaboration), "Evolution of the differential transverse momentum correlation function with centrality in Au+Au collisions at $\sqrt{s_{NN}} = 200$ GeV," *Phys.Lett.* **B704** (2011) 467–473, arXiv:1106.4334 [nucl-ex].

[44] B. Alver *et al.*, (PHOBOS Collaboration collaboration), "High p(T) Triggered Delta eta, Delta-phi Correlations over a Broad Range in Delta eta," *J.Phys.* **G35** (2008) 104080, arXiv:0804.3038 [nucl-ex].

[45] E. Fermi, "High-energy nuclear events," *Prog.Theor.Phys.* **5** (1950) 570–583.

[46] L. Landau, "On the multiparticle production in high-energy collisions," *Izv.Akad.Nauk Ser.Fiz.* **17** (1953) 51–64.

[47] R. Hagedorn, "Statistical thermodynamics of strong interactions at high-energies," *Nuovo Cim.Suppl.* **3** (1965) 147–186.

[48] B. M. J. Kapusta and J. Rafelski, *Quark-Gluon Plasma: Theoretical Foundations, An annotated reprint collection.* Elsevier, Oxford, 2003.

[49] J. D. Bjorken, "Highly Relativistic Nucleus-Nucleus Collisions: The Central Rapidity Region," *Phys. Rev.* **D27** (1983) 140–151.

[50] S. Adler *et al.*, (PHENIX Collaboration collaboration), "Elliptic flow of identified hadrons in Au+Au collisions at s(NN)**(1/2) = 200-GeV," *Phys.Rev.Lett.* **91** (2003) 182301, arXiv:nucl-ex/0305013 [nucl-ex].

[51] J. Adams *et al.*, (STAR Collaboration collaboration), "Azimuthal anisotropy in Au+Au collisions at s(NN)**(1/2) = 200-GeV," *Phys.Rev.* **C72** (2005) 014904, arXiv:nucl-ex/0409033 [nucl-ex].

[52] P. Huovinen, P. Kolb, U. W. Heinz, P. Ruuskanen, and S. Voloshin, "Radial and elliptic flow at RHIC: Further predictions," *Phys.Lett.* **B503** (2001) 58–64, arXiv:hep-ph/0101136 [hep-ph].

[53] D. Teaney, J. Lauret, and E. Shuryak, "A Hydrodynamic description of heavy ion collisions at the SPS and RHIC," arXiv:nucl-th/0110037 [nucl-th].

[54] L. D. Landau and E. M. Lifshitz, *Fluid Mechanics*. Pergamon, Oxford, 1963.

[55] S. R. de Groot, W. A. van Leewen, and C. G. van Weert, *Relativistic Kinetic Theory*. North Holland, Amsterdam, 1980.

[56] A. Muronga, "Causal theories of dissipative relativistic fluid dynamics for nuclear collisions," *Phys.Rev.* **C69** (2004) 034903, arXiv:nucl-th/0309055 [nucl-th].

[57] P. Huovinen and P. Ruuskanen, "Hydrodynamic Models for Heavy Ion Collisions," *Ann.Rev.Nucl.Part.Sci.* **56** (2006) 163–206, arXiv:nucl-th/0605008 [nucl-th].

[58] J.-Y. Ollitrault, "Relativistic hydrodynamics," *Eur. J. Phys.* **29** (2008) 275–302, arXiv:0708.2433 [nucl-th].

[59] P. Romatschke, "New Developments in Relativistic Viscous Hydrodynamics," *Int. J. Mod. Phys.* **E19** (2010) 1–53, arXiv:0902.3663 [hep-ph].

[60] T. Hirano, N. van der Kolk, and A. Bilandzic, "Hydrodynamics and Flow," *Lect.Notes Phys.* **785** (2010) 139–178, arXiv:0808.2684 [nucl-th].

[61] U. W. Heinz, "Early collective expansion: Relativistic hydrodynamics and the transport properties of QCD matter," arXiv:0901.4355 [nucl-th].

[62] C. Eckart, "The thermodynamics of irreversible processes. iii. relativistic theory of the simple fluid," *Phys. Rev.* **58** (Nov, 1940) 919–924. http://link.aps.org/doi/10.1103/PhysRev.58.919.

[63] H. Song and U. W. Heinz, "Interplay of shear and bulk viscosity in generating flow in heavy-ion collisions," *Phys.Rev.* **C81** (2010) 024905, arXiv:0909.1549 [nucl-th].

[64] A. Muronga, "Second order dissipative fluid dynamics for ultrarelativistic nuclear collisions," *Phys.Rev.Lett.* **88** (2002) 062302, arXiv:nucl-th/0104064 [nucl-th].

[65] M. A. Aziz and S. Gavin, "Causal diffusion and the survival of charge fluctuations in nuclear collisions," *Phys. Rev.* **C70** (2004) 034905, arXiv:nucl-th/0404058.

[66] W. A. Hiscock and L. Lindblom, "Generic instabilities in first-order dissipative relativistic fluid theories," *Phys.Rev.* **D31** (1985) 725–733.

[67] C. Cattaneo, "Sulla conduzione del calore.," *Atti Semin. Mat. Fis. Univ., Modena* **3** (1949) 83–101.

[68] W. Israel, "Nonstationary irreversible thermodynamics: A Causal relativistic theory," *Ann. Phys.* **100** (1976) 310–331.

[69] U. W. Heinz, H. Song, and A. K. Chaudhuri, "Dissipative hydrodynamics for viscous relativistic fluids," *Phys.Rev.* **C73** (2006) 034904, arXiv:nucl-th/0510014 [nucl-th].

[70] R. Baier, P. Romatschke, and U. A. Wiedemann, "Dissipative hydrodynamics and heavy ion collisions," *Phys.Rev.* **C73** (2006) 064903, arXiv:hep-ph/0602249 [hep-ph].

[71] S. Gavin and M. Abdel-Aziz, "Measuring Shear Viscosity Using Transverse Momentum Correlations in Relativistic Nuclear Collisions," *Phys.Rev.Lett.* **97** (2006) 162302, arXiv:nucl-th/0606061 [nucl-th].

[72] C. Kittel and H. Kroemer, *Thermal Physics*. W. H. Freeman, 1980.

[73] K. Aamodt *et al.*, (The ALICE Collaboration collaboration), "Elliptic flow of charged particles in Pb-Pb collisions at 2.76 TeV," *Phys.Rev.Lett.* **105** (2010) 252302, arXiv:1011.3914 [nucl-ex].

[74] A. Hosoya and K. Kajantie, "Transport coefficients of qcd matter," *Nuclear Physics B* **250** (1985) no. 14, 666 – 688.

[75] P. Danielewicz and M. Gyulassy, "Dissipative Phenomena in Quark Gluon Plasmas," *Phys. Rev.* **D31** (1985) 53–62.

[76] S. Gavin, "TRANSPORT COEFFICIENTS IN ULTRARELATIVISTIC HEAVY ION COLLISIONS," *Nucl. Phys.* **A435** (1985) 826–843.

[77] M. H. Thoma, "Viscosity coefficient of the quark - gluon plasma in the weak coupling limit," *Phys. Lett.* **B269** (1991) 144–148.

[78] P. B. Arnold, G. D. Moore, and L. G. Yaffe, "Transport coefficients in high temperature gauge theories: (I) Leading-log results," *JHEP* **11** (2000) 001, arXiv:hep-ph/0010177.

[79] P. B. Arnold, G. D. Moore, and L. G. Yaffe, "Transport coefficients in high temperature gauge theories. II: Beyond leading log," *JHEP* **05** (2003) 051, arXiv:hep-ph/0302165.

[80] A. Muronga, "Shear Viscosity Coefficient from Microscopic Models," *Phys. Rev.* **C69** (2004) 044901, arXiv:nucl-th/0309056.

[81] L. P. Csernai, J. I. Kapusta, and L. D. McLerran, "On the strongly-interacting low-viscosity matter created in relativistic nuclear collisions," *Phys. Rev. Lett.* **97** (2006) 152303, arXiv:nucl-th/0604032.

[82] T. Schafer and D. Teaney, "Nearly Perfect Fluidity: From Cold Atomic Gases to Hot Quark Gluon Plasmas," *Rept.Prog.Phys.* **72** (2009) 126001, arXiv:0904.3107 [hep-ph]. 69 pages, 9 figures, review article.

[83] D. A. Teaney, "Viscous Hydrodynamics and the Quark Gluon Plasma," arXiv:0905.2433 [nucl-th].

[84] M. Prakash, M. Prakash, R. Venugopalan, and G. Welke, "Non-equilibrium properties of hadronic mixtures," *Physics Reports* **227** (1993) no. 6, 321 – 366.

[85] T. Hirano and M. Gyulassy, "Perfect Fluidity of the Quark Gluon Plasma Core as Seen through its Dissipative Hadronic Corona," *Nucl. Phys.* **A769** (2006) 71–94, arXiv:nucl-th/0506049.

[86] https://wiki.bnl.gov/hhic/index.php/Lattice_calculatons_of_Equation_of_State.

[87] A. Muronga, "Erratum: Second order dissipative fluid dynamics for ultrarelativistic nuclear collisions [phys. rev. lett. 88, 062302 (2002)]," *Phys. Rev. Lett.* **89** (Sep, 2002) 159901.

[88] B. Abelev *et al.*, (ALICE Collaboration collaboration), "Charged-particle multiplicity density at mid-rapidity in central Pb-Pb collisions at $\sqrt{s_{NN}} = 2.76$ TeV," *Phys.Rev.Lett.* **105** (2010) 252301, arXiv:1011.3916 [nucl-ex].

[89] S. Chatrchyan *et al.*, (CMS Collaboration collaboration), "Observation of long-range near-side angular correlations in proton-lead collisions at the LHC," *Physics Letters B* (2012) , arXiv:1210.5482 [nucl-ex].

[90] T. J. Tarnowsky, "Long-Range Multiplicity Correlations in Relativistic Heavy Ion Collisions as a Signal for Dense Partonic Matter," arXiv:0807.1941 [nucl-ex].

[91] T. Lappi and L. McLerran, "Long range rapidity correlations as seen in the STAR experiment," *Nucl.Phys.* **A832** (2010) 330–345, arXiv:0909.0428 [hep-ph].

[92] C. W. Gardiner, *Handbook of stochastic methods for physics, chemistry, and the natural sciences*, vol. 42. Springer, 1985.

[93] N. G. V. Kampen, *Stochastic Processes in Physics and Chemistry*. Elsevier, Amsterdam, 2 ed., 1997.

[94] M. A. York and G. D. Moore, "Second order hydrodynamic coefficients from kinetic theory," *Phys. Rev.* **D79** (2009) 054011, arXiv:0811.0729 [hep-ph].

[95] J. Hong, D. Teaney, and P. M. Chesler, "The Wake of a Heavy Quark in Non-Abelian Plasmas : Comparing Kinetic Theory and the AdS/CFT Correspondence," arXiv:1110.5292 [nucl-th].

[96] B. Schenke, S. Jeon, and C. Gale, "Higher flow harmonics from (3+1)D event-by-event viscous hydrodynamics," *Phys.Rev.* **C85** (2012) 024901, arXiv:1109.6289 [hep-ph].

[97] H. Song and U. W. Heinz, "Causal viscous hydrodynamics in 2+1 dimensions for relativistic heavy-ion collisions," *Phys.Rev.* **C77** (2008) 064901, arXiv:0712.3715 [nucl-th].

[98] J. Adams *et al.*, (STAR Collaboration collaboration), "Incident energy dependence of pt correlations at RHIC," *Phys.Rev.* **C72** (2005) 044902, arXiv:nucl-ex/0504031 [nucl-ex].

[99] S. Gavin, "Traces of thermalization from p(t) fluctuations in nuclear collisions," *Phys. Rev. Lett.* **92** (2004) 162301, arXiv:nucl-th/0308067.

[100] M. Sharma, C. Pruneau, S. Gavin, J. Takahashi, R. D. de Souza, *et al.*, "Longitudinal dependence of two-particle momentum correlations from NEXSPHERIO model," *Phys.Rev.* **C84** (2011) 054915, arXiv:1107.3587 [nucl-th].

[101] R. A. Lacey, A. Taranenko, R. Wei, N. Ajitanand, J. Alexander, *et al.*, "Azimuthal anisotropy: transition from hydrodynamic flow to jet suppression," *Phys.Rev.* **C82** (2010) 034910, arXiv:1005.4979 [nucl-ex].

[102] C. Shen, U. Heinz, P. Huovinen, and H. Song, "Radial and elliptic flow in Pb+Pb collisions at the Large Hadron Collider from viscous hydrodynamic," *Phys.Rev.* **C84** (2011) 044903, arXiv:1105.3226 [nucl-th].

[103] B. Abelev *et al.*, (STAR Collaboration collaboration), "Long range rapidity correlations and jet production in high energy nuclear collisions," *Phys.Rev.* **C80** (2009) 064912, arXiv:0909.0191 [nucl-ex].

[104] L. De Silva, (STAR Collaboration collaboration), "Evolution of structures in two particle correlations in RHIC Cu+Cu collisions as a function of centrality and momentum," arXiv:0910.5938 [nucl-ex].

[105] Y. Hama, R. Peterson G. Andrade, F. Grassi, W.-L. Qian, T. Osada, *et al.*, "NeXSPheRIO Results on Elliptic-Flow Fluctuations at RHIC," *Phys.Atom.Nucl.* **71** (2008) 1558–1564, arXiv:0711.4544 [hep-ph].

[106] H. J. Drescher, F. M. Liu, S. Ostapchenko, T. Pierog, and K. Werner, "Initial condition for quark-gluon plasma evolution," *Phys. Rev. C* **65** (Apr, 2002) 054902. http://link.aps.org/doi/10.1103/PhysRevC.65.054902.

[107] J. Takahashi, B. Tavares, W. Qian, R. Andrade, F. Grassi, *et al.*, "Topology studies of hydrodynamics using two particle correlation analysis," *Phys.Rev.Lett.* **103** (2009) 242301, arXiv:0902.4870 [nucl-th].

[108] W.-L. Qian, R. Andrade, J. Socolowski, Otavio, F. Grassi, T. Kodama, *et al.*, "p(T) distribution of hyperons in 200-A-GeV Au-Au in smoothed particle hydrodynamics," *Braz.J.Phys.* **37** (2007) 767–769, arXiv:nucl-th/0612061 [nucl-th].

[109] B. Abelev *et al.*, (STAR Collaboration collaboration), "Systematic Measurements of Identified Particle Spectra in pp, d^+ Au and Au+Au Collisions from STAR," *Phys.Rev.* **C79** (2009) 034909, arXiv:0808.2041 [nucl-ex]. 60 pages, 46 figures, 37 tables.

[110] E. Zauderer, *Partial differential equations of applied mathematics*. Pure and applied mathematics. Wiley-Interscience, 2006.

[111] B. Schenke, S. Jeon, and C. Gale, "Elliptic and triangular flow in event-by-event (3+1)D viscous hydrodynamics," *Phys.Rev.Lett.* **106** (2011) 042301, arXiv:1009.3244 [hep-ph].

[112] P. Bozek, "Flow and interferometry in 3+1 dimensional viscous hydrodynamics," *Phys.Rev.* **C85** (2012) 034901, arXiv:1110.6742 [nucl-th].

[113] M. Sharma and C. Pruneau. Private communications.

[114] S. Gavin and M. Abdel-Aziz, "Measuring shear viscosity using correlations," *Brazilian Journal of Physics* **37** (09, 2007) 1023 – 1030. http://www.scielo.br/scielo.php?script=sci_arttext&pid=S0103-97332007000600020&nrm=iso.

[115] S. Gavin and G. Moschelli, "Viscosity and the Soft Ridge at RHIC," *J.Phys.* **G35** (2008) 104084, arXiv:0806.4366 [nucl-th].

[116] J. Kapusta, B. Muller, and M. Stephanov, "Relativistic Theory of Hydrodynamic Fluctuations with Applications to Heavy Ion Collisions," *Phys.Rev.* **C85** (2012) 054906, arXiv:1112.6405 [nucl-th].

ABSTRACT

SECOND ORDER AND FLUCTUATING HYDRODYNAMIC THEORY OF TWO-PARTICLE TRANSVERSE MOMENTUM CORRELATIONS IN NUCLEAR COLLISIONS

by

RAJENDRA K POKHAREL

AUGUST 2013

Advisor: Dr. Sean Gavin

Major: Physics

Degree: Doctor of Philosophy

Relativistic heavy ion collision experiments show clear evidence of creation of a very short-lived phase of nuclear matter consisting of color-deconfined quarks and gluons. This matter is known as the quark-gluon plasma (QGP). Fluctuation and correlation measurements of the detected particles have played a very important role in revealing the properties of QGP. In particular, these measurements have shown that the QGP behaves like a nearly perfect liquid. Relativistic hydrodynamics has been successfully used to study how the QGP evolves before the system hadronizes and ultimately produces the final state particles. Transport properties like shear viscosity constitute an important part in such studies.

This work is focused on developing a second order hydrodynamic theory for the evolution of two-particle transverse momentum correlations. We use general temperature dependent transport and relaxation coefficients as well as the latest information on equations of state and use both first and second order relativistic viscous hydrodynamics to compute experimentally measurable observables. We will show that our computations using the second order viscous hydrodynamics are in good agreement with experimental data. We also highlight some features that distinguish the second order viscous hydrodynamic evolution of QGP from the first order.

AUTOBIOGRAPHICAL STATEMENT

4 May, 1968	Born in Udaypur NEPAL
1989 – 1991	B.Sc. Physics Tribhuvan University Kathmandu, NEPAL
1993 – 1995	M.Sc. Physics Tribhuvan University Kathmandu, NEPAL
1996 – 1998	Science and Mathematics Teacher Little Angels School Hattiban, Lalitpur, Nepal
1998 – 2002	Assistant Lecturer, Part Time Trichandra College Tribhuvan University Ghanta Ghar, Kathmandu, Nepal
1999 – 2002	Physics Instructor Xavier Academy Hattiban, Lalitpur, Nepal
2002 – 2004	Graduate Teaching Assistant Department of Physics and Astronomy Bowling Green State University Bowling Green, OH, USA
2005 – 2012	Graduate Teaching and Research Assistant Department of Physics and Astronomy Wayne State University Detroit, MI, USA